

AD A 032432

FG.

DNA 3986F

ELECTRON BEAM IEMP SIMULATION DEVELOPMENT

12

Simulation Physics, Inc.
41 B Street
Burlington, Massachusetts 01803

August 1975

Final Report

CONTRACT No. DNA 001-75-C-0136

APPROVED FOR PUBLIC RELEASE;
DISTRIBUTION UNLIMITED.

THIS WORK SPONSORED BY THE DEFENSE NUCLEAR AGENCY
UNDER RDT&E RMSS CODE B323075464 R99QAXEB08954 H2590D.

Prepared for
Director
DEFENSE NUCLEAR AGENCY
Washington, D. C. 20305

T D D C
RECEIVED
NOV 23 1976
B

Destroy this report when it is no longer
needed. Do not return to sender.



UNCLASSIFIED

SECURITY CLASSIFICATION OF THIS PAGE (When Data Entered)

19 REPORT DOCUMENTATION PAGE		READ INSTRUCTIONS BEFORE COMPLETING FORM
1. REPORT NUMBER DNA 3986F	2. GOVT ACCESSION NO.	3. RECIPIENT'S CATALOG NUMBER
4. TITLE (and Subtitle) ELECTRON BEAM IEMP SIMULATION DEVELOPMENT.	5. TYPE OF REPORT & PERIOD COVERED Final Report.	
7. AUTHOR(s) John R./Uglum, Roger G./Little Steven H./Face	8. CONTRACT OR GRANT NUMBER(s) DNA 01-75-C-0136 NEW	
9. PERFORMING ORGANIZATION NAME AND ADDRESS Simulation Physics, Inc., 41 B Street Burlington, Massachusetts 01803	10. PROGRAM ELEMENT, PROJECT, TASK AREA & WORK UNIT NUMBERS NWED Subtask R99QAXEB089-54	
11. CONTROLLING OFFICE NAME AND ADDRESS Director Defense Nuclear Agency Washington, D.C. 20305	12. REPORT DATE August 1975	13. NUMBER OF PAGES 118
14. MONITORING AGENCY NAME & ADDRESS (if different from Controlling Office)	15. SECURITY CLASS (of this report) UNCLASSIFIED	
15a. DECLASSIFICATION DOWNGRADING SCHEDULE		
16. DISTRIBUTION STATEMENT (of this Report) Approved for public release; distribution unlimited.		
17. DISTRIBUTION STATEMENT (of the abstract entered in Block 20, if different from Report)		
18. SUPPLEMENTARY NOTES This work sponsored by Defense Nuclear Agency under RDT&E RMSS Code B323075464 R99QAXEB08954 H2590D.		
19. KEY WORDS (Continue on reverse side if necessary and identify by block number) Simulation Electron Beams Pulsed Power Internal Electromagnetic Pulse		
20. ABSTRACT (Continue on reverse side if necessary and identify by block number) This report describes work performed to develop improved simulation sources for IEMP studies. Modifications were made to a pulsed electron beam generator to improve current risetime and synchronize machine output with other events. Electron beam diagnostics were developed and calibrated for characterization of environments for IEMP cavity studies. One such study is reported on which involves the phenomenon of enhanced cavity transport when dielectric surfaces are present.		

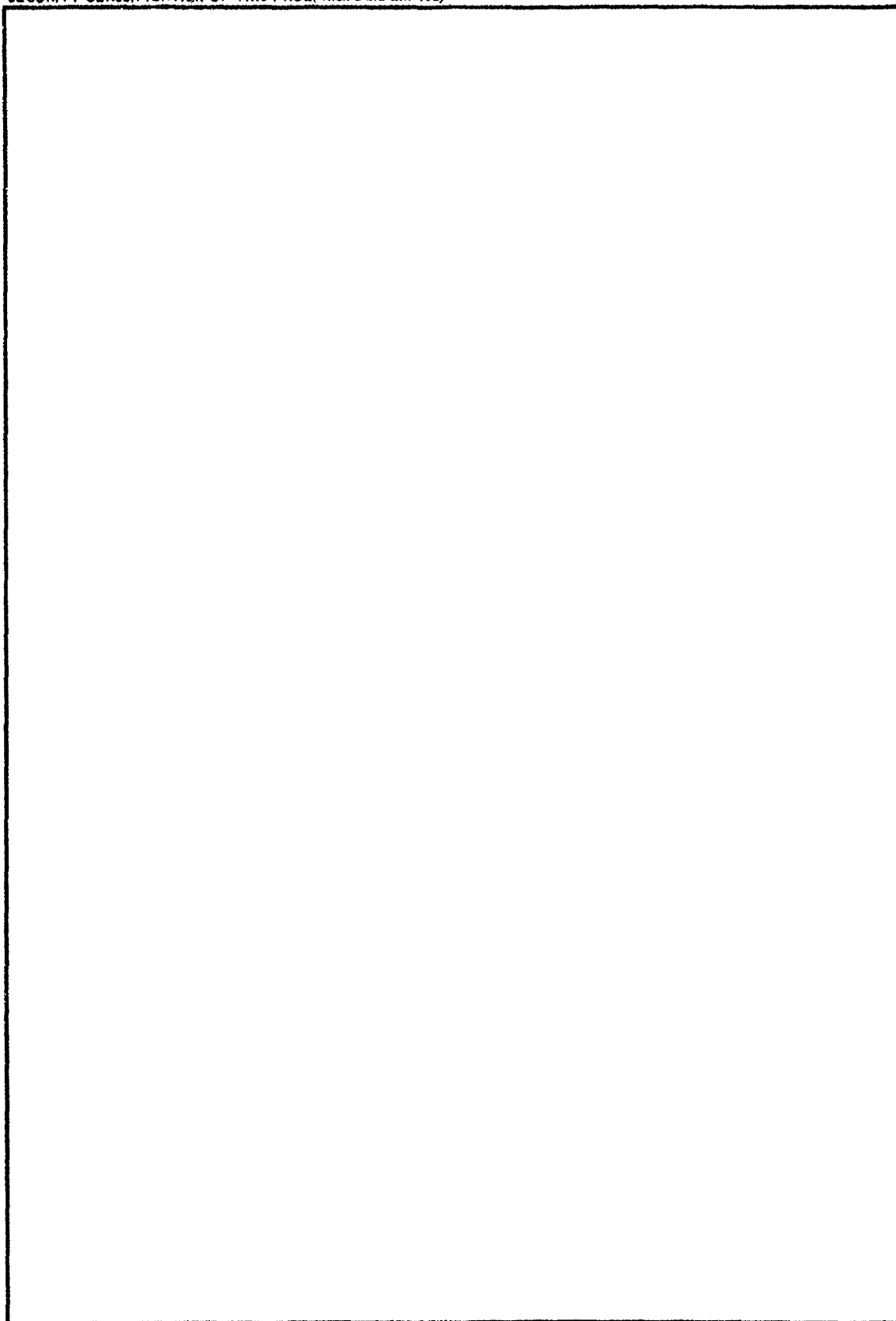
UNCLASSIFIED

SECURITY CLASSIFICATION OF THIS PAGE (When Data Entered)

391 875

UNCLASSIFIED

SECURITY CLASSIFICATION OF THIS PAGE(When Data Entered)



UNCLASSIFIED

SECURITY CLASSIFICATION OF THIS PAGE(When Data Entered)

TABLE OF CONTENTS

<u>SECTION</u>		<u>PAGE</u>
I	INTRODUCTION	9
II	DIAGNOSTICS CALIBRATION	10
	2.1 INTRODUCTION	10
	2.2 VOLTAGE MONITOR CALIBRATION	12
	2.2.1 Step Function Voltage Measurement	12
	2.2.2 RC Decay Time Measurement	13
	2.2.3 Capacitive Bridge Measurement	14
	2.2.4 Matched Transmission Line Measurements	14
	2.2.5 Matched Resistive Load Measurements	18
	2.2.6 Time Resolved Spectrometer Measurements	19
	2.2.7 Summary of Voltage Monitor Calibrations	21
	2.3 CURRENT MONITOR CALIBRATION	23
	2.3.1 Resistive Bridge Measurement	23
	2.3.2 Matched Transmission Line Measurement	23
	2.3.3 Summary of Current Monitor Calibration	24
	2.4 INDUCTIVE VOLTAGE CORRECTION	27
	2.5 SUMMARY OF CALIBRATION RESULTS	29
III	CAVITY TRANSPORT - BENCHMARK EXPERIMENTS	30
	3.1 INTRODUCTION	30
	3.2 EXPERIMENTAL CONFIGURATION AND TEST MATRIX	30
	3.3 INJECTED BEAM PARAMETERS	32
	3.3.1 Diode Measurements	32
	3.3.2 Injected Current	32
	3.3.3 Angular and Energy Spread	36
	3.3.4 Magnetic Spectrometer Measurements	36
	3.3.4.1 Spectrometer Design	40
	3.3.4.2 Spectrometer Probe Energy Resolution	40
	3.3.4.3 Spectrometer Calibration	43
	3.3.4.4 Thirty-Five ns Pulse Results	43
	3.3.5 Injected Beam Parameters - Benchmark Experiments	47
	3.3.6 Injected Current Density	51
	3.4 BENCHMARK EXPERIMENT RESULTS	54

ACCESSION for	
NTIS	White Section <input checked="" type="checkbox"/>
DOC	Buff Section <input type="checkbox"/>
FRANKOUNCED	<input type="checkbox"/>
NOTIFICATION	
BY	
DISTRIBUTION/AVAILABILITY CODES	
Dist.	AVAIL. and/or SPECIAL
A	

TABLE OF CONTENTS (Cont.)

<u>SECTION</u>		<u>PAGE</u>
IV	DIELECTRIC ENHANCED CAVITY TRANSPORT	57
	4.1 INTRODUCTION	57
	4.2 EXPERIMENTAL CONFIGURATION	57
	4.3 CONSTANT CURRENT EXPERIMENTS	59
	4.4 CONSTANT CURRENT DENSITY EXPERIMENTS	66
	4.5 PULSE WIDTH VARIATION EXPERIMENTS	66
	4.6 ION DETECTION EXPERIMENTS	70
	4.7 INTERPRETATION	71
	4.8 CONCLUSIONS	74
V	SPI-PULSE 6000 MODIFICATION	75
	5.1 INTRODUCTION	75
	5.2 RISETIME CONSIDERATIONS	75
	5.2.1 Machine Design and Modifications	75
	5.2.2 Risetime Analysis	77
	5.2.3 Effect of Non-Linear Diode	78
	5.3 TRIGATRON SWITCHING	82
	5.3.1 Trigatron Approach	82
	5.3.2 Trigatron Design Analysis	84
	5.3.3 Trigatron Design	88
	5.3.4 Trigger Voltage Source	90
	5.3.5 Trigatron Switching Checkout	90
	5.4 MODIFIED SPI-PULSE 6000 TESTING	94
	5.4.1 Machine Final Switching Configuration	94
	5.4.2 SPI-PULSE 6000 Delay and Jitter Measurements	94
	5.4.3 SPI-PULSE 6000 Risetime Measurements	98
VI	SUMMARY	105
	REFERENCES	108

LIST OF FIGURES

<u>FIGURE NO.</u>		<u>PAGE</u>
2.1	Schematic of SPI-PULSE 5000 Diode Diagnostics	11
2.2	Voltage and Current Diagnostics Calibration Using Matched 50 Ohm Transmission Line Section and 1 kV Rep. Rate Pulser	15
2.3	Input and Output Pulses for 50 Ohm Transmission Line Geometry Using 1 kV Rep. Rate Pulser	16
2.4	Voltage Monitor Response with 50 Ohm Transmission Line Geometry Using 1 kV Rep. Rate Pulser	17
2.5	SPI-PULSE 5000 Diode Voltage and Current Waveforms With 41 Ohm Resistive Dummy Load at $V_0 = 150$ kV	20
2.6	Comparison of Time Resolved Spectrometer Output and Measured Diode Voltage (Corrected for Inductive Component) for $\tau = 100$ ns (fwhm)	22
2.7	Current Monitor Calibration for 50 Ohm Transmission Line Geometry Using 1 kV Rep. Rate Pulser	25
2.8	Comparison of Code Calculated Diode Voltage to Measured Diode Voltage Corrected for Inductive Component	28
3.1	Schematic of Typical Configuration for IEMP Benchmark Experiments	31
3.2	IEMP Benchmark Diode Current, Voltage and Inductance Corrected Diode Voltage Waveforms for $\tau = 35$ ns (fwhm)	34
3.3	Dependence of Vacuum Transmitted Current on Cavity Depth	35
3.4	Energy Loss Curves in 0.25 mil Mylar by 25%, 50% and 75% of the Electrons (Eltran Calculation)	37

LIST OF FIGURES (Cont.)

<u>FIGURE NO.</u>		<u>PAGE</u>
3.5	Polar Scattering Distributions In 0.25 mil Mylar for 25%, 50% and 75% of the Electrons (Eltran Calculation)	38
3.6	SPI 180° Magnetic Spectrometer with 10 Time Resolved Channels	41
3.7	Internal Conversion Beta Source Calibration Compared to Calculated Calibration Curve for Magnetic Spectrometer	44
3.8	Diode Diagnostic Waveforms for 35 ns (fwhm) Pulse	45
3.9	Comparison of Computer Injected Electron Energy and Spectrometer Probe Output	46
3.10	Measured Time Integrated Spectrum at 30°	47
3.11	Representative Injected Beam Characteristics for IEMP Benchmark Experiments	49
3.12	Segmented Faraday Cup (12" Diameter) Integrated Current Data for 35 ns (fwhm) Pulse	52
3.13	Segmented Faraday Cup Charge and Current Density Measurements for 35 ns (fwhm) Pulse	53
3.14	Peak Transmitted Current vs. Cavity Pressure for Cavity Depths of 2 cm, 7 cm and 15 cm with 35 ns (fwhm) Pulse in IEMP Benchmark Configuration	55
3.15	Dependence of Transmitted Current Time Signature on Cavity Pressure for 15 cm Deep Cavity and 35 ns (fwhm) Pulse in IEMP Benchmark Configuration	56
4.1	Apparatus for Dielectric Lined Cavity Wall Experiments	58
4.2	Diode Voltage, Injected Current and Comparative Transmitted Current Traces with and without Dielectric Wall at Low Pressure	60
4.3	Peak Vacuum Transmitted Current Dependence Upon Cavity Aspect Ratio	61
4.4	Dependence of Time Delay To Onset of Current Enhancement on Cavity Depth - Constant Injected Current	63

LIST OF FIGURES (Cont.)

<u>FIGURE NO.</u>		<u>PAGE</u>
4.5	Peak Transmitted Current Dependence on Dielectric Thickness	64
4.6	Wall Current Measurements for 15 cm Diameter 10 cm Deep Cavity	65
4.7	Dependence of Transmitted Current on Dielectric Material	67
4.8	Representative Results for Constant Current Density Experiments	68
4.9	Effect of Injected Current Pulse Width Variation Upon Transmitted Current Pulse	69
4.10	Open Shutter Photograph of Surface Flashover on Dielectric Tube	72
5.1	SPI-PULSE 6000 Redesigned Low Inductance Front-end Showing Inner and Outer Conducting Paths	76
5.2	Calculated SPI-PULSE 6000 Risetime vs. Number of Trigger Channels	79
5.3	Calculated SPI-PULSE 6000 Current Risetime Waveforms for Linear and Non-Linear Loads	83
5.4	Electrical Circuit for Trigatron Trigger	85
5.5	Trigatron Assembly	89
5.6	Isolation Resistor-Gap	91
5.7	Front-end Assembly for SPI-PULSE 2500 When Used as a Power Supply Trigger Source	92
5.8	Test Chamber for Trigatrons Under Pressure	93
5.9	Trigatron Trigger Adaptation to SPI-PULSE 6000 Low Inductance Front-end	95
5.10	Relative Switching Delay as a Function of Percentage of Self Breakdown Voltage	96
5.11	Diode Voltage Traces Showing Relative Jitter of SPI-PULSE 6000 Discharge at $V_0 = 165$ kV (Shot No. 2091-2100)	97
5.12	SPI-PULSE 6000 Diode Current Waveform Into a 3.5 ohm Dummy Load Showing 2 ns Improvement From One to Three Trigatrons	99

LIST OF FIGURES (Cont.)

<u>FIGURE NO.</u>		<u>PAGE</u>
5.13	SPI-PULSE 6000 Diode Current Waveform with 30 cm Diameter Cathode and Three Trigatron Switching	101
5.14	Comparison of Measured and Calculated SPI-PULSE 6000 Dummy Load Current Waveforms	103
5.15	Comparison of Measured and Calculated SPI-PULSE 6000 Diode Load Current Waveforms	104
6.1	SPI-PULSE 6000 in SGEMP Configuration	107

LIST OF TABLES

<u>TABLE NO.</u>		<u>PAGE</u>
2.1	Voltage Monitor Calibration Values	21
2.2	Current Monitor Calibration Values	24
3.1	IEMP Benchmark Experiment Data Status August 1975	33
3.2	Time Resolved Spectrometer Measurements Summary	39
3.3	Injected Beam Parameters - Benchmark Experiment	50
5.1	Summary of Jitter Measurement	98

SECTION I INTRODUCTION

The research described in this report was motivated by a need to develop improved simulation sources for IEMP studies. Specifically, the risetime of the injected current pulse in previous work was excessive (50 ns) and improvements in this area were required. Also, to have the capability of irradiating very large cavities it is necessary to be able to synchronously switch several parallel machines. Therefore, the main thrust of the program as originally structured was to modify the SPI-PULSE 6000 machine with a low jitter, multi-channel switch to both improve the machine risetime and demonstrate the capability for synchronous switching. In parallel, another experimental program was designed to study parametrically the phenomenon of enhanced cavity current transport when dielectric surfaces are present.

During the course of this contract it became apparent that certain experiments in support of other IEMP programs were required. Specifically, a thorough calibration of the SPI-PULSE 5000 diode diagnostics was carried out. Once completed, this information was used to define injected beam parameters for a series of benchmark experiments in which pressure and cavity geometry effects on the transport of electron beams were studied. The following sections detail these various efforts.

SECTION II
DIAGNOSTICS CALIBRATION

2.1 INTRODUCTION

To provide meaningful experimental data for comparison with IEMP code results, it is necessary that the beam parameters be known as accurately as possible. In particular, a knowledge of the true voltage and current of the beam-forming diode is necessary for calculating the injected beam energy in cavity experiments.

In this section a review is given of the techniques used to calibrate the voltage and current monitors of the SPI-PULSE 5000 when configured for 12" diameter beam experiments. A schematic of the monitors is shown in Figure 2.1. They consist of a capacitive divider voltage monitor and a low resistance current shunt. The operating principle of the current monitor will be discussed in a later section. For the capacitive divider, the relation between the actual voltage $V_s(t)$ on the cathode shank at the position opposite the voltage monitor and the voltage monitor output $V_M(t)$ is given by the equation

$$\frac{dV_s}{dt} = G_V \left[\frac{dV_M}{dt} + \frac{1}{\tau} V_M \right] \quad (2.1)$$

where

$$\tau = (R + Z) (C_1 + C_2)$$

$$G_V = \frac{(R + Z) (C_1 + C_2)}{ZC_1} = \frac{\tau}{ZC_1}$$

C_1 = capacitance linking the shank to the voltage monitor band.

C_2 = capacitance linking the voltage monitor band to ground.

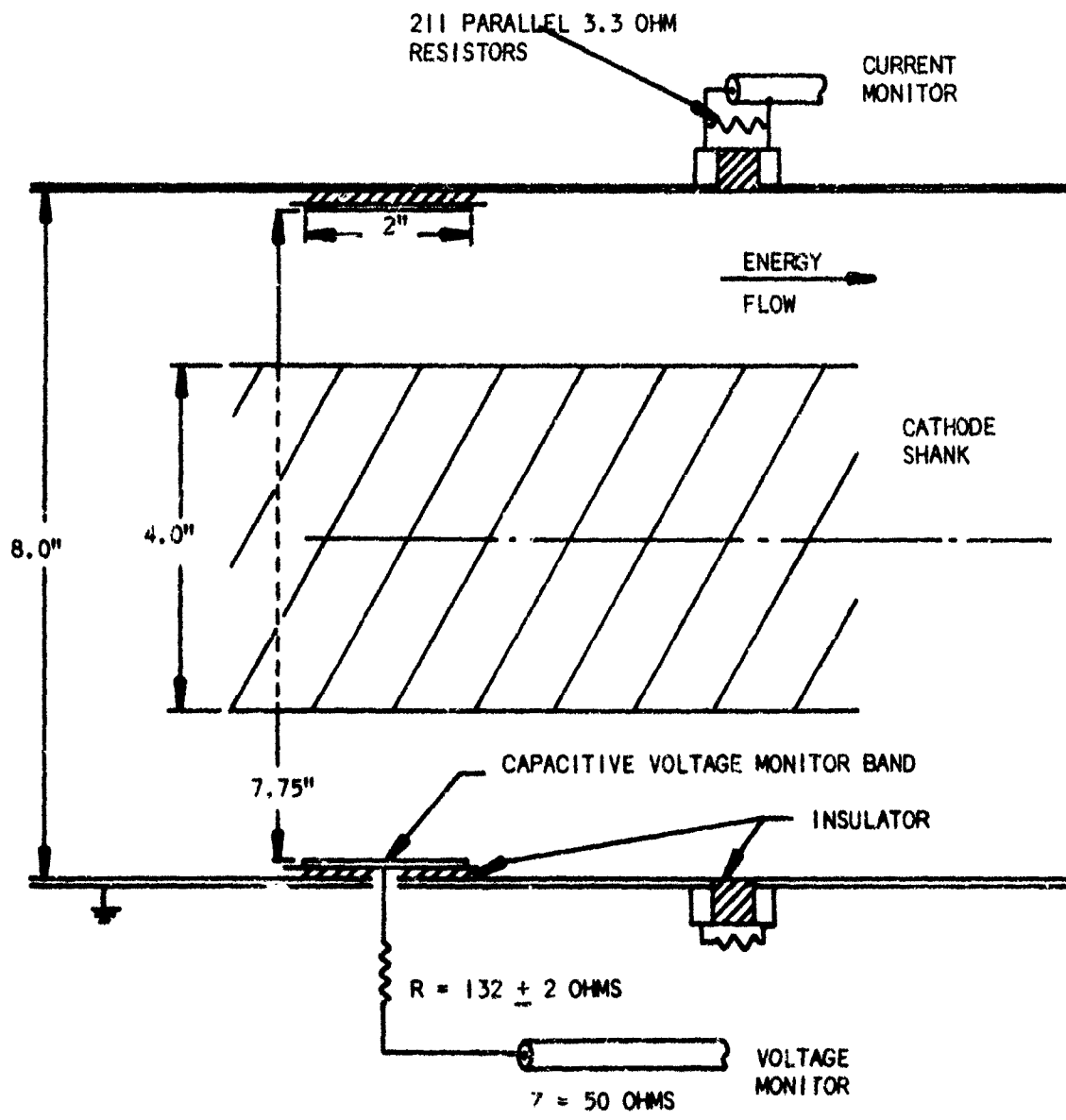


Figure 2.1 Schematic of SPI-PULSE 5000 Diode Diagnostics

The solution of equation (2.1) is

$$V_s(t) = G_V \left\{ V_M(t) + \frac{1}{\tau} \int_0^t V_M(t') dt' \right\} \quad (2.2)$$

One normally designs τ to be very much greater than any pulse length of interest, so that to a good approximation the integral term can be neglected. Then the determination of the voltage monitor coefficient - G_V - is all that is required to calibrate the capacitive divider.

2.2 VOLTAGE MONITOR CALIBRATION

Six experimental methods were used to determine G_V . They consisted of both low voltage and high voltage techniques:

Low Voltage

- Step Function Voltage
- RC Decay Time
- Capacitive Bridge
- Matched Transmission Line

High Voltage

- Matched Resistive Load
- Time Resolved Magnetic Spectrometer

Each method will be considered separately.

2.2.1 Step Function Voltage Measurement

In this technique the step function voltage output of a SPI-PULSE 25 transmission line pulser is split with an unmatched "T". One output is applied to the cathode shank, which quickly charges up to a voltage V_s . The other "T" output is sent to an oscilloscope. This oscilloscope trace then gives the static charging voltage - V_s - on the shank.

Another oscilloscope is used to monitor the capacitive divider output - V_M . From equation (2.2) it follows that for a step function voltage

$$\frac{V_M}{V_S} = G_V^{-1} e^{-t/\tau} \quad (2.3)$$

Thus, by measuring the two oscilloscope outputs at times very much less than τ the coefficient G_V is determined. Experimentally, this ratio is

$$G_V = 9.0 \text{ KV/V}$$

2.2.2 RC Decay Time Measurement

From equation (2.3) it is clear that the decay of the capacitance divider output, when driven by a step function, determines the time constant τ . This was measured to be

$$\tau = 2.1 \pm .1 \text{ } \mu\text{sec}$$

Then since Z is known,

$$G_V = \frac{\tau}{ZC_1} = \frac{42}{C_1 \text{ (pF)}} \frac{\text{KV}}{\text{V}} \quad (2.4)$$

The capacitance C_1 can be estimated from the coaxial line relation

$$C_1 = \frac{2\pi\epsilon_0 l}{\ln r_o/r_i} \quad (2.5)$$

which, from the dimensions given in Figure 2.1, gives

$$C_1 = 4.31 \text{ pF}$$

and

$$G_V = 9.7 \frac{\text{KV}}{\text{V}}$$

2.2.3 Capacitive Bridge Measurement

Since the desired voltage monitor coefficient is given by

$$G_V = \frac{(R + Z)}{Z} \frac{(C_1 + C_2)}{C_1} \approx \frac{(R + Z)}{Z} \frac{C_2}{C_1} \quad (2.6)$$

then since R and Z are known, and C_1 has been estimated, a determination of C_2 is all that is required. This was measured using a calibrated GR capacitance bridge. The result was

$$C_2 = 12,000 \text{ pF}$$

From this, $G_V = 10.1 \text{ KV/V}$.

This bridge measurement was made at 1 khz frequency, whereas typical SPI-PULSE 5000 pulse lengths correspond to greater than 1 Mhz frequency. The frequency dependence of the dielectric material used to insulate the voltage monitor band is such that C_2 would be lower at the higher frequency. Therefore, the value of G_V computed above is probably high.

2.2.4 Matched Transmission Line Measurements

The cathode shank diameter of Figure 2.1 is reduced to 3.5" to make the wave impedance of the coaxial line feeding the load equal to 50 ohms. Thus any wave launched onto it from a 50 ohm source will propagate without reflections if it is terminated in a matched load. Figure 2.2 shows schematically the apparatus used. Pulses from the SPI-PULSE 25 (1000 volts, 1 ns rise, square wave generator) are fed via 50 ohm cable into a 50 ohm biconic transmission line which matches into the 3.5" diameter shank. Another biconic line takes the pulse which has passed the voltage (and current) monitor into another 50 ohm cable which goes to a 7904 oscilloscope. Figure 2.3 shows the measured input pulse to the calibration system and the pulse which has passed through the system. Their equality indicates that the entire structure is very nearly 50 ohms throughout.

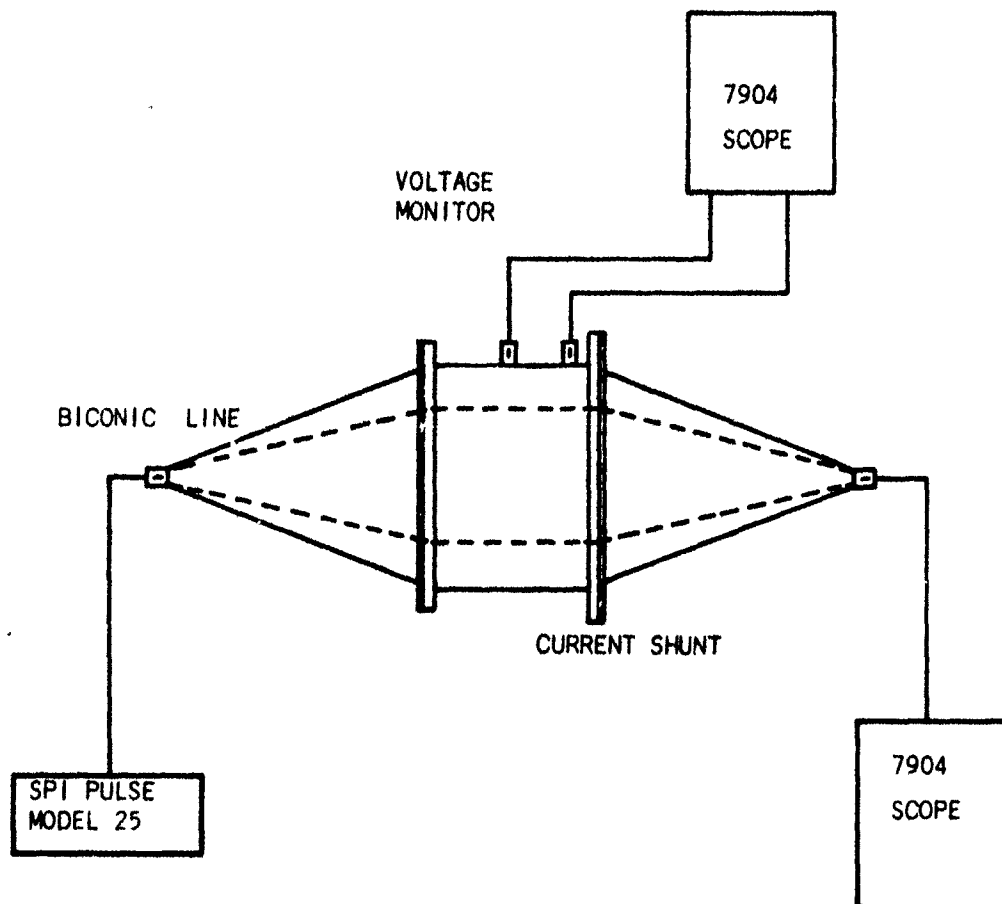
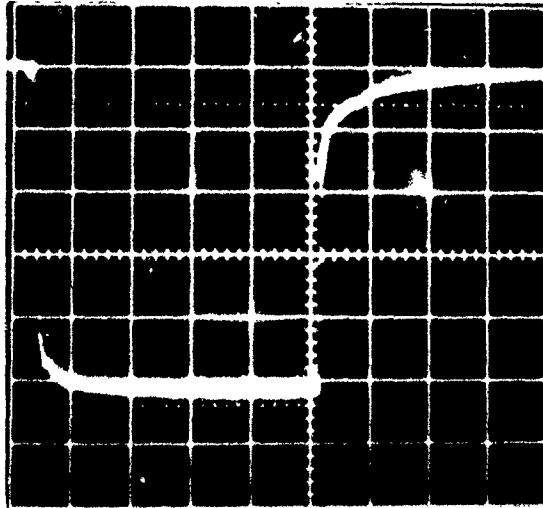
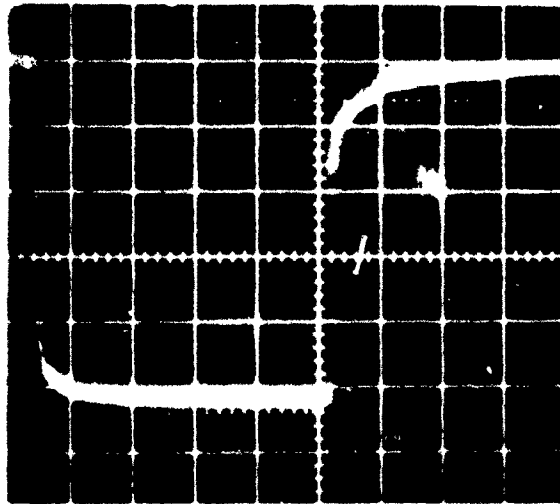


Figure 2.2 Voltage and Current Diagnostics Calibration Using Matched 50 Ohm Transmission Line Section and 1 kV Rep. Rate Pulser

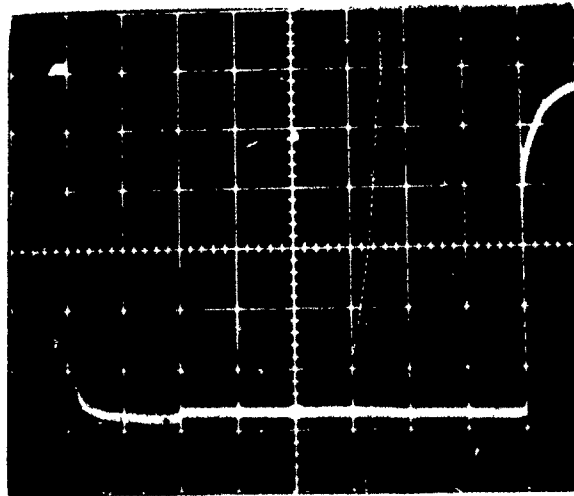


Input Pulse 50 V/div., 20 ns/div.

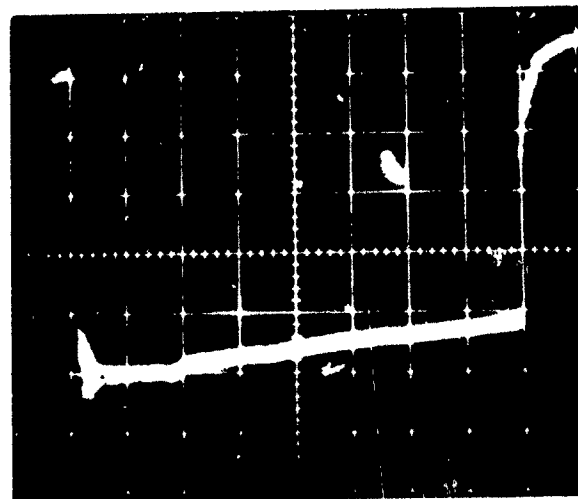


Transmitted Pulse 50 V/div., 20 ns/div.

Figure 2.3. Input and Output Pulses for 50 ohm Transmission Line Geometry using 1 kV Rep. Rate Pulser



Input Pulse 100 V/div., 50 ns/div.



Voltage Monitor Output 10 mV/div., 50 ns/div.

Figure 2.4. Voltage Monitor Response with 50 ohm Transmission Line Geometry using 1 kV Rep. Rate Pulser

Figure 2.4 shows the input voltage pulse and the corresponding output signal from the voltage monitor. Taking peak values, the resulting calibration coefficient is

$$G_V = 11.6 \frac{\text{KV}}{\text{Volt}}$$

To obtain the relevant value for the 4" shank configuration, the change in C_1 must be accounted for. When this is done using equation (2.5), the value obtained is

$$G_V = 9.65 \frac{\text{KV}}{\text{Volt}}$$

2.2.5 Matched Resistive Load Measurements

As indicated in Figure 2.1, energy flowing towards the load passes the voltage and current monitors on a coaxial transmission line which has (for a 4" diameter shank) a wave impedance of 41.5 ohms. If the load is a pure resistance equal to 41.5 ohms, no reflections will occur and the voltage and current recorded by the monitors will be identical to the voltage and current of the resistor.

A $41.2 \pm .4$ ohm copper sulphate load was placed on the end of the 4" shank extension of the SPI-PULSE 5000 and data obtained by charging the machine to 150 KV. Because the pulse forming line (the dielectric energy store) has a wave impedance of only about 2.0 ohms, the load is highly over-matched to the machine and the peak output voltage will be nearly 150 KV. The 519 oscilloscopes used to record the voltage and current monitors were calibrated using the SPI-PULSE 25 with the following results:

- Voltage Monitor Oscilloscope Sensitivity
10.1 Volts/division
- Current Monitor Oscilloscope Sensitivity
9.4 Volts/division

Figure 2.5 shows the voltage and current monitor traces obtained for a machine charging voltage of 150 KV. The ratio of the voltage monitor signal to the current monitor signal was measured to be constant to within $\pm 3\%$ throughout the duration of the signals recorded. Letting

A_I = voltage amplitude of current monitor signal

A_V = voltage amplitude of voltage monitor signal

G_I = current monitor calibration in amps/volt

then

$$G_V = 41.2 G_I \frac{A_I}{A_V}$$

Using measured values for A_I and A_V and the known value of G_I , there results

$$G_V = 9.84 \frac{KV}{VOLT}$$

2.2.6 Time Resolved Spectrometer Measurements

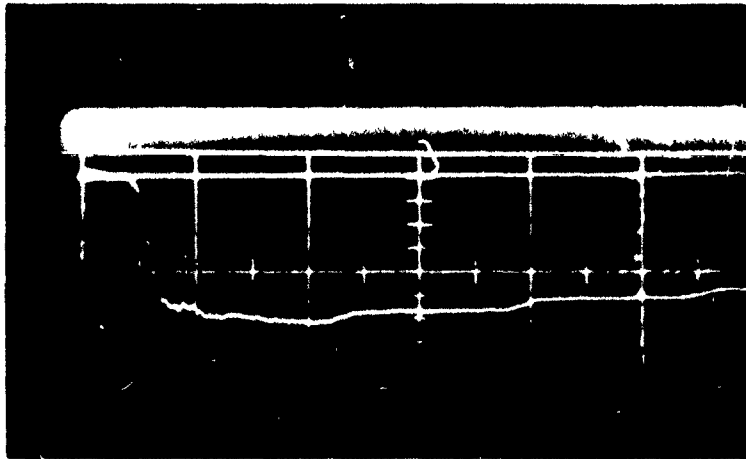
The time resolved spectrometer, described in the next section, was primarily intended for making direct measurements of the injected electron beam energy and angular distribution. However, from the data obtained it is also possible to infer the voltage monitor coefficient.

Figure 2.6 shows a comparison of the spectrometer output and the diode voltage. The upper curve shows the diode voltage as computed from the voltage monitor output using the coefficient

$$G_V = 9.7 \frac{KV}{VOLT}$$



Voltage Monitor Output 10.1 V/div., 20 ns/div.



Current Monitor Output 47 V/div., 20 ns/div.

Figure 2.5. SPI-PULSE 5000 Diode Voltage and Current Waveforms with 41 ohm Resistive Dummy Load at $V_o = 150$ KV

and including an inductive correction for the voltage drop along the shank between the monitor and the load (see Section 2.4). Because of the finite probe and collimating slit widths, each spectrometer probe has a finite energy acceptance range; so there is a small energy overlap between adjacent probes. The energy acceptance range, and corresponding time phasing, of each probe is indicated by the rectangular boxes on the upper curve. The 0.25 mil thick Mylar window used in this case causes negligible energy degradation for the beam energies indicated, so this correction has not been included.

The lower part of Figure 2.6 shows the measured time phasing of the four highest energy spectrometer probes. The time overlap between adjacent probes is in excellent agreement with that predicted by the voltage monitor output. Based upon this, it can be inferred that the voltage monitor coefficient given above is consistent with the spectrometer data.

2.2.7 Summary of Voltage Monitor Calibrations

The results of all voltage monitor coefficient measurements is summarized in Table 2.1.

Table 2.1 Voltage Monitor Calibration Values

Calibration Technique	Results (KV/V)
Step Function Voltage	9.0
RC Decay Time	9.7
Capacitive Bridge	10.1
Matched Transmission Line	9.65
Matched Resistive Load	9.84
Time Resolved Spectrometer	9.7
AVERAGE VALUE	9.7

The average value has been rounded to the first decimal place; the estimated accuracy of the average value is $\pm 7\%$.

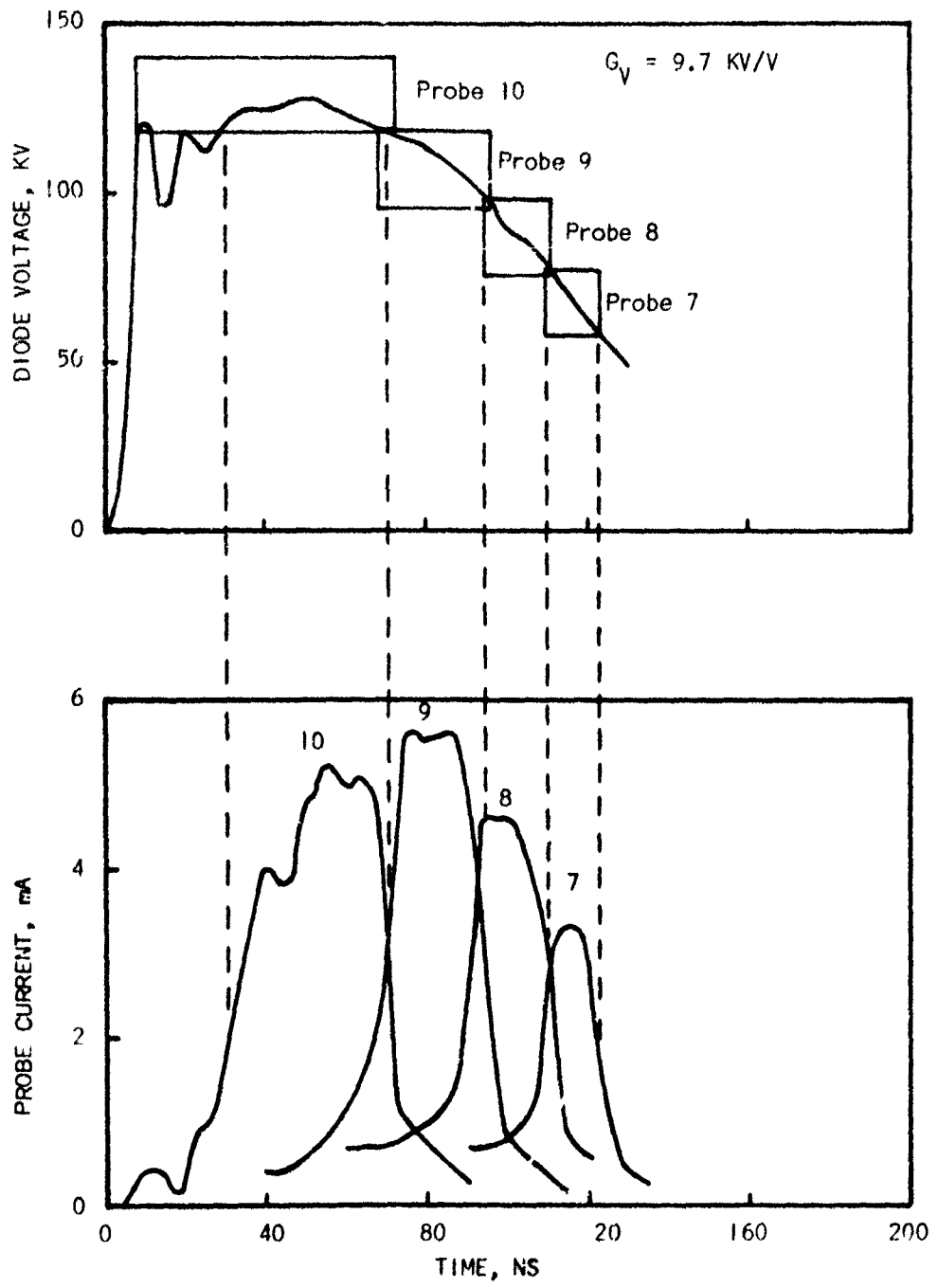


Figure 2.6 Comparison of Time Resolved Spectrometer Output and Measured Diode Voltage (Corrected for Inductive Component) for $\tau = 100 \text{ ns}$ (fwhm)

2.3 CURRENT MONITOR CALIBRATION

The other important diagnostic tool used for characterizing the electron beam is the resistive current shunt. As indicated in Figure 2.1, this consists of a low impedance resistor band placed in series with the outer conductor of the coaxial line feeding energy to the load. The voltage generated across the band is monitored with a Tektronix 519 oscilloscope. Any current pulse flowing on the cathode shank will induce an equal and opposite current in the outer conductor. This is a general property of transmission lines, and is physically caused by the fact that the magnetic field - B_{θ} - associated with the current flow on the shank induces current flow in the outer wall.

From the known number of resistors in the current monitor, its calibration can be easily calculated to be

$$G_1 = \frac{1}{R} = \frac{211}{3.3} = 63.9 \text{ amps/volt}$$

This section reviews the two techniques used to verify this.

2.3.1 Resistive Bridge Measurement

Using a calibrated GR resistive bridge, it was possible to directly measure the resistance of the current shunt. The value determined was

$$R = 16 \times 10^{-3} \text{ ohms}$$

However, the lowest bridge sensitivity is $\pm 1 \times 10^{-3}$ ohms; therefore the current monitor coefficient is

$$C_1 = 62.5 \pm 3.7 \text{ amps/volt}$$

2.3.2 Matched Transmission Line

Using the 50 ohm transmission line geometry described in Section 2.2.4, it is also possible to calibrate the current monitor. Since the amplitude

of the voltage pulse - V_p - on the line is known, and no reflections occur in the matched 50 ohm system, the current flowing both on the inner coaxial line and through the current monitor is

$$I_p = V_p/Z = 0.02 V_p$$

By measuring the voltage - V_1 - induced across the current monitor, the coefficient

$$G_1 = \frac{I_p}{V_1}$$

can be determined. Figure 2.7 shows measured waveforms; from these there results

$$G_1 = 60.6 \pm 4.2 \text{ amps/volt}$$

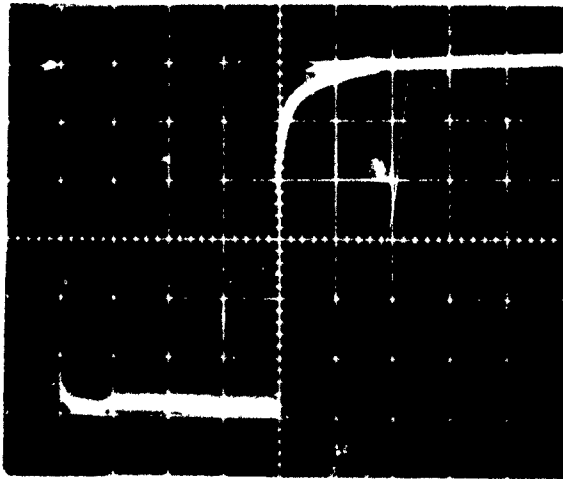
2.3.3 Summary of Current Monitor Calibration

Table 2.2 summarizes the current monitor calibrations determined by three techniques.

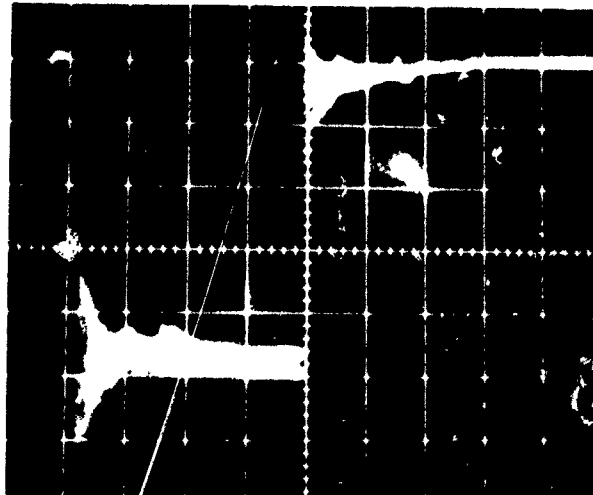
Table 2.2 Current Monitor Calibration Values

Measurement Techniques	Result (A/V)
Number of Resistors	63.9
Bridge Measurement	62.5 \pm 3.7
Matched Transmission Line	60.6 \pm 4.2
AVERAGE VALUE	62.3 \pm 2.2

One further consideration of the current monitor is warranted. Because of its physical construction the resistor band is shunted by a capacitor C. The equivalent monitor circuit is a parallel RC network driven by a current



Input Pulse 50 V/div., 100 ns/div.



Current Monitor Output 20 mV/div., 100 ns/div.

Figure 2.7. Current Monitor Calibration for 50 ohm Transmission Line Geometry using 1 kV Rep. Rate Pulser

source. The voltage - V_1 - across the monitor is then described by the equation

$$V_1(t) = \frac{1}{C} \int_0^t e^{-\frac{(t-t')}{\tau}} I(t') dt' \quad (2.7)$$

where

$$\tau = RC = \frac{C}{G_1}$$

Equation (2.7) can be integrated by parts to give

$$V_1(t) = \frac{I(t)}{G_1} - \frac{1}{G_1} \int_0^t e^{-\frac{(t-t')}{\tau}} \frac{dI}{dt'} dt' \quad (2.8)$$

To estimate the magnitude of the integral term, assume a current ramp of the form

$$I(t) = I_M t/t_r \quad (2.9)$$

Then

$$V_1(t) = \frac{I_M}{G_1} t/t_r - \frac{I_M}{G_1} \frac{\tau}{t_r} (1 - e^{-t/\tau}) \quad (2.10)$$

The estimated value for the shunting capacitance is

$$C = 12 \text{ pF}$$

The time constant is then

$$\tau = 0.2 \text{ picoseconds}$$

The capacitor clearly has a negligible effect on the measurement.

2.4 INDUCTIVE VOLTAGE CORRECTION

Referring again to Figure 2.1, the voltage and current diagnostics used actually measure V_M and I_M on a portion of the coaxial transmission line which is some distance removed from the actual electron beam load. Since the effective load resistance is typically much less than the wave impedance of the transmission line, voltage reflections occur which constitute part of the voltage monitor signal. In general, the voltage monitor does not uniquely determine the load voltage.

Since typical current pulses rise in several tens of nanoseconds, the short length of transmission line between the monitors and load is usually represented by an equivalent lumped inductance. If the length of line segment is l , then the equivalent inductance is

$$L = (2 \times 10^{-7} \ln \frac{r_o}{r_i}) l \quad (2.11)$$

where r_o and r_i are the outer and inner radii of the transmission line. Then the load (diode) voltage is

$$V_D(t) = V_M(t) - L \frac{dI_M}{dt} \quad (2.12)$$

To verify the validity of the inductive correction, the transmission line code⁽¹⁾ was used to model the SPI-PULSE 5000. The code was set up to print out the voltage and current waveforms at the position of the actual monitors. In addition, the actual load voltage was printed out. The computer generated voltage monitor signal was corrected for the inductive drop, using the computer generated current monitor signal, by employing a simple three point differencing scheme to compute the current derivative. Figure 2.8 summarizes the results. The solid line shows the actual load voltage, while the dot-dash line corresponds to the voltage monitor output. The dashed curve is the result of applying the inductive correction to the voltage monitor signal. It is clear that this technique reproduces the actual load voltage quite well; the small oscillations about the true value largely reflect numerical inaccuracies in computing the current derivative.

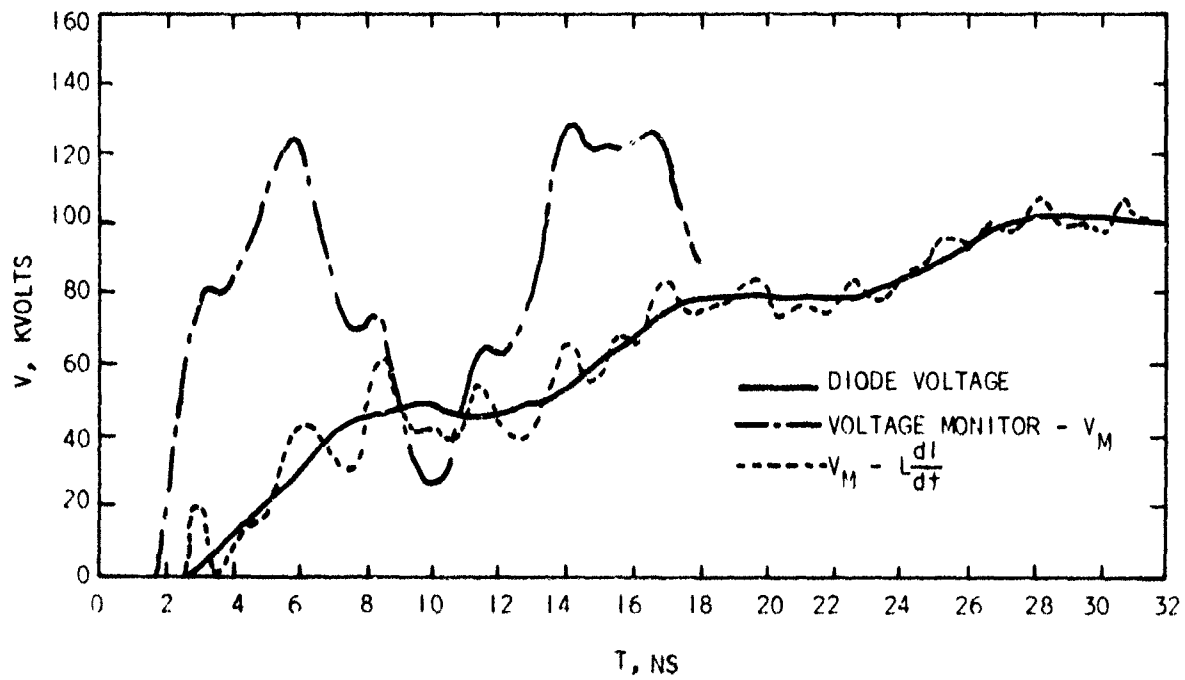


Figure 2.8. Comparison of Code Calculated Diode Voltage to Measured Diode Voltage Corrected for Inductive Component

Based upon this study, it can be concluded that the inductive voltage correction is sufficient to compute the true load voltage.

2.5 SUMMARY OF CALIBRATION RESULTS

Based upon a thorough study of the SPI-PULSE 5000 diagnostics, the following results apply for the 12" diameter diode configuration:

- the voltage monitor coefficient is 9.7 ± 0.6 KV/V
- the current monitor coefficient is 62.3 ± 2.2 amps/volt
- a simple inductive voltage correction accurately determines the true diode voltage.
- because of the agreement between low voltage and high voltage measurements of the voltage monitor coefficient, it can be concluded that if shank emission of electrons is occurring it has a negligible effect on the voltage monitor output.

SECTION III
CAVITY TRANSPORT - BENCHMARK EXPERIMENTS

3.1 INTRODUCTION

An experimental program was carried out to provide data, for fixed cavity geometries, which could be compared to IEMP transport code predictions. A major requirement of the program was that the injected beam parameters be accurately determined. In this section the techniques used are described and the data resulting from the measurements presented.

3.2 EXPERIMENTAL CONFIGURATION AND TEST MATRIX

The equipment used is shown schematically in Figure 3.1. The SPI-PULSE 5000 accelerator served as the injected electron source. The machine charging voltage was held constant at 250 kV and the gap between the 30 cm diameter cathode and tungsten mesh/0.25 mil aluminized Mylar anode set at 1.5 cm. To produce a short injected pulsewidth, the diode pressure was maintained at 40 μ (air).

The cavity itself consisted of a 30 cm diameter right cylindrical sleeve mounted on insulating supports inside a larger diameter vacuum chamber. The mesh/mylar anode through which the electron beam was injected served as one end of the cavity. The other end of the cavity was defined by a moveable aluminum current collector plate. This plate was electrically isolated from the cavity side wall by a low impedance resistor band. The voltage induced across the band is then directly proportional to the net current transported through the cavity. The wall current monitor was not used during these runs.

The experiment was designed to assess the dependence of current transport on two variables: cavity depth and residual gas pressure in the cavity. The complete test matrix is shown in Table 3.1. Because of time limitations, only a portion of the data has been reduced.

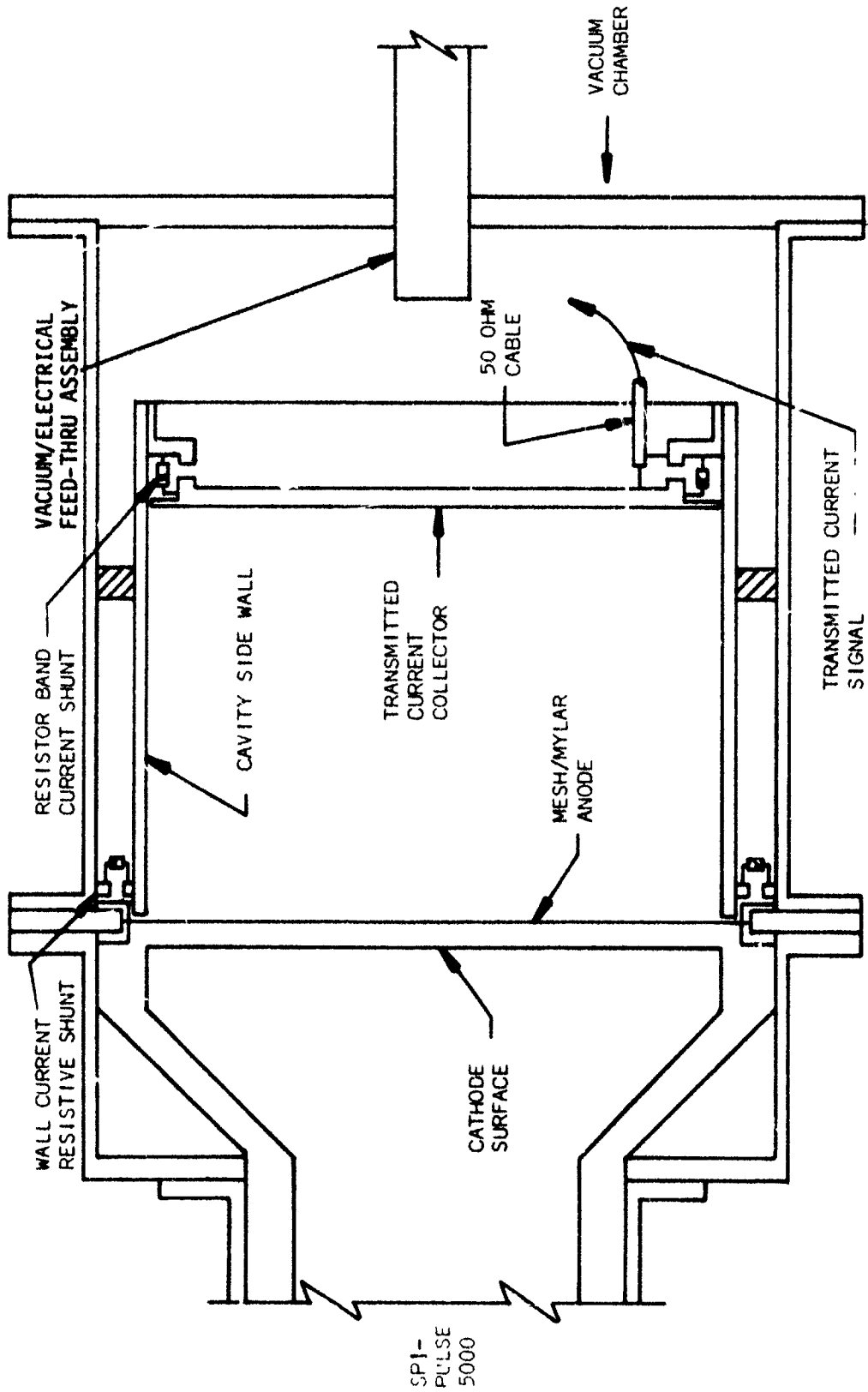


Figure 3.1. Schematic of Typical Configuration for IEMP Benchmark Experiments

3.3 INJECTED BEAM PARAMETERS

In order to obviate any problems in computing cavity parameters because of erroneous input data, it was necessary to very carefully determine the time dependent beam injection parameters. Specifically, these are energy, current, current density distribution, energy spread and electron angular spread. The following sub-sections consider each in detail.

3.3.1 Diode Measurements

From the results described in Section 2, it is possible to calculate the actual diode voltage and current. Figure 3.2 shows typical data; the upper curves show the observed voltage monitor and current time dependence. The voltage curve has been corrected for the integral term in equation 2.2 to give the cathode shank voltage. Using the inductive correction described previously, with an inductance value of 21 nH, the lower curve results. This gives the time history of the main accelerating voltage in the anode/cathode gap.

3.3.2 Injected Current

Determination of the injected beam current was found to depend critically on where it was measured. Referring to Figure 3.1, the cavity side wall was positioned 1.0 mm away from the injection plane. Because the moveable back current collector was not perfectly perpendicular to the cavity axis (the collector was cocked by ± 0.5 mm), the closest spacing was 1.0 mm. Measurements made at this location and at succeeding greater spacings, are shown in Figure 3.3.

The results, which were quite reproducible, show a strong dependence of transmitted current on cavity depth for times greater than 50 ns. The current density is roughly 5 amps/cm² at that point; from Figure 3.2 the beam energy is less than 40 keV. Since

TABLE 3.1 IEMP BENCHMARK EXPERIMENT DATA STATUS AUGUST 1975

<u>NOMINAL BEAM CHARACTERISTICS</u>																																																																																																																																													
Pulse Width = 35 ns (FWHM)																																																																																																																																													
Injected Current Density (peak) = 3.0 amps/cm ²																																																																																																																																													
Injected Beam Energy (average) = 100 keV																																																																																																																																													
<u>FIXED DIODE PARAMETERS</u>	<u>FIXED CAVITY PARAMETERS</u>																																																																																																																																												
Cathode Diameter = 30 cm.	Cavity Diameter = 30 cm																																																																																																																																												
Anode = 65% transparent mesh and 0.25 mil Al-Mylar																																																																																																																																													
Anode/Cathode gap = 1.5 cm																																																																																																																																													
Diode Pressure = 40 μ																																																																																																																																													
<u>TEST MATRIX</u>																																																																																																																																													
	CAVITY DEPTH, CM																																																																																																																																												
	<table border="1"> <thead> <tr> <th></th> <th>.1</th> <th>1</th> <th>2</th> <th>4</th> <th>7</th> <th>10</th> <th>15</th> <th>20</th> <th>30</th> </tr> </thead> <tbody> <tr> <th>.1</th> <td>X</td> <td>X</td> <td>X</td> <td>X</td> <td>X</td> <td>X</td> <td>X</td> <td></td> <td>X</td> </tr> <tr> <th>1</th> <td></td> <td></td> <td>X</td> <td></td> <td>X</td> <td></td> <td>X</td> <td></td> <td>X</td> </tr> <tr> <th>5</th> <td></td> <td></td> <td>X</td> <td></td> <td>X</td> <td></td> <td>X</td> <td></td> <td>X</td> </tr> <tr> <th>10</th> <td></td> <td></td> <td>X</td> <td></td> <td>X</td> <td></td> <td>X</td> <td></td> <td>X</td> </tr> <tr> <th>20</th> <td></td> <td></td> <td>X</td> <td></td> <td>X</td> <td></td> <td>X</td> <td></td> <td>X</td> </tr> <tr> <th>30</th> <td></td> <td></td> <td>X</td> <td></td> <td>X</td> <td></td> <td>X</td> <td></td> <td>X</td> </tr> <tr> <th>50</th> <td></td> <td></td> <td>X</td> <td></td> <td>X</td> <td></td> <td>X</td> <td></td> <td>X</td> </tr> <tr> <th>70</th> <td></td> <td></td> <td>X</td> <td></td> <td>X</td> <td></td> <td>X</td> <td></td> <td>X</td> </tr> <tr> <th>100</th> <td></td> <td></td> <td>X</td> <td></td> <td>X</td> <td></td> <td>X</td> <td></td> <td>X</td> </tr> <tr> <th>200</th> <td></td> <td></td> <td>X</td> <td></td> <td>X</td> <td></td> <td>X</td> <td></td> <td>X</td> </tr> <tr> <th>350</th> <td></td> <td></td> <td>X</td> <td></td> <td>X</td> <td></td> <td>X</td> <td></td> <td>X</td> </tr> <tr> <th>500</th> <td></td> <td></td> <td>X</td> <td></td> <td>X</td> <td></td> <td>X</td> <td></td> <td>X</td> </tr> <tr> <th>1000</th> <td></td> <td></td> <td>X</td> <td></td> <td>X</td> <td></td> <td></td> <td></td> <td></td> </tr> </tbody> </table>		.1	1	2	4	7	10	15	20	30	.1	X	X	X	X	X	X	X		X	1			X		X		X		X	5			X		X		X		X	10			X		X		X		X	20			X		X		X		X	30			X		X		X		X	50			X		X		X		X	70			X		X		X		X	100			X		X		X		X	200			X		X		X		X	350			X		X		X		X	500			X		X		X		X	1000			X		X				
	.1	1	2	4	7	10	15	20	30																																																																																																																																				
.1	X	X	X	X	X	X	X		X																																																																																																																																				
1			X		X		X		X																																																																																																																																				
5			X		X		X		X																																																																																																																																				
10			X		X		X		X																																																																																																																																				
20			X		X		X		X																																																																																																																																				
30			X		X		X		X																																																																																																																																				
50			X		X		X		X																																																																																																																																				
70			X		X		X		X																																																																																																																																				
100			X		X		X		X																																																																																																																																				
200			X		X		X		X																																																																																																																																				
350			X		X		X		X																																																																																																																																				
500			X		X		X		X																																																																																																																																				
1000			X		X																																																																																																																																								
CAVITY PRESSURE, μ																																																																																																																																													
<u>MEASUREMENTS</u>																																																																																																																																													
Diode Voltage and Current vs. Time																																																																																																																																													
Transmitted Cavity Current vs. Time																																																																																																																																													

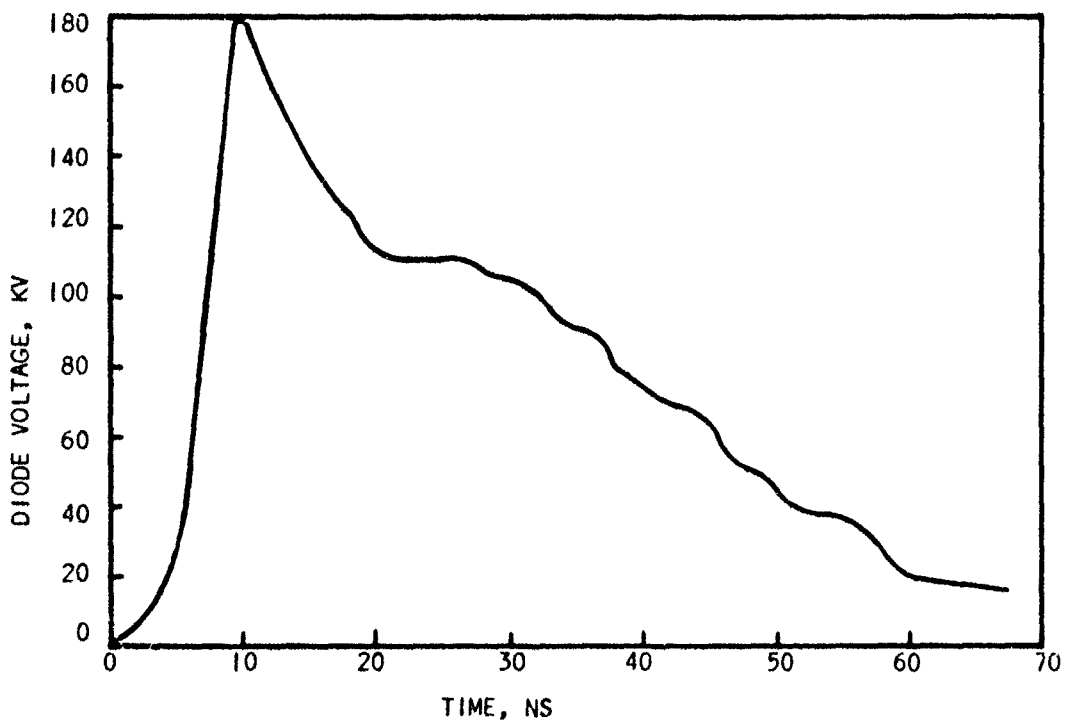
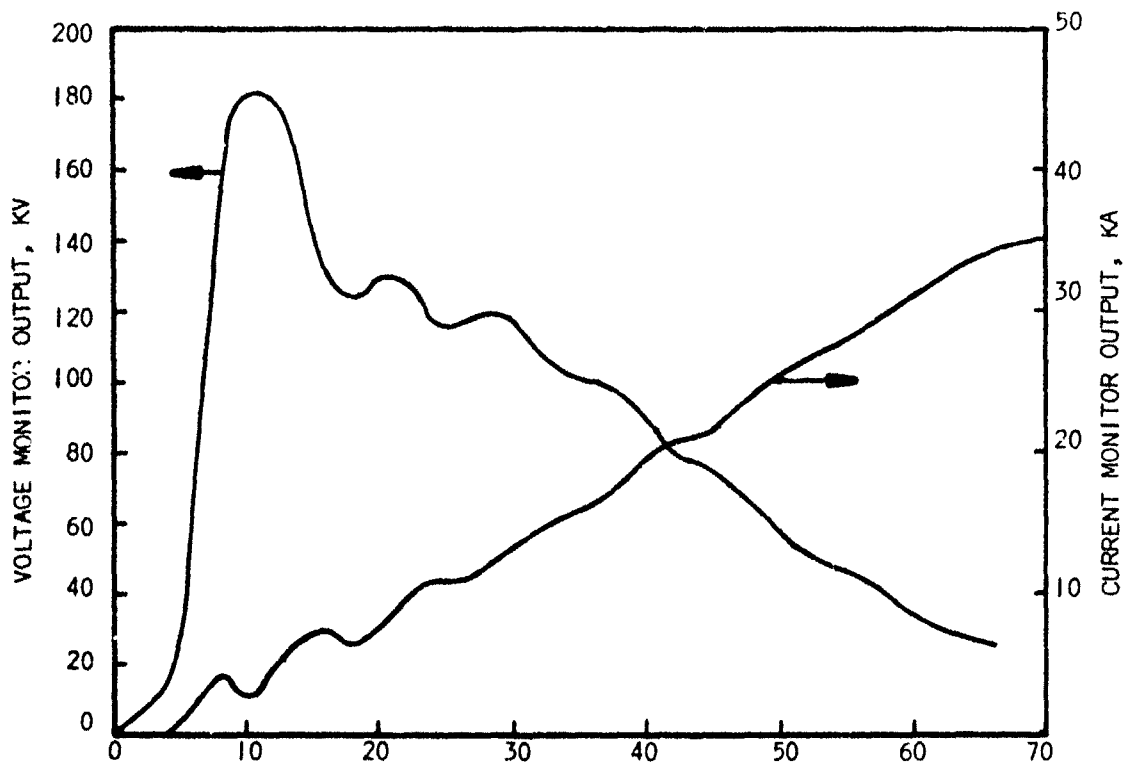


Figure 3.2. IEMP Benchmark Diode Current, Voltage and Inductance Corrected Diode Voltage Waveforms for $\tau = 35$ ns (fwhm)

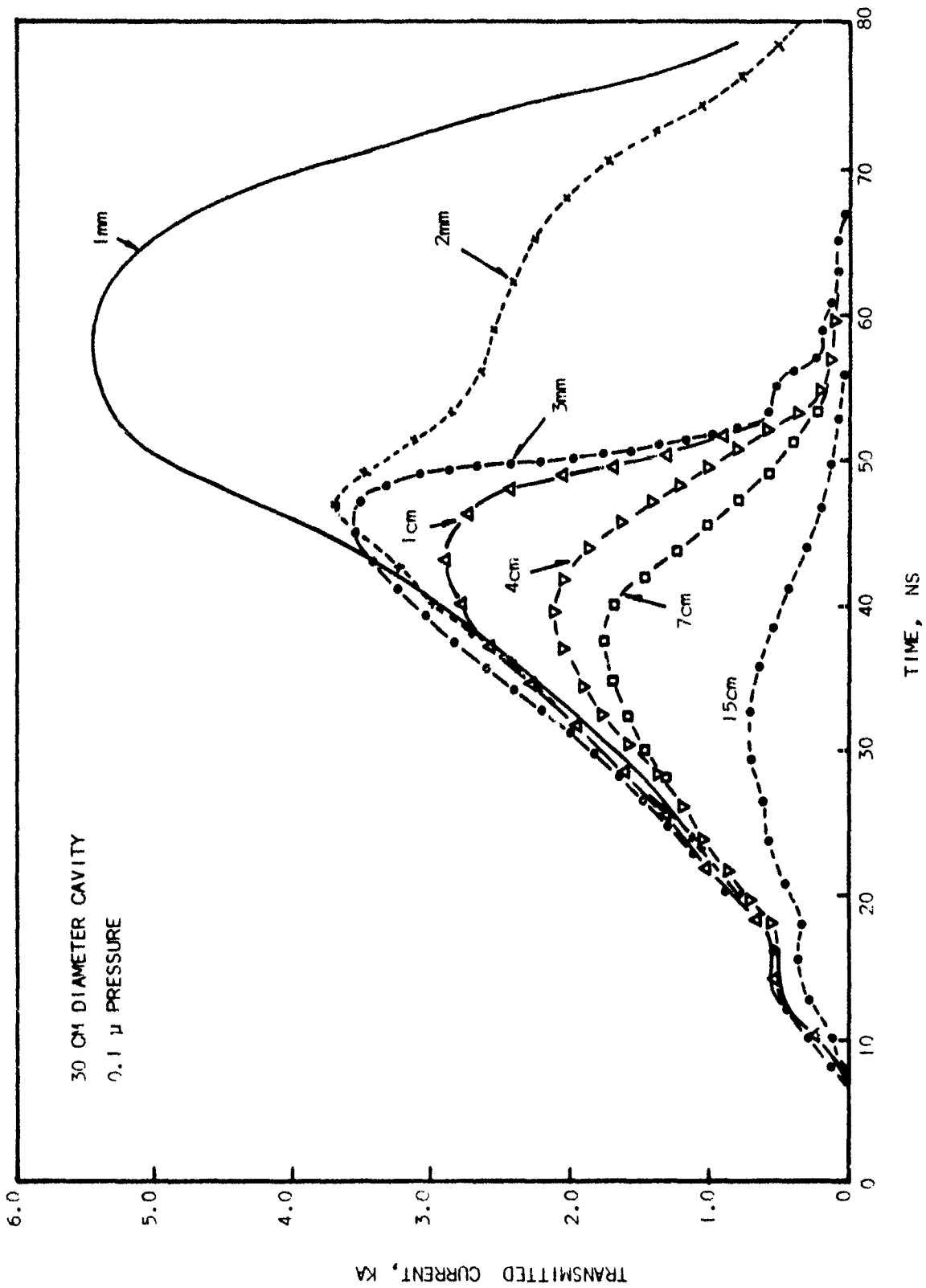


Figure 3.3. Dependence of Vacuum Transmitted Current on Cavity Depth

$$\frac{J \ell^2}{2.34 \times 10^{-6} V^{3/2}} \approx \frac{1}{25}$$

it is surprising that strong space charge limiting should be observed. This may be due to the annularity of the beam as will be described. The current pulse measured 1 mm from the injection plane is taken to be the actual injected beam current.

3.3.3 Angular and Energy Spread

Because a Mylar pressure diaphragm was used at the injection plane, electrons traversing it will be degraded in energy and have their direction of injection randomized. To study this, a Monte Carlo transport code - ELTRAN⁽²⁾ - was employed. For a given electron energy incident on the Mylar, the injected beam was characterized in the following way:

- the energy loss incurred by 25% or less, 50% or less, and 75% or less of the electrons.
- the polar angle deflection incurred by 25% or less, 50% or less, and 75% or less of the electrons.

The energy loss curves are shown in Figure 3.4; the values given should be subtracted from the initial energy to give the injected energy of the corresponding particle group. The corresponding curves for polar angle deflection (assumed to be azimuthally symmetric) are contained in Figure 3.5.

3.3.4 Magnetic Spectrometer Measurements

In order to directly measure the injected electron beam energy, or energy distribution, at each instant of time, a time resolved magnetic spectrometer system was designed and built. Table 3.2 summarizes the spectrometer measurement test matrix. Reference to long pulse width spectrometer data was made in Section 2. In this section, a discussion is presented of the spectrometer design and calibration. This is followed by considerations on the short pulsewidth benchmark beam results.

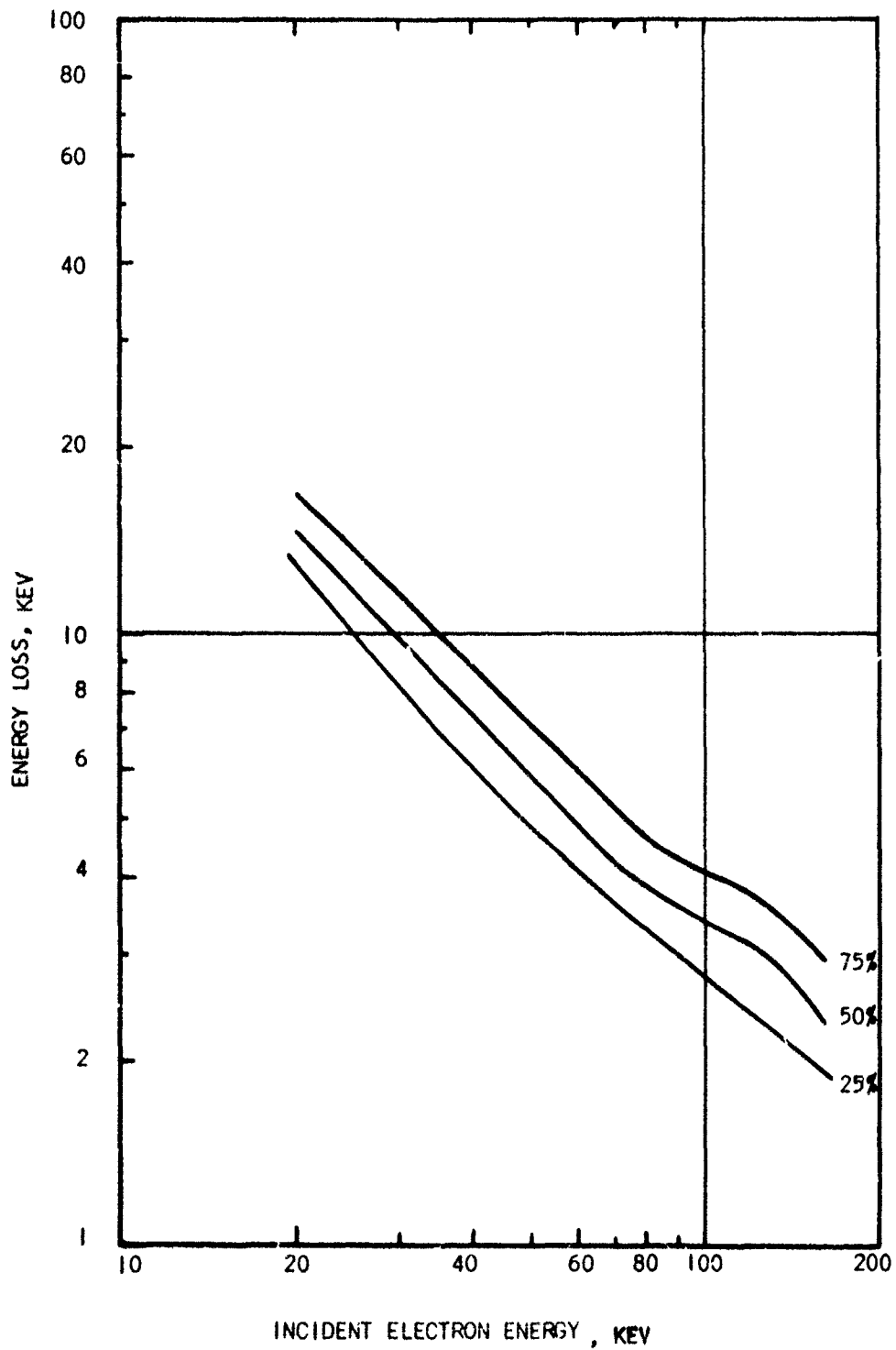


Figure 3.4 Energy Loss Curves In 0.25 mil Mylar By 25%, 50% and 75% of the Electrons (Eltran Calculation)

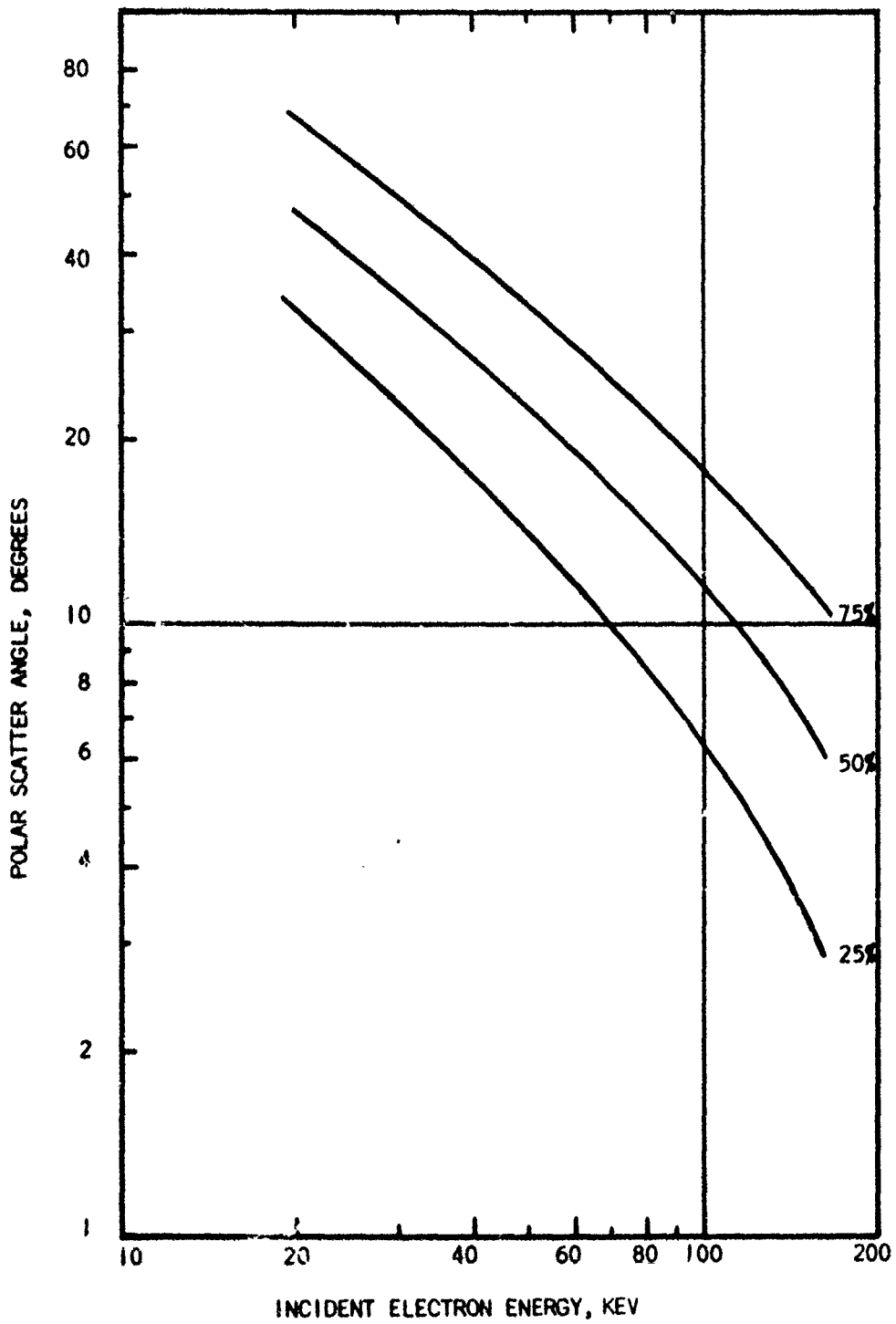


Figure 3.5. Polar Scattering Distributions In 0.25 mil Mylar for 25%, 50% and 75% of the Electrons (Eltran Calculation)

Table 3.2 Time Resolved Spectrometer Measurements Summary

LONG PULSE - 100 ns

		2 mm Drift 0.1 μ				1 cm Drift 0.1 μ			
		0°	30°	45°	60°	0°	30°	45°	60°
RADIAL POSITION	0 cm	X	X	X		X	X		X
	12.7 cm	X				X			

		10 cm Drift 0°	
		0.1 μ	100 μ
RADIAL POSITION	0 cm	X	X
	12.7 cm	X	X

SHORT PULSE - 35 ns

		2 mm Drift 0.1				1 cm Drift 0.1			
		0°	30°	45°	60°	0°	30°	45°	60°
RADIAL POSITION	0 cm	X				X	X		X
	12.7 cm								

3.3.4.1 Spectrometer Design

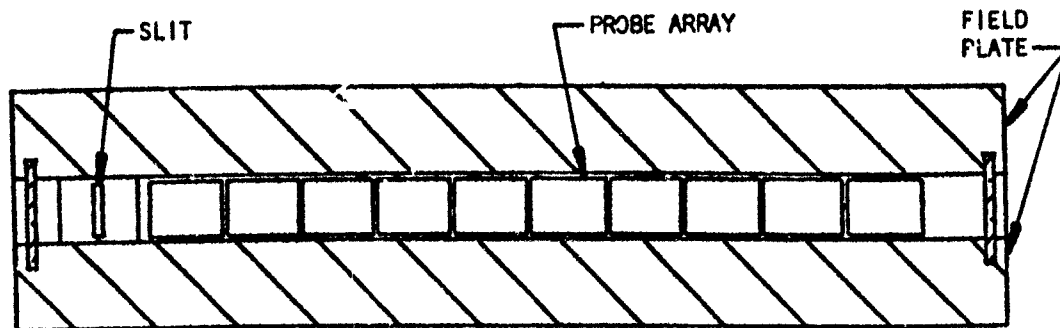
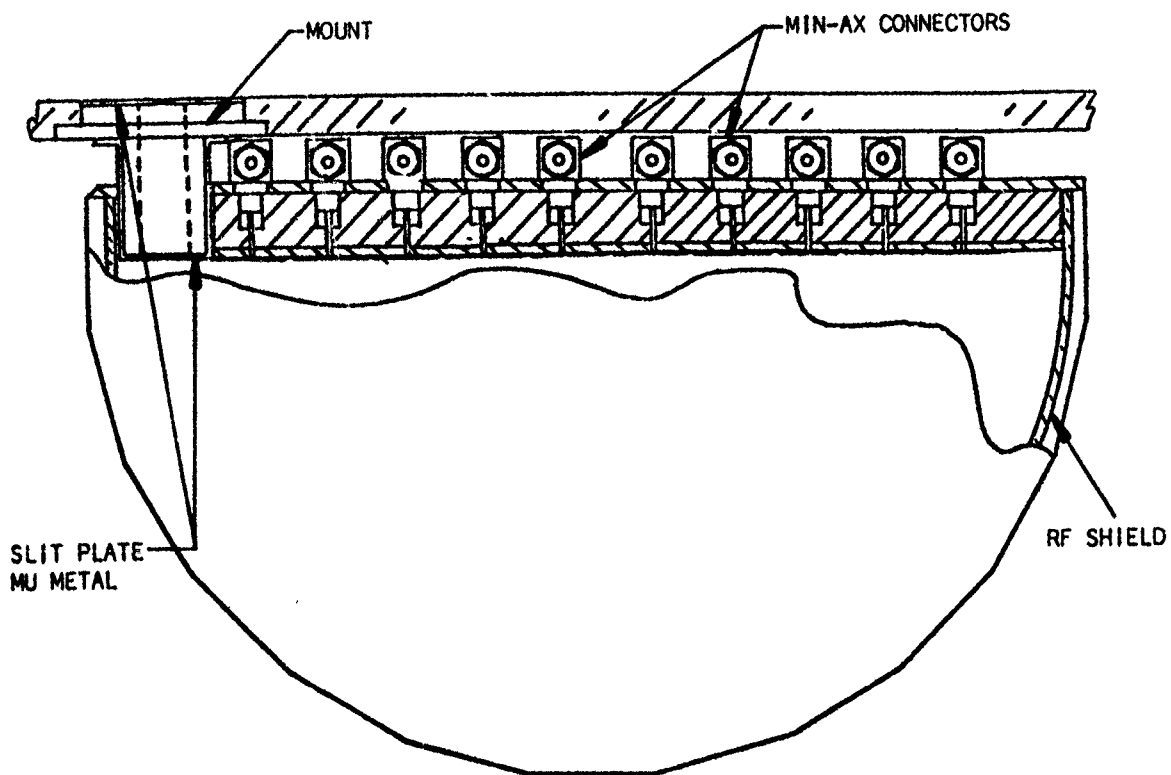
The 180° magnetic spectrometer utilizes a permanent magnet array to provide a uniform field between two 6 inch diameter semicircular pole plates. Figure 3.6 shows the spectrometer to scale in two views. The probe configuration shown was designed to provide ten channels of time-resolved information. A miniature coax angle connector is located directly behind each probe on an aluminum mounting plate which, with the peripheral band, provides an RF tight enclosure. This peripheral band also serves to hold the pole plates at 1 cm separation. The probes, approximately 1 cm² in area, are made of copper. The probes and the second slit are recessed from the edge of the pole plates a minimum of 1 cm in all directions to insure a normal field to the electron velocity at all points. The slit assembly consists of an aluminum mounting piece for good electrical grounding, with slits and sides of high permeability mu metal to eliminate any fields in the slit area. The slit separation is 2.5 cm. Slits of several dimensions were made to provide maximum resolution for a range of incident current densities.

The circumference of the pole plates has thirteen machined flats ~3/4 inch wide to accommodate the permanent magnets used to provide the field. The 3/4 x 1 5/16 inch magnets were also ground flat to provide maximum contact with the pole flats. Both pole plates and magnets were nickel plated to eliminate any oxidation. Four sets of thirteen magnets were made. Each set, having a different strength, was color-coded and numbered to reproduce configurations easily. Small plastic rectangular slabs, epoxied to the magnets, provide a press fit between the pole plates and secure the magnets in position.

Fields obtainable range from approximately 50 to 500 gauss. A Hall effect gaussmeter with a 1/8 x 3/16 inch probe was used to measure the field uniformity at various locations within the pole plates. A uniformity of $\pm 2\%$ was easily obtainable. At the same time, the field within the slit assembly was shown to be <2 gauss, i.e. no indication on the gaussmeter at higher sensitivity.

3.3.4.2 Spectrometer Probe Energy Resolution

From the average field value a calibration curve of electron energy versus arc diameter was calculated using the basic equation



ACTUAL SIZE SHOWN

Figure 3.6. SPI 180° Magnetic Spectrometer with 10 Time Resolved Channels

$$T_o = M_o C^2 \left[\sqrt{1 + \left(\frac{X_o B_o}{3410}\right)^2} - 1 \right] \quad (3.1)$$

where

T_o = electron kinetic energy in keV

$M_o C^2$ = electron rest energy = 511 keV

X_o = arc diameter in cm

B_o = magnetic field in gauss.

Also with the probe locations known with respect to the slit and given

W_p = probe width in cm

W_s = slit width in cm

S_s = slit separation in cm

the energy acceptance for each probe could be calculated from the equations

$$T_{MIN} = M_o C^2 \left[\sqrt{1 + \left(1 - \frac{W_p + W_s}{2 X_o}\right)^2 \left(\frac{X_o B_o}{3410}\right)^2} - 1 \right] \quad (3.2)$$

and

$$T_{MAX} = M_o C^2 \left[\sqrt{1 + \left(1 + \frac{W_p + W_s}{2 X_o \cos \alpha_o}\right)^2 \left(\frac{X_o B_o}{3410}\right)^2} - 1 \right] \quad (3.3)$$

where

$$\alpha_o = \tan^{-1} (W_s / S_s)$$

3.3.4.3 Spectrometer Calibration

An internal conversion beta source, Cd-109, with transition energies of 62.2 and 84.2 keV was used to verify the calculated calibration. A strip of Kodak Type AA Industrex X-ray film was placed at the probe plane with the source collimated by the narrow slits of the spectrometer. The film was exposed at two locations according to the energy of the betas in the form of a thin slightly blurred line. Figure 3.7 shows the calculated calibration curve with the position of the experimental lines indicated on the X-axis. The corresponding energies can be seen to agree to within 2% of the known values.

3.3.4.4 Thirty-Five ns Pulse Results

The work presented here was carried out about six weeks prior to performing the benchmark experiments. Because of a change in the instrument used to monitor diode pressure, the pulse length of the beam studied with the spectrometer was somewhat shorter than that used for the benchmark series of experiments. Nevertheless, the general conclusions reached are applicable to both cases.

Measurements were made approximately 2 mm beyond the Mylar pressure diaphragm. Figure 3.8 indicates the measured voltage monitor and current monitor waveforms. Using this data, correcting for the inductive voltage drop, and using the mean (50%) energy loss curve (Figure 3.4) the injected energy curve shown in Figure 3.9 was calculated. The energy/time acceptance of each spectrometer probe is indicated by a rectangular box. The lower graphs show the measured probe waveforms, with the spectrometer positioned to accept only electrons coming out normal to the anode.

The general agreement between the derived injected energy curve and spectrometer probe output is good; each probe signal peaks at essentially the center of its energy/time acceptance range. The early time tail of each probe can be accounted for by scatter from the edge of the entrance slit. Referring to equation (3.3) for the maximum energy acceptance of a probe, slit scatter can increase α_0 and thus increase the real energy acceptance of a probe. The late time tail cannot be accounted for by the same mechanism. While its origin

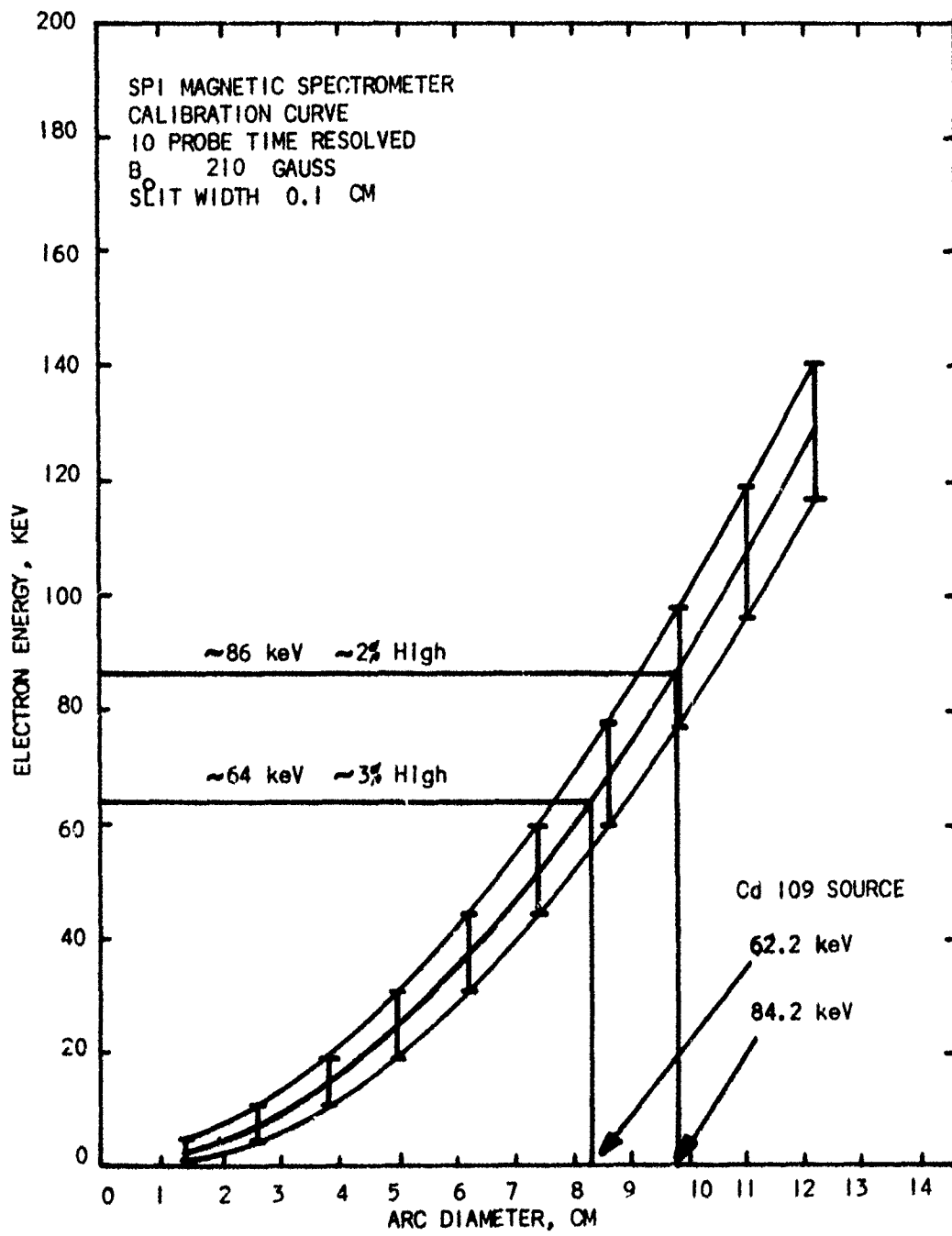


Figure 3.7 Internal Conversion Beta Source Calibration Compared to Calculated Calibration Curve for Magnetic Spectrometer

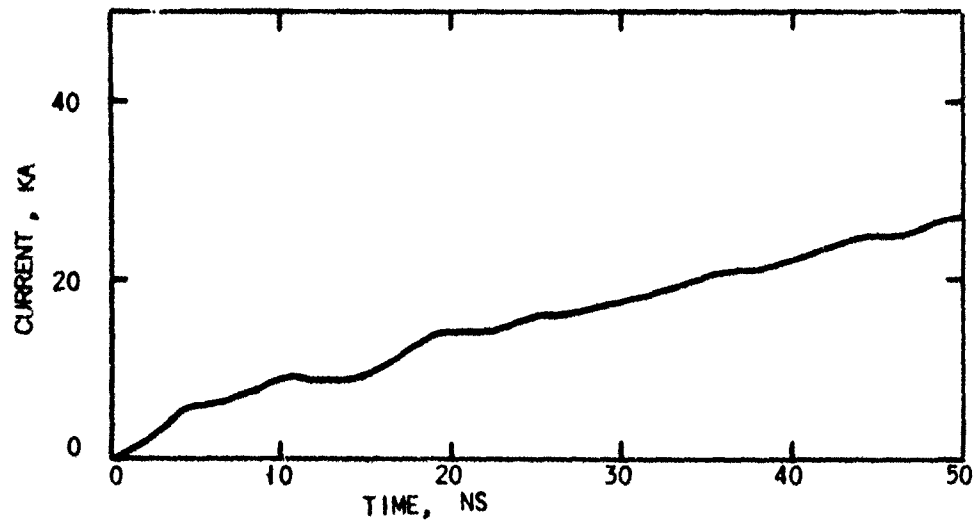
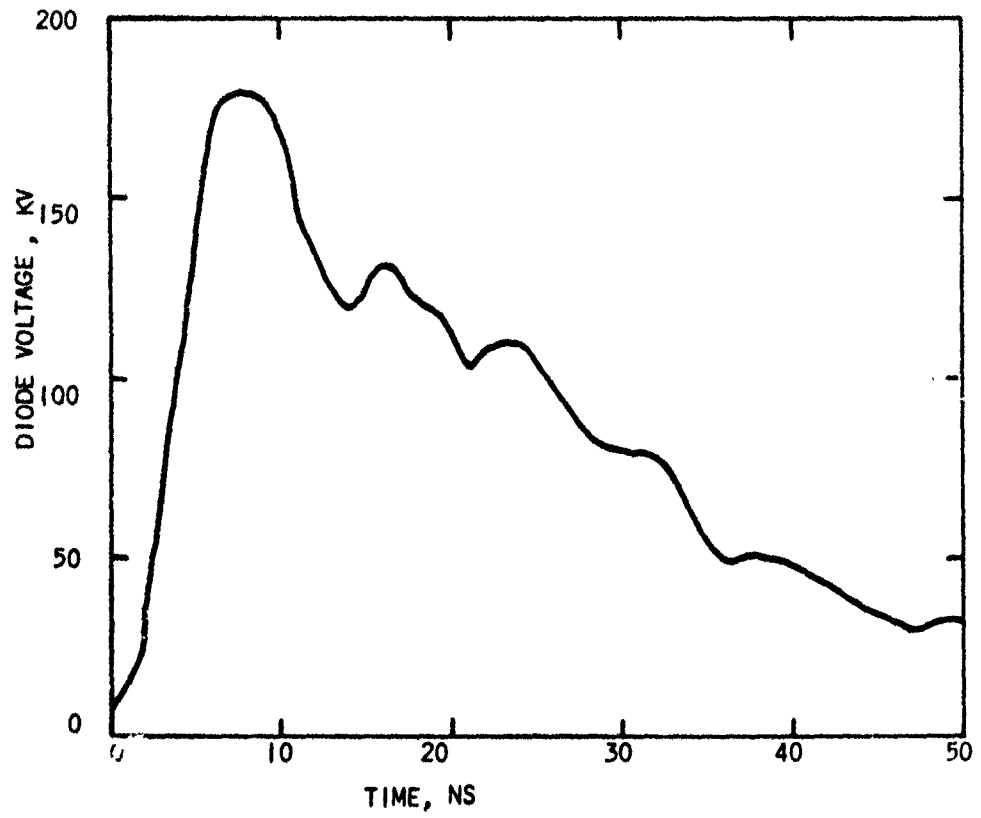


Figure 3.8 Diode Diagnostic Waveforms for 35 ns (fwhm) Pulse

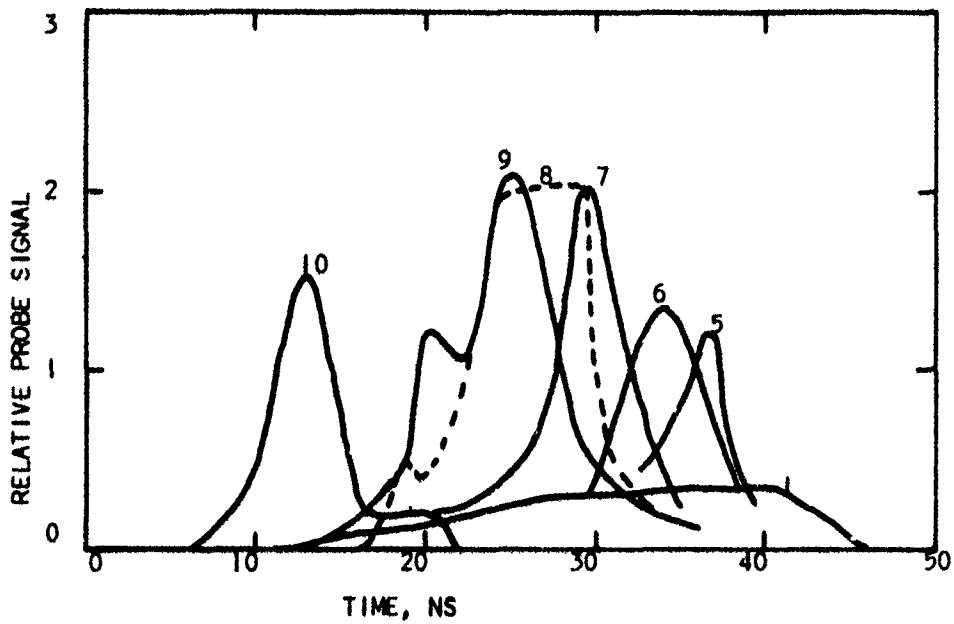
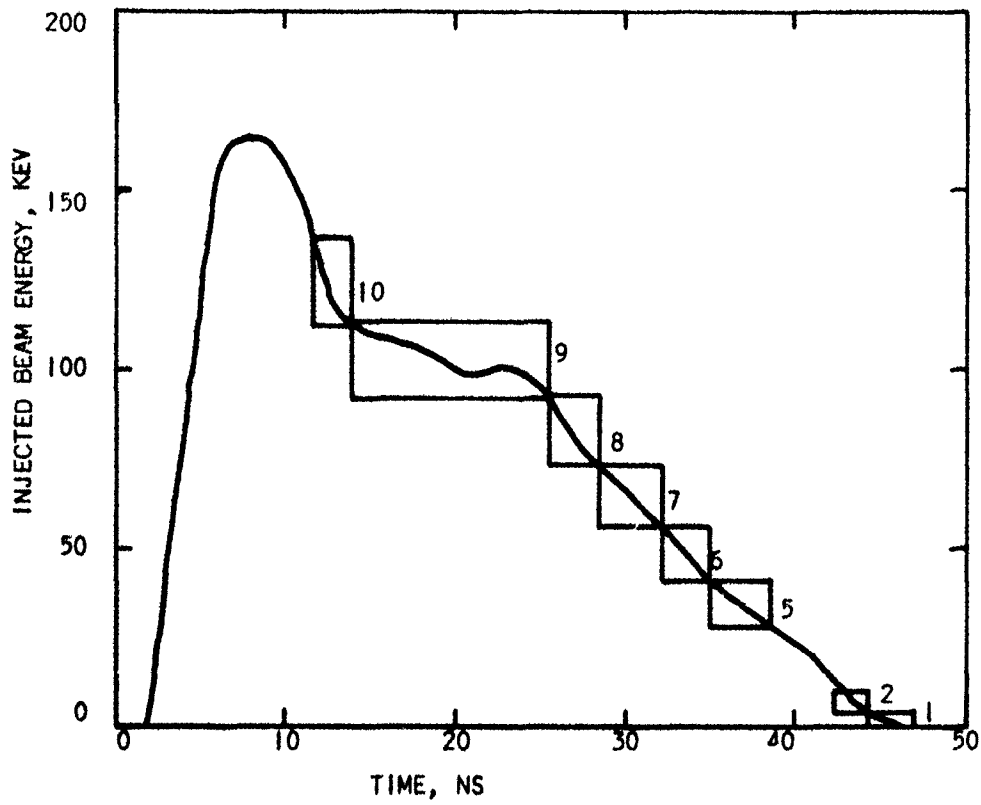


Figure 3.9 Comparison of Computed Injected Electron Energy and Spectrometer Probe Output

is not definitely known, it is likely that it is a result of secondary electron emission from the surface of the copper probes. Higher energy secondaries (a few keV energy) are bent by the magnetic field in such a way that they tend to strike higher energy probes. While not shown on Figure 3.9, all of the lower energy probes (1 through 5) have long early time tails which start at about 15 ns into the pulse.

Finally, another measurement was made with the spectrometer set to sample that portion of the injected beam scattered 30° to the anode normal. By integrating the output of each probe, the energy spectrum shown in Figure 3.10 was obtained. From Figure 3.5, one would not expect much of the beam to be scattered into this large an angle until the energy is well below 100 keV. The data substantiates this.

3.3.5 Injected Beam Parameters - Benchmark Experiments

During the series of measurements made to fill in the test matrix shown in Table 3.1, it was observed that the peak voltage monitor output varied by about $\pm 5\%$ and the injected beam current varied by $\pm 10\%$. Therefore an average set of waveforms was used to characterize the beam. These are shown in Figure 3.11.

To make code input convenient the beam variables were digitized every two nanoseconds, with the zero time shifted to correspond to the beginning of injected current. The beam energy was characterized by a two group distribution; the 25% and 75% points. A similar characterization was used for the injected beam polar angles. The Monte Carlo calculations described earlier were used to generate this grouping. It might be argued that the spectrometer data should have been used to determine the appropriate energy grouping; however, because of the effect of slit width it was not possible to determine the real energy spread at each time. Therefore, it was felt that use of the computer energy spread was a better approach.

Table 3.3 summarizes the injected beam parameters in digital form.

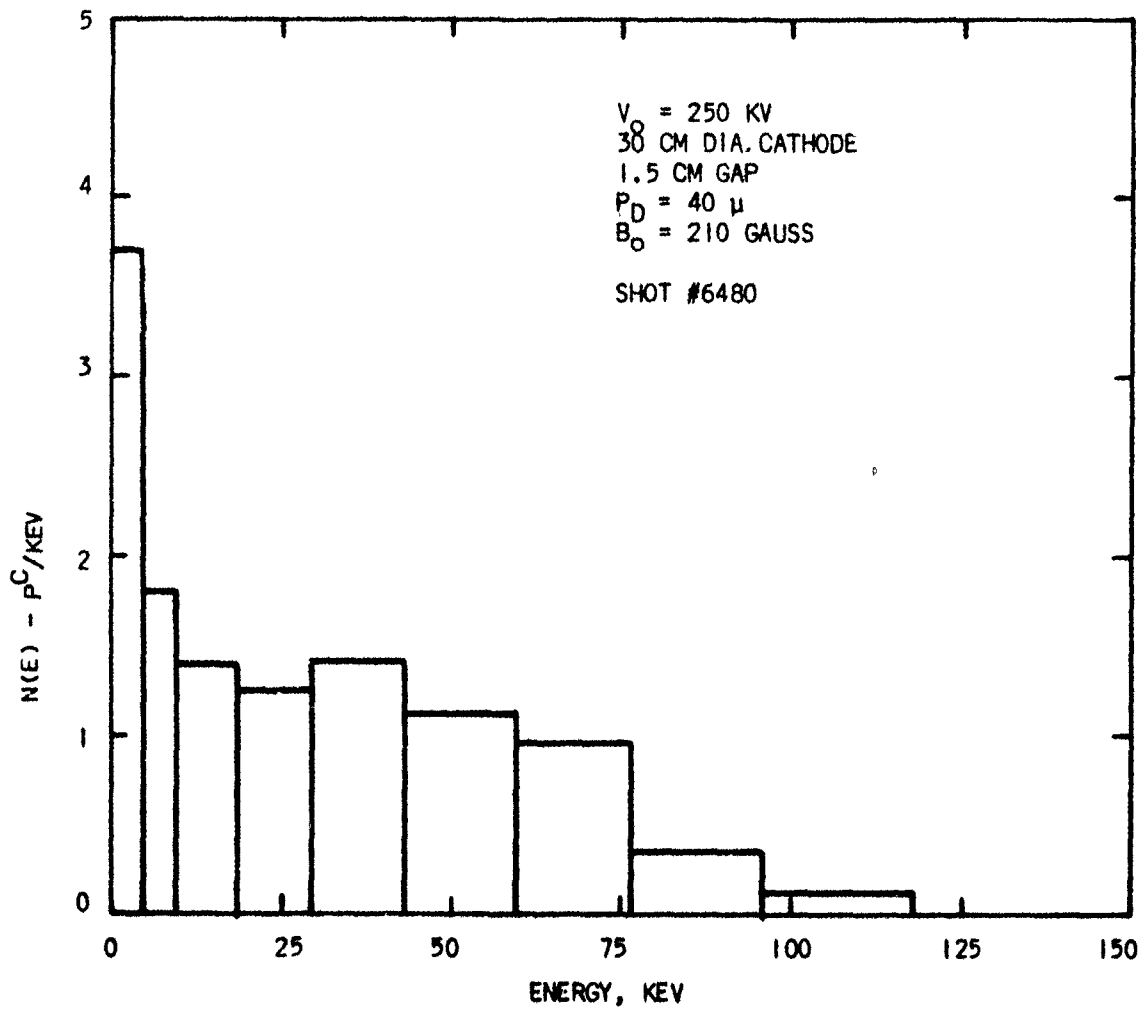


Figure 3.10 Measured Time Integrated Spectrum at 30°

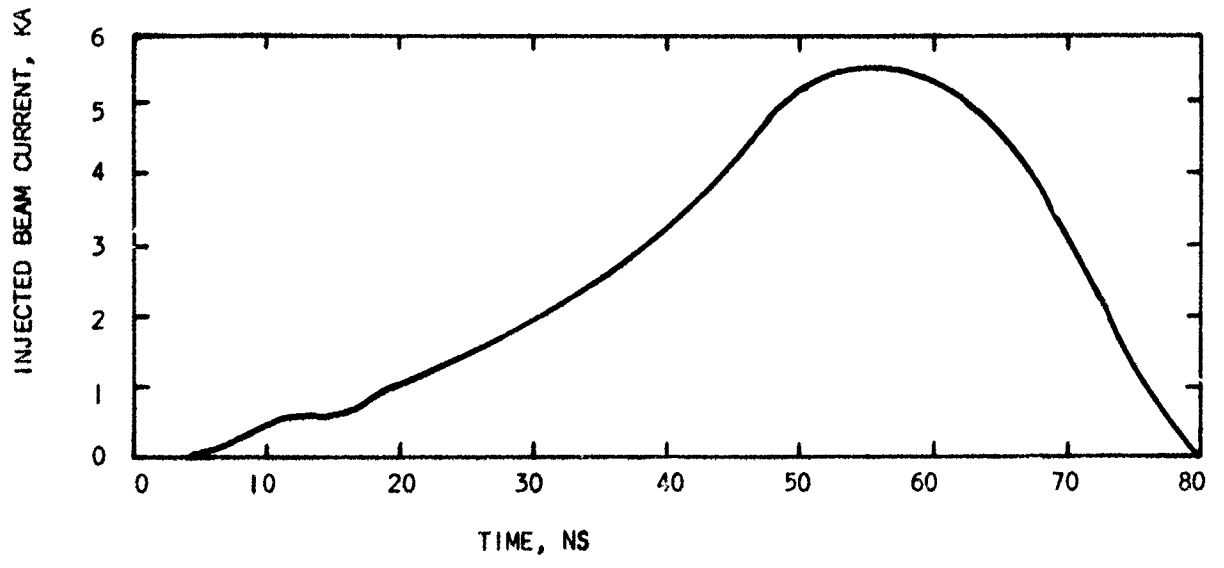
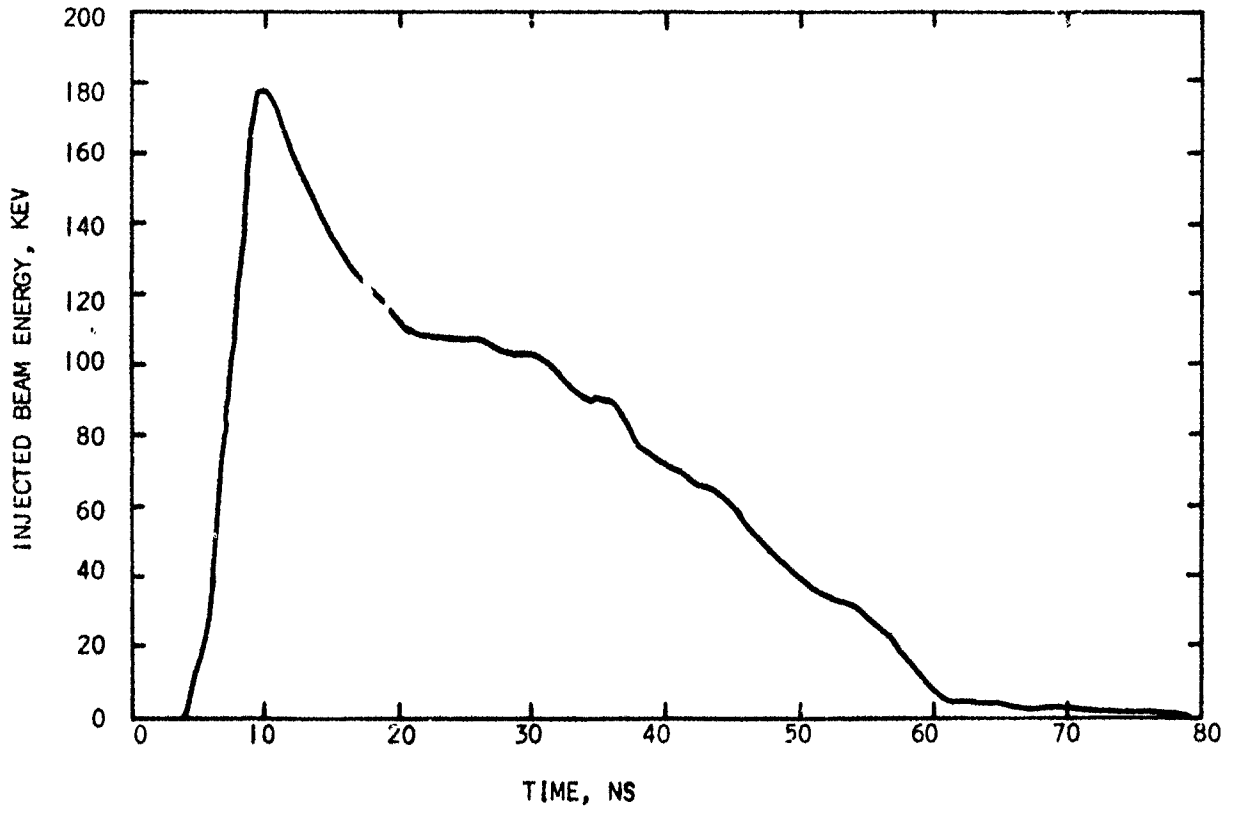


Figure 3.11 Representative Injected Beam Characteristics for IEMP Benchmark Experiments

TABLE 3.3. INJECTED BEAM PARAMETERS - BENCHMARK EXPERIMENT

TIME, NS	INJECTED CURRENT, KAMPS	MEAN ENERGY, KEV	ENERGY BIN #1, KEV	ENERGY BIN #2, KEV	ANGLE BIN #1, DEGREES	ANGLE BIN #2, DEGREES
0	0.0	0.0	0.0	0.0	41.4	75.5
2	0.11	38.1	39.2	36.3	17.0	40.2
4	0.26	122.9	123.3	122.3	4.5	14.3
6	0.45	176.7	177.1	176.2	2.6	9.6
8	0.53	159.4	159.8	158.9	3.0	10.8
10	0.55	144.2	144.6	143.7	3.7	12.0
12	0.61	129.4	129.8	128.8	4.4	13.5
14	0.86	121.7	122.1	121.1	4.6	14.4
16	1.05	111.1	111.5	110.5	5.5	15.7
18	1.18	109.2	109.6	108.5	5.6	16.0
20	1.32	107.7	108.1	107.0	5.7	16.2
22	1.52	107.8	108.2	107.1	5.7	16.2
24	1.74	104.1	104.5	103.4	6.0	16.8
26	1.96	102.6	103.0	101.9	6.2	17.0
28	2.19	96.6	97.0	95.9	6.8	18.0
30	2.43	90.1	90.6	89.3	7.5	19.2
32	2.68	89.7	90.1	88.9	7.6	19.4
34	2.97	76.2	76.7	75.2	9.5	22.4
36	3.26	72.1	72.7	71.2	10.3	23.6
38	3.61	66.5	67.1	65.5	11.1	25.7
40	4.01	63.6	64.2	62.5	11.8	26.9
42	4.52	54.0	54.8	52.7	13.5	31.2
44	4.96	47.0	47.9	45.5	15.0	34.9
46	5.23	39.5	40.5	37.7	16.6	39.4
48	5.38	33.9	35.1	31.9	18.0	42.7
50	5.44	30.9	32.2	28.8	18.9	44.5
52	5.44	24.5	26.0	22.0	21.5	49.3
54	5.40	17.1	18.7	14.4	25.4	55.8
56	5.30	6.5	7.9	4.2	33.8	67.2
58	5.11	5.3	6.5	3.3	34.8	68.6
60	4.81	4.0	5.0	2.3	36.4	70.1
62	4.37	3.0	3.8	1.6	35.0	71.4
64	3.77	3.0	3.8	1.6	35.0	71.4
66	3.08	2.0	2.6	1.0	38.6	72.7
68	2.39	1.6	2.1	0.7	39.2	73.3
70	1.57	1.1	1.4	0.4	39.9	74.0
72	0.89	1.0	1.3	0.4	39.9	74.0
74	0.40	0.5	0.7	0.2	40.7	74.6
76	0.0	0.0	0.0	0.0	41.4	75.5

3.3.6 Injected Current Density

Initially, for long pulse work (i.e. $\tau \approx 100$ ns fwhm) thin film blue cellophane dosimetry could be used⁽³⁾ to determine the time integrated electron current density distribution. Invariably⁽⁴⁾ the measured distribution was quite flat, i.e. $\pm 15\%$ under these conditions. As the technique for producing shorter electron beam pulses evolved, it was no longer possible to use blue cellophane for mapping because the total integrated dose was too low. Uniformity was assumed to hold true there as well.

During an experimental program⁽⁵⁾ employing a 30 ns fwhm pulse, multiple concentric rings used to measure injected current density showed that the beam was annular. Further measurements, made with the Faraday cup array of Figure 3.12 placed 2 mm from the window, agreed with this result as indicated by the total integrated charge values contained in each probe. A cross section of this current density map is presented in Figure 3.13. It shows the current density distribution to be generally hollow with approximately 2.3 times more current in the outer annulus.

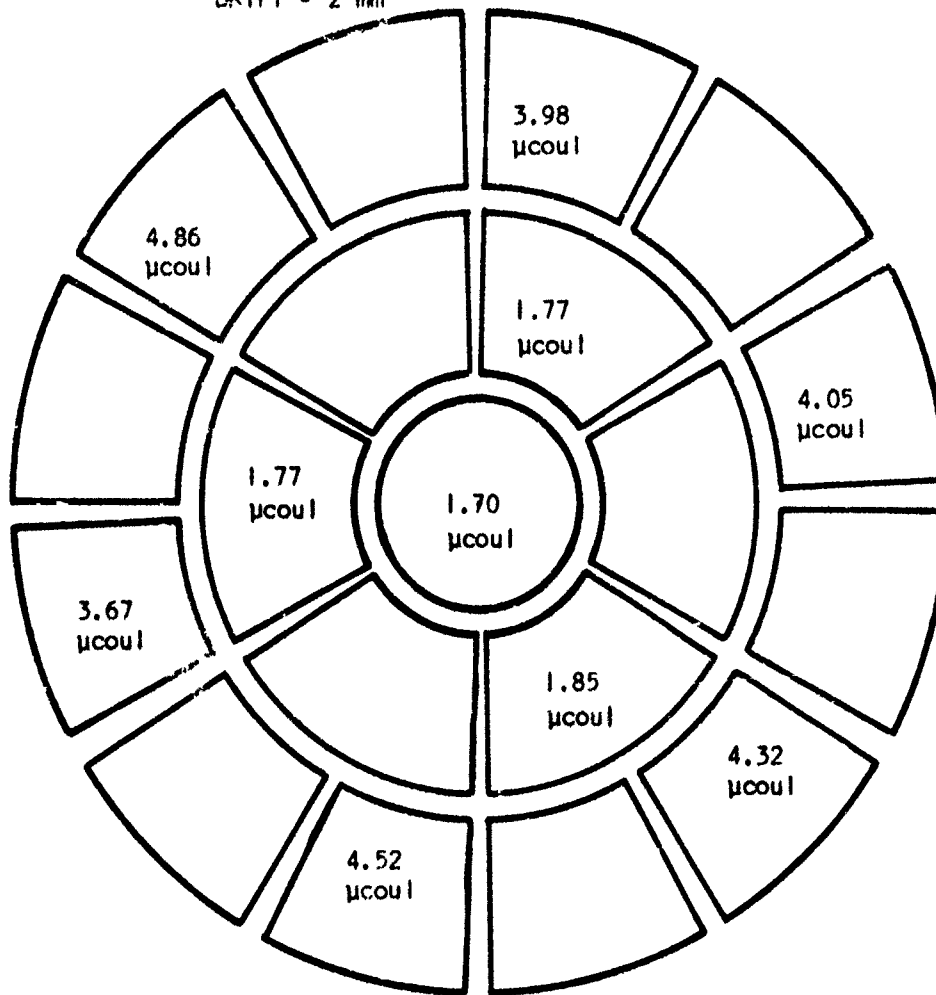
Subsequent to these measurements a radiographic technique was developed for beam mapping. This consists of allowing the electrons to impinge upon a thin, 0.001 inch, tantalum foil over a film cassette thereby creating bremsstrahlung radiation and exposing the film. Although a precise comparison of film exposure and current density has not yet been made, beam uniformity distributions qualitatively agree.

Using this technique a series of measurements was made to determine the cause of the non-uniformity observed and to make corrective modifications. The results were that when a 1/2 inch radius of curvature is used on the 12 inch diameter emitter (reducing the emission surface to 11 inch diameter) uniform emission occurs. Future experiments will be performed with these uniform beams.

19-PROBE SEGMENTED FARADAY CUP

SPI-PULSE 5000 12" DIA. FCH

1.5 cm GAP 250 kv CHARGE $P_d = 40$ mT
DRIFT = 2 mm



PROBE AREA = 36.3 cm^2

Figure 3.12 Segmented Faraday Cup (12" Diameter) Integrated Current Data for 35 ns (fwhm) Pulse

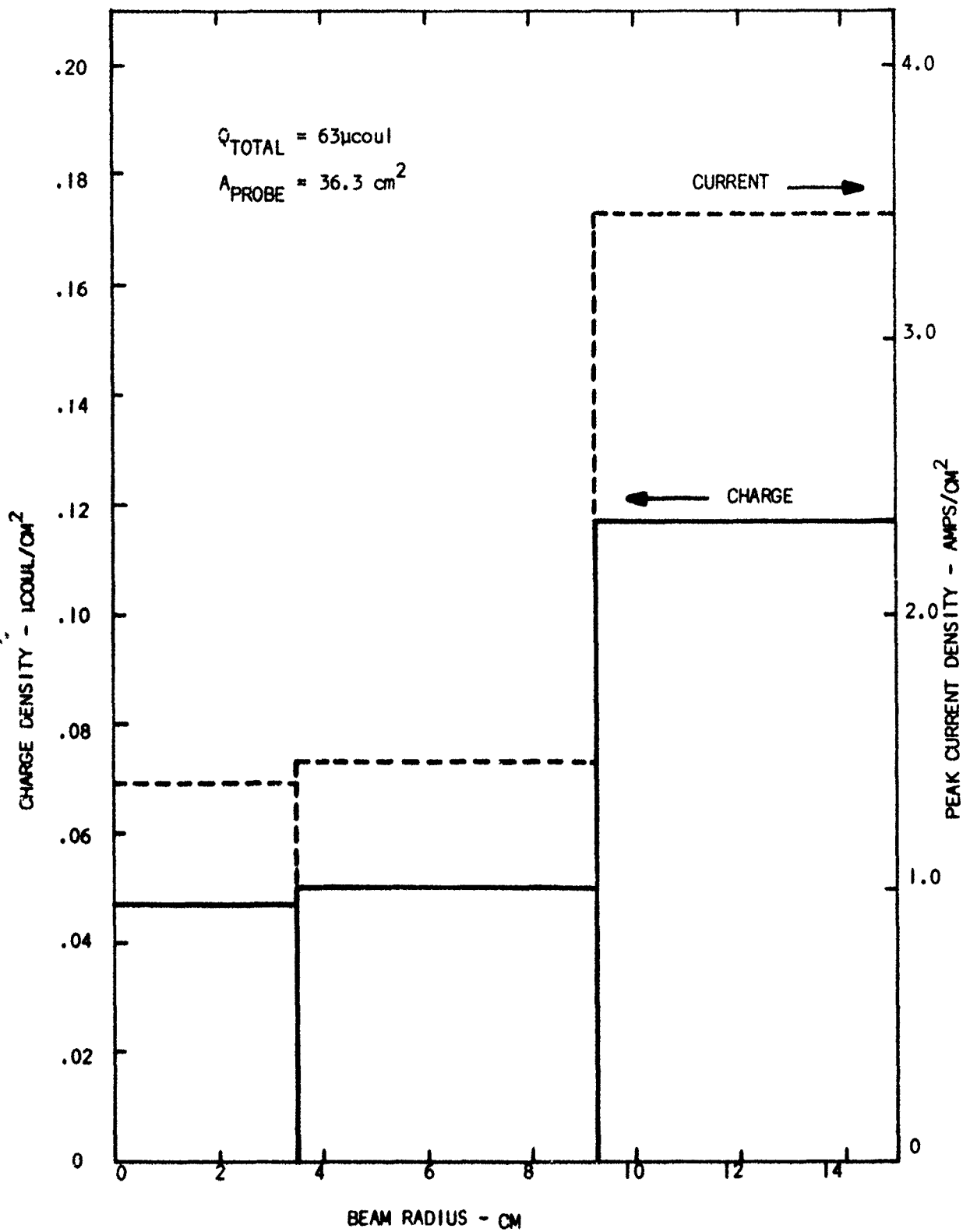


Figure 3.13 Segmented Faraday Cup Charge and Current Density Measurements for 35 ns (fwhm) Pulse

3.4 BENCHMARK EXPERIMENT RESULTS

Throughout the experimental series the cavity pressure was monitored with an Alphatron gauge, estimated to be accurate to better than $\pm 10\%$. At fixed cavity depths, the pressure was scanned from less than 10^{-3} torr to 1 torr. Figure 3.14 is indicative of the general results.

At low pressures the transmitted current falls off rather rapidly with cavity depth. As the pressure is increased above 3×10^{-2} torr, there is an abrupt increase in transmitted current, indicating that space charge neutralization is occurring. The transmitted current peaks at about 0.08 - 0.1 torr, and then falls off gradually up to 0.3 torr. Beyond this it gradually increases.

Figure 3.15 shows the time dependence of transmitted current at three representative pressures. The cavity depth is 15 cm. The main feature is the late time (> 50 ns) tail at .05 and .2 torr. This is presumably due to the formation of a highly conducting plasma, which attempts to maintain a constant magnetic field. Note also that the barrier dissipation time can be estimated as roughly 15 ns into the pulse at 50 microns and 5 ns for 200 microns. At these times there is a marked increase in current compared to the case at 0.1 microns. This indicates that the dissipation time is scaling roughly inversely with pressure, as expected from simply primary ionization arguments.

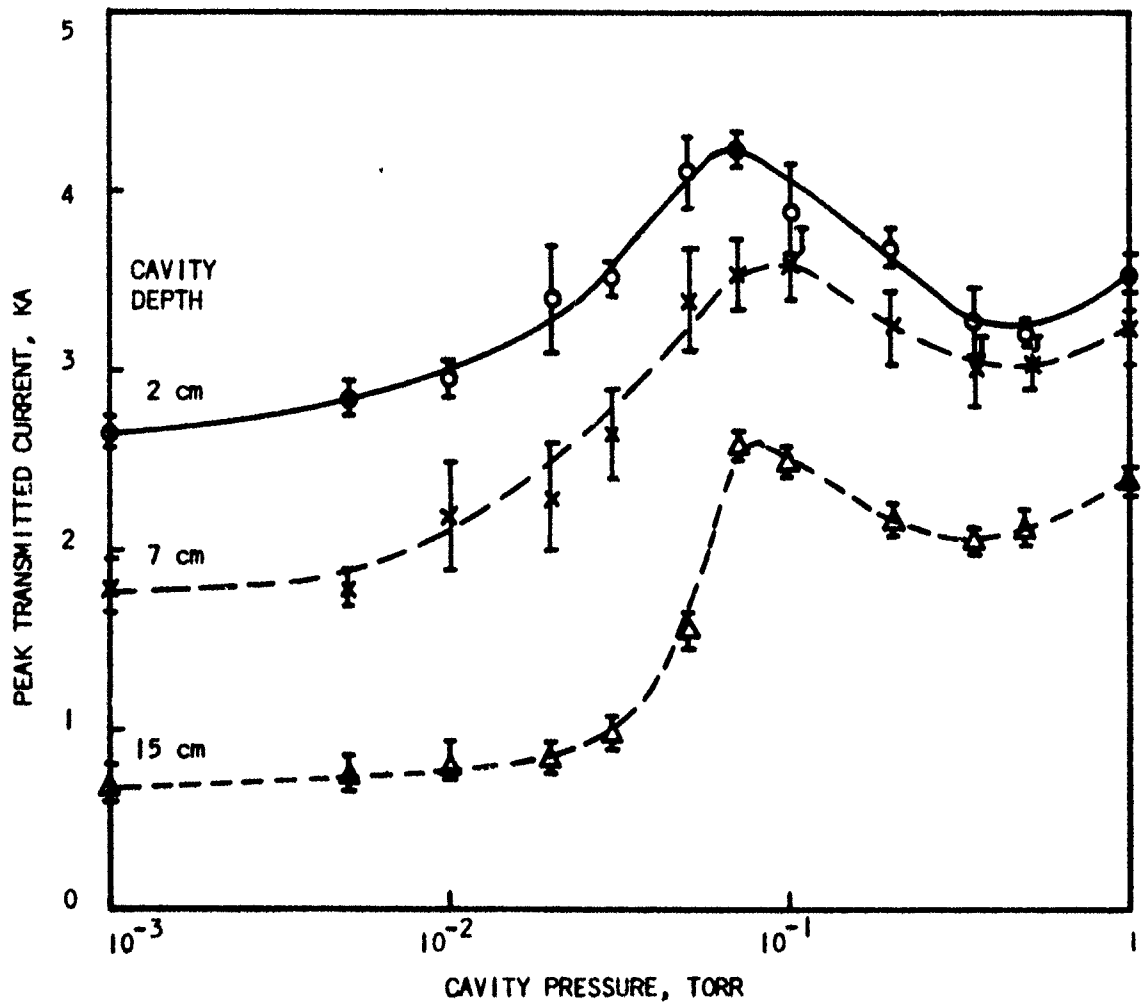


Figure 3.14 Peak Transmitted Current vs. Cavity Pressure for Cavity Depths of 2 cm, 7 cm and 15 cm with 35 ns (fwhm) Pulse in IEMP Benchmark Configuration

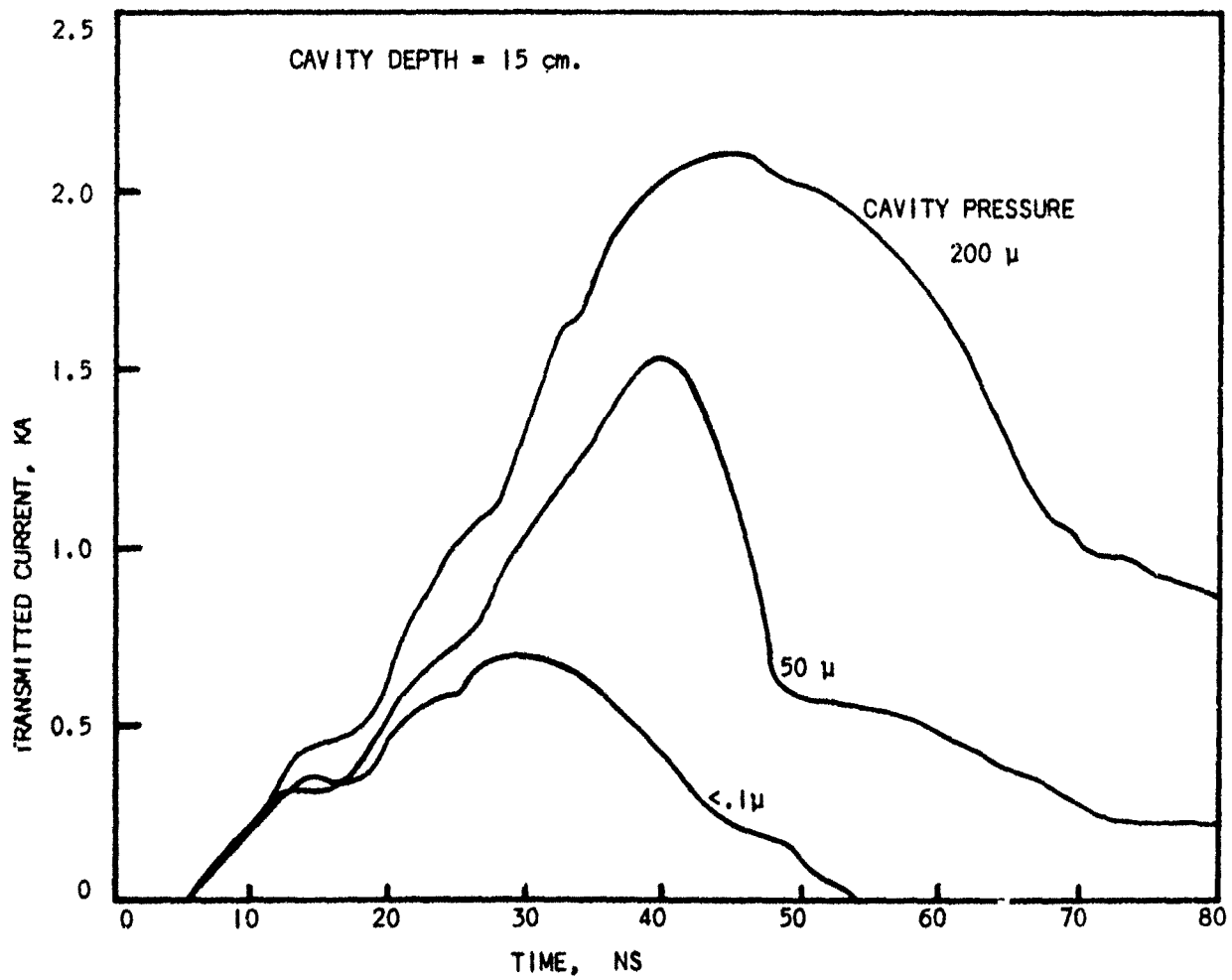


Figure 3.15 Dependence of Transmitted Current Time Signature on Cavity Pressure for 15 cm Deep Cavity and 35 ns (fwhm) Pulse in EMP Benchmark Configuration

SECTION IV DIELECTRIC ENHANCED CAVITY TRANSPORT

4.1 INTRODUCTION

It has previously been shown⁽⁶⁾ that the presence of dielectric surfaces within evacuated (10^{-4} torr) cavities can significantly enhance the transport of electron beams through the cavity. Under situations in which the beam would normally be strongly space charged limited, current enhancement by factors greater than ten has been observed. In this section a review is given of a program which studied the parametric dependence of this effect on dielectric thickness and geometry.

4.2 EXPERIMENTAL CONFIGURATION

In the experimental program the cavity geometry used consisted of a right circular cylinder with the cylinder side wall lined with a thin sheet of dielectric material. Figure 4.1 indicates schematically a typical set-up. The SPI-PULSE 6000 electron beam accelerator was used to inject electrons through one end of the cavity. A high transparency metal mesh served to define a ground plane at the injection end while ensuring that a large fraction of the initial beam entered the cavity. The other end of the cavity was defined by an aluminum plate current collector which was electrically connected to the cavity side wall through a low impedance (~ 0.02 ohm) resistive shunt. The voltage induced across this shunt (less than 300 volts) was monitored to provide a measurement of the current transmitted through the cavity.

Another resistive shunt, located near the injection plane, electrically connects the cavity side wall to the electron injection source ground. This monitor was used to measure the sum of the injected current striking the side wall plus the current transmitted to the back of the cavity. When the side wall was lined with dielectric this monitor indicated the current striking the dielectric plus transmitted current; the current striking the dielectric and becoming trapped in it is capacitively coupled to the cavity side wall and the induced current flowing through this capacitive link is equal in magnitude to that striking the dielectric.

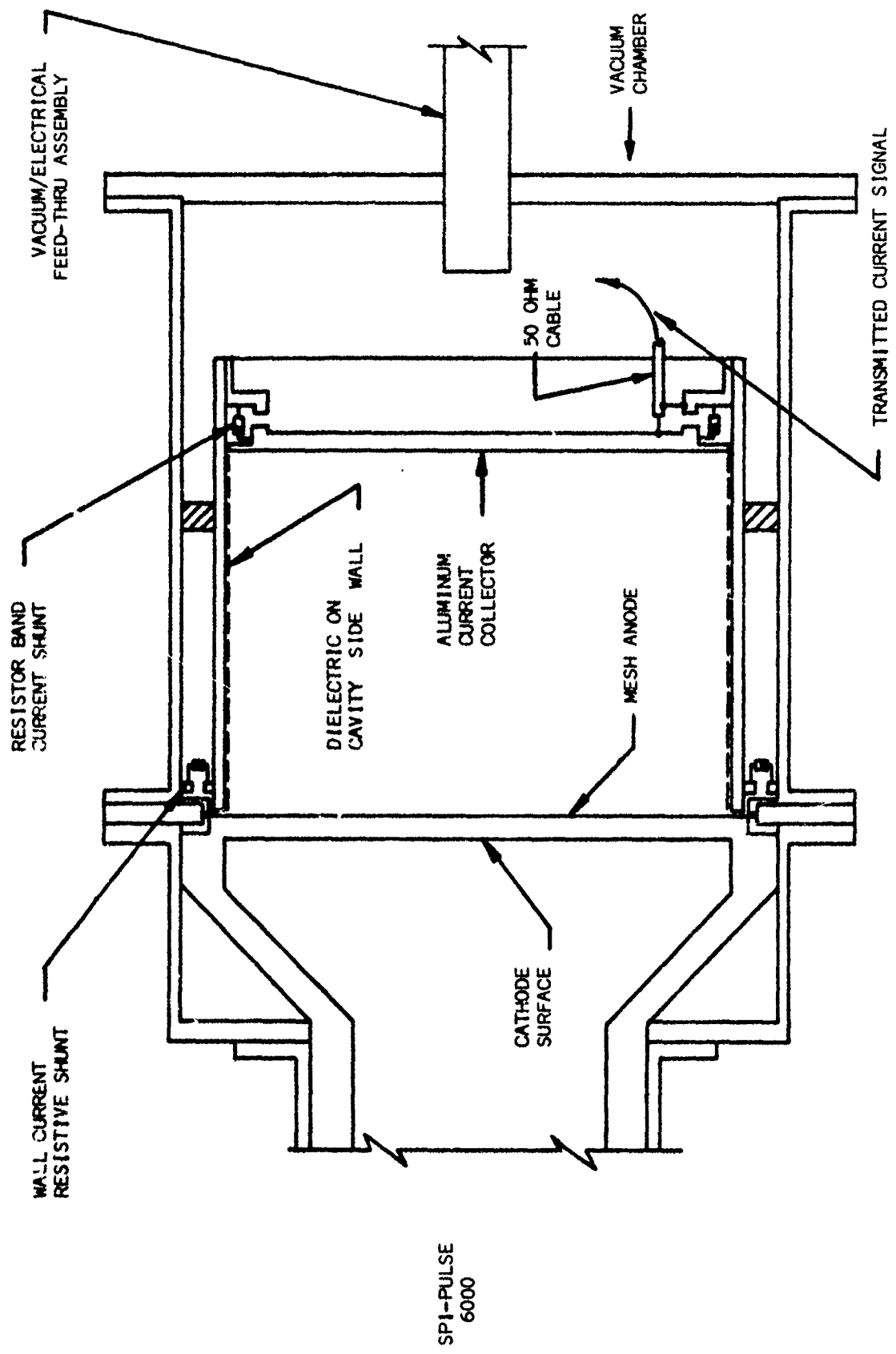


Figure 4.1 Apparatus for Dielectrically Lined Cavity Wall Experiments

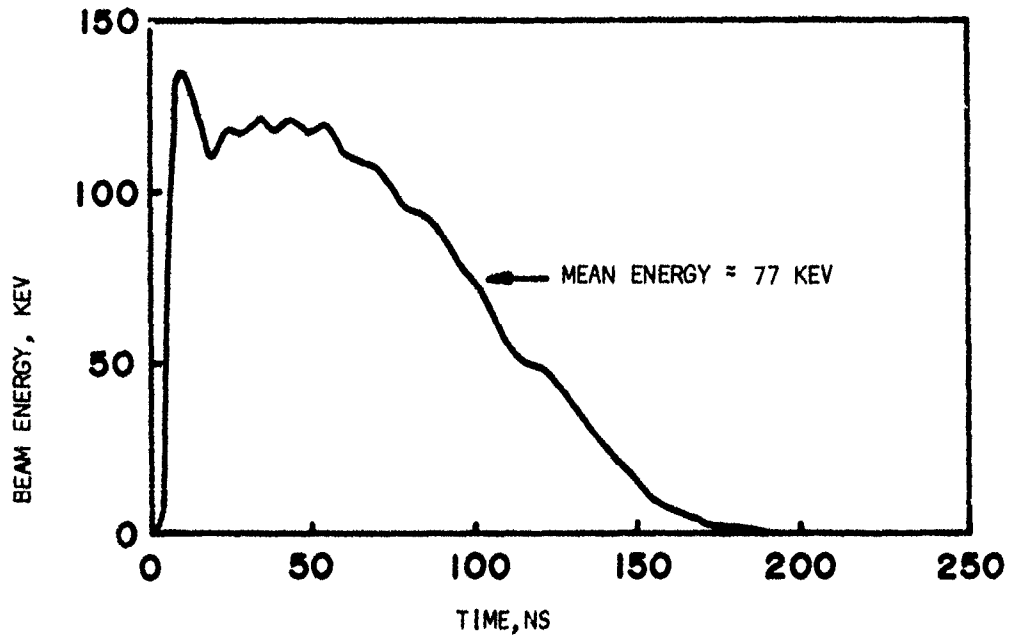
The cavity was housed within a vacuum chamber which was evacuated to less than 10^{-3} torr pressure in all cases. Previous experimental work⁽⁷⁾ in this pressure regime has shown that no enhanced current transport occurs due to space charge neutralization by ionization of the ambient gas. The current enhancement that is observed is therefore attributable to the presence of dielectric material within the cavity.

4.3 CONSTANT CURRENT EXPERIMENTS

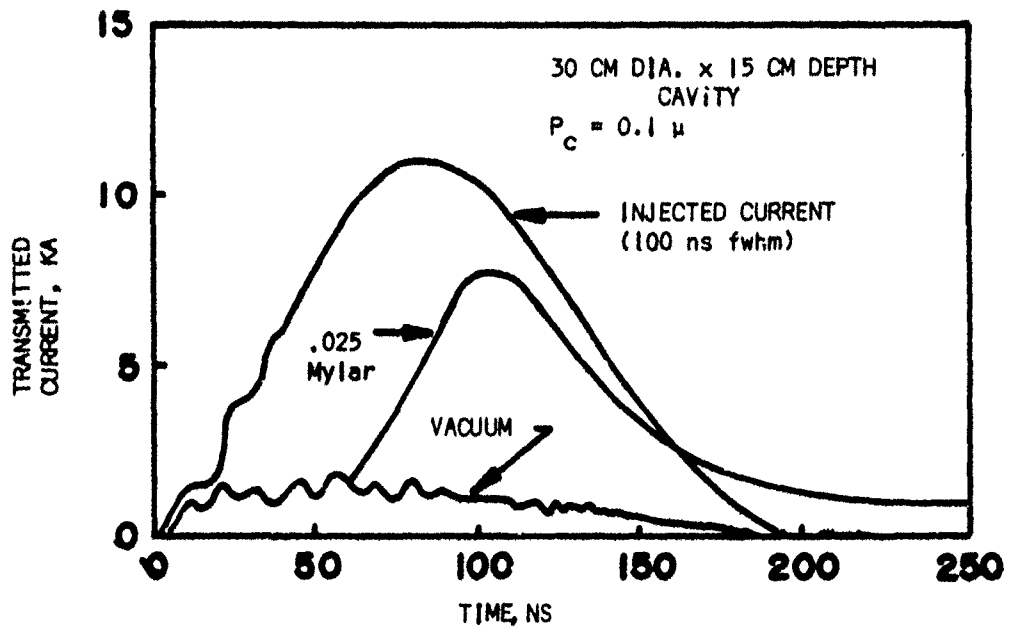
In this set of experiments three different cavity diameters (10, 15, and 30 cm) were used. In conjunction with a range of cavity depths, the cavity diameter to depth aspect ratio was varied from approximately 0.7 to 2.0. For each aspect ratio the dielectric thickness was varied to determine the dependence of current enhancement on this parameter. For each cavity diameter, the SPI-PULSE 6000 electron beam forming diode was modified to keep both the mean injected electron energy and peak injected current approximately constant. In all cases the injected beam diameter was equal to or slightly smaller than the inner cavity diameter.

Figure 4.2 shows a representative set of data obtained for a 30 cm diameter by 15 cm deep cavity. The upper graph gives the time dependence of the injected electron energy. Since the thickness of the mesh material used at the injection plane was much greater than an electron range the injected beam was essentially mono-energetic at any instant of time. The lower graph is composed of three waveforms. The upper curve shows the current that would be transported across the cavity if there were no space charge limiting or beam blow up. It was obtained by positioning the back plate current collector one millimeter behind the mesh anode. The lower curve indicates the measured transmitted current for an evacuated cavity with no dielectric present. The intermediate curve is obtained when 0.025" of Mylar dielectric is placed on the cavity side wall. Several features are apparent:

- 1) With no dielectric present there is heavy space charge limiting and only a small fraction of the injected current is transmitted. As shown in Figure 4.3, the



(A) Time Dependence of Injected Beam Energy



(B) Injected and Transmitted Current Profiles

Figure 4.2 Diode Voltage, Injected Current Pulse and Comparative Transmitted Current Traces with and without Dielectric Wall at Low Pressure

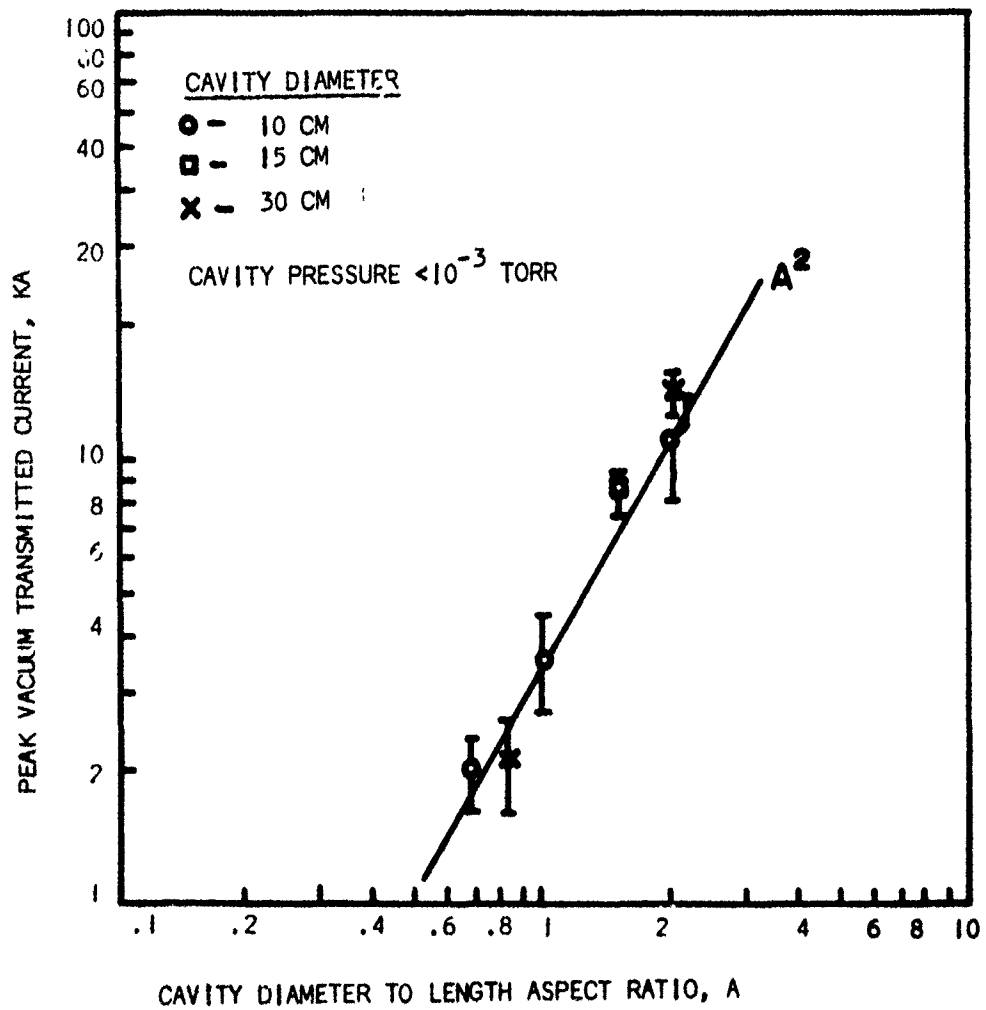


Figure 4.3 Peak Vacuum Transmitted Current Dependence Upon Cavity Aspect Ratio

amount transmitted scales as the square of the cavity aspect ratio over a large range of cavity diameters and cavity lengths.

- 2) With dielectric present, there is a delay period to the onset of current enhancement. During this delay the transmitted current stays at the same level as observed in the no dielectric case. As shown in Figure 4.4, the duration of this delay scales linearly with cavity length.
- 3) Following the onset of enhanced transport the transmitted current climbs to a value which is a large fraction of the injected current.
- 4) Late in time the transmitted current shows a long tail, even after the corresponding injected current pulse has gone to zero. This is reminiscent of induced plasma currents observed in gas neutralization experiments⁽⁸⁾.

Figure 4.5 shows the measured dependence of peak enhanced current on dielectric thickness. It should be kept in mind that in these measurements the total injected current was held constant. The upper graph shows results for two different cavity diameters with a fixed depth of 15 cm. For no dielectric or very thin dielectric, the peak transmitted current increases with increasing aspect ratio. However, for thicknesses greater than 0.005" of Mylar there is no significant difference. The lower graph shows similar results for two other cavity diameters and a different cavity depth. For the early portion of the injected beam pulse the beam energy is roughly constant at 110 keV; the arrow on the upper graph indicates the extrapolated range for this electron energy in Mylar. If the data for 0.005" and thicker is plotted on a log-log scale, the dependence of peak transmitted current on thickness is to the 1/4th to 1/5th power.

Corroborating evidence for the delay to onset of enhanced transport was also seen in the wall current signal. Figure 4.6 shows data obtained for a 15 cm diameter by 10 cm deep cavity. Again the curve marked injected current, measured

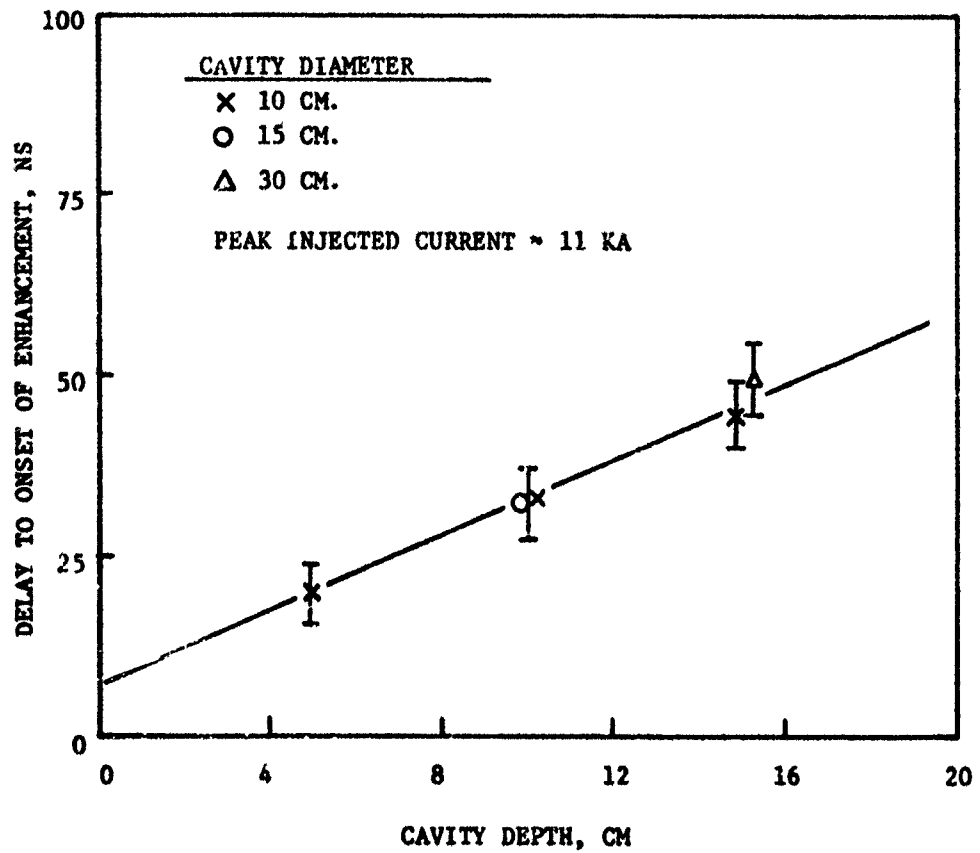


Figure 4.4 Dependence of Time Delay To Onset of Current Enhancement on Cavity Depth - Constant Injected Current

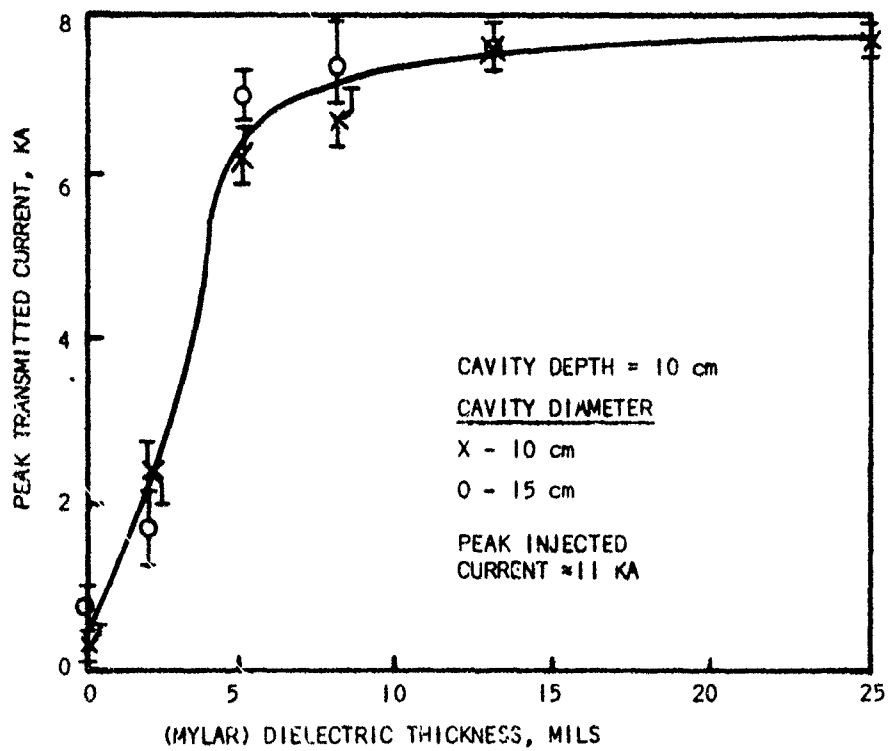
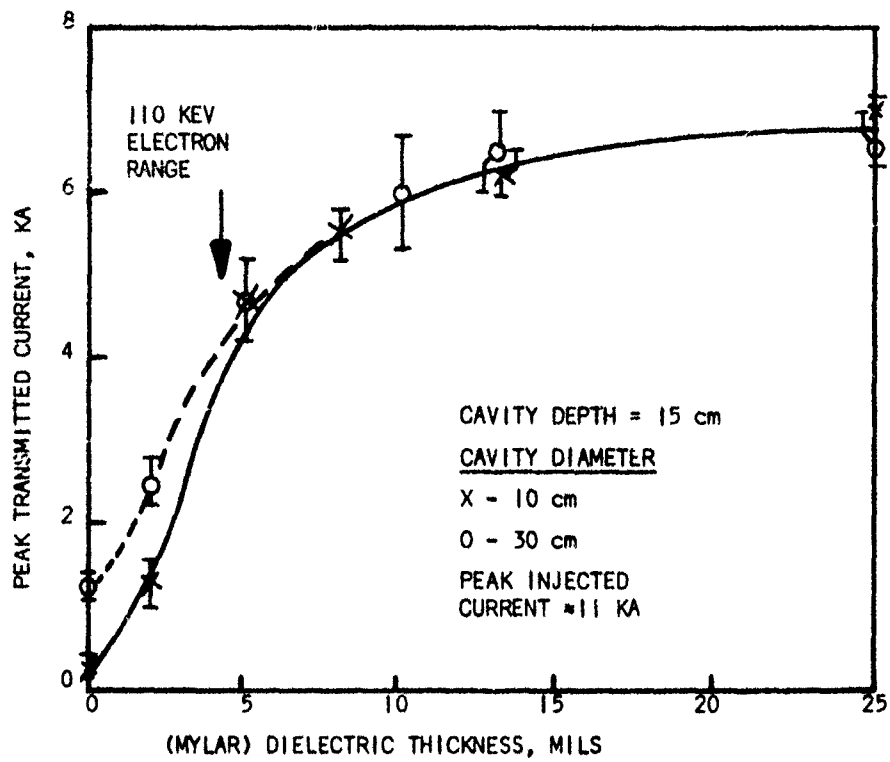


Figure 4.5 Peak Transmitted Current Dependence on Dielectric Thickness

15 CM DIA X 10 CM DEEP CAVITY

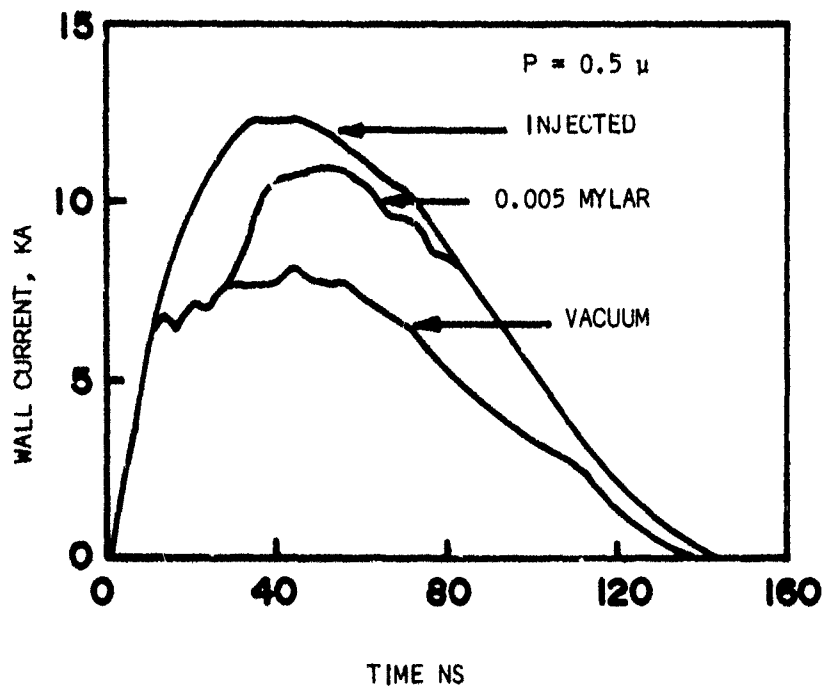


Figure 4.6 Wall Current Measurements for 15 cm Diameter 10 cm Deep Cavity

1 mm beyond the injection plane, is what would be seen if there were no space charge limiting. The lower curve indicates the vacuum cavity situation. Since less than 1.0 kamp of current is transmitted through the cavity, this curve indicates the current striking the side wall. Roughly one-third of the injected current is returned to the injection plane. With dielectric present there is again a delay to onset of enhanced current, equal to the delay observed in the transmitted current pulse, and then an abrupt rise in wall current due to transmitted current enhancement. Similar results were seen in the 10 cm and 30 cm diameter cavity experiments.

Finally, measurements were carried out to assess what influence the type of dielectric material might have on current enhancement. Figure 4.7 shows data obtained for Mylar, polyethylene, and polyvinylchloride (PVC). There did not appear to be significant differences in the delay to onset of enhancement, but there were differences in the rate of current rise (di/dt) to peak enhanced current.

4.4 CONSTANT CURRENT DENSITY EXPERIMENTS

In this series of experiments the injected current density was held constant; three different cavity diameters (10 cm, 15 cm, 30 cm) were used with a fixed cavity depth of 15 cm. Figure 4.8 is indicative of the results obtained. The upper graph shows results for a 30 cm diameter cavity, while the lower graph is for a 15 cm diameter cavity. In both cases the onset of enhanced current occurs at approximately 50 ns into the pulse. The total charge injected through the entrance plane was $0.4 \pm 0.05 \mu\text{C}/\text{cm}^2$.

4.5 PULSE WIDTH VARIATION EXPERIMENTS

Another set of experiments kept the cavity/dielectric geometry constant, and varied the time duration of the injected pulse. Figure 4.9 shows the general behavior observed as the pulse width decreases; the upper graph shows strong enhancement for an injected pulse width of 82 ns (fwhm). The intermediate graph is for a pulse width of 75 ns (fwhm) and shows a moderate amount of enhancement. The lower graph shows a small enhancement with a 63 ns (fwhm) pulse. In all cases the beginning of increased current transport occurred at 50 ns.

30 CM. DIAMETER X 15 CM. DEEP CAVITY

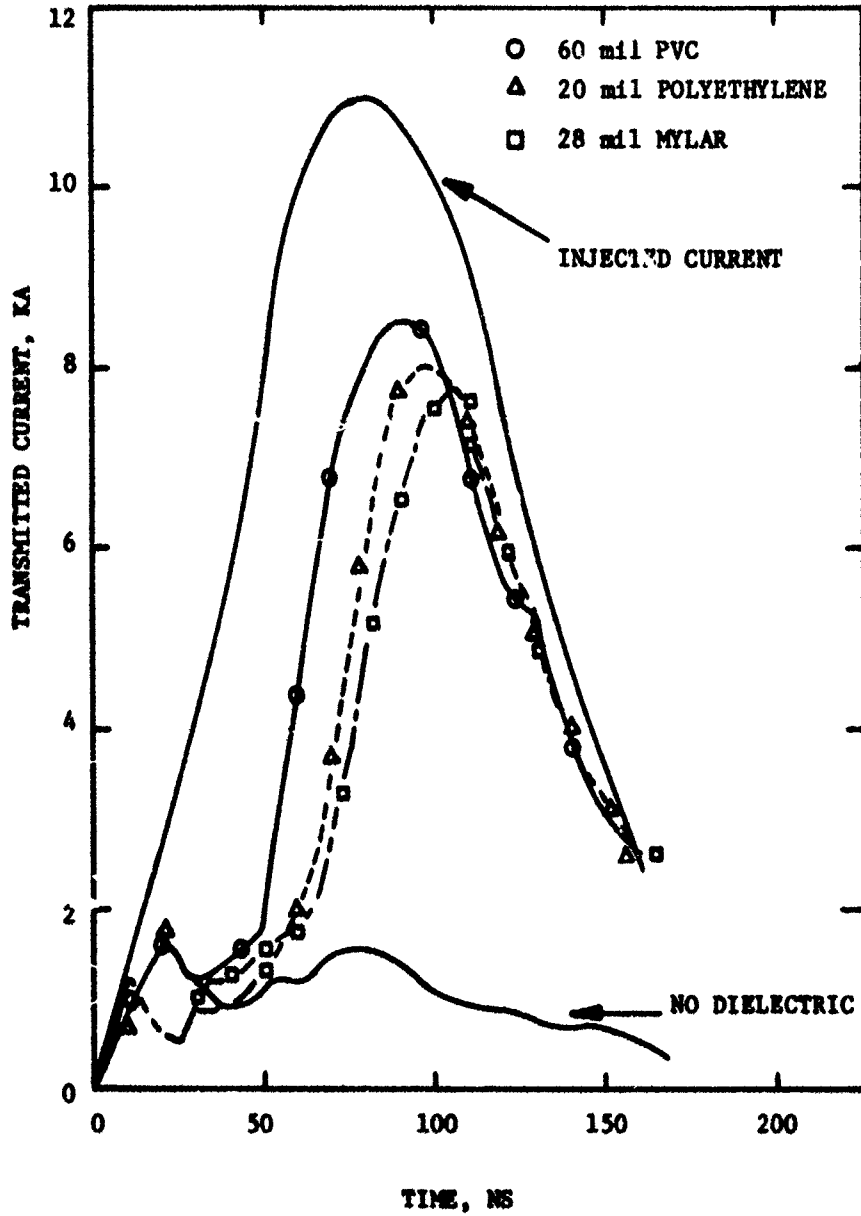


Figure 4.7 Dependence of Transmitted Current on Dielectric Material

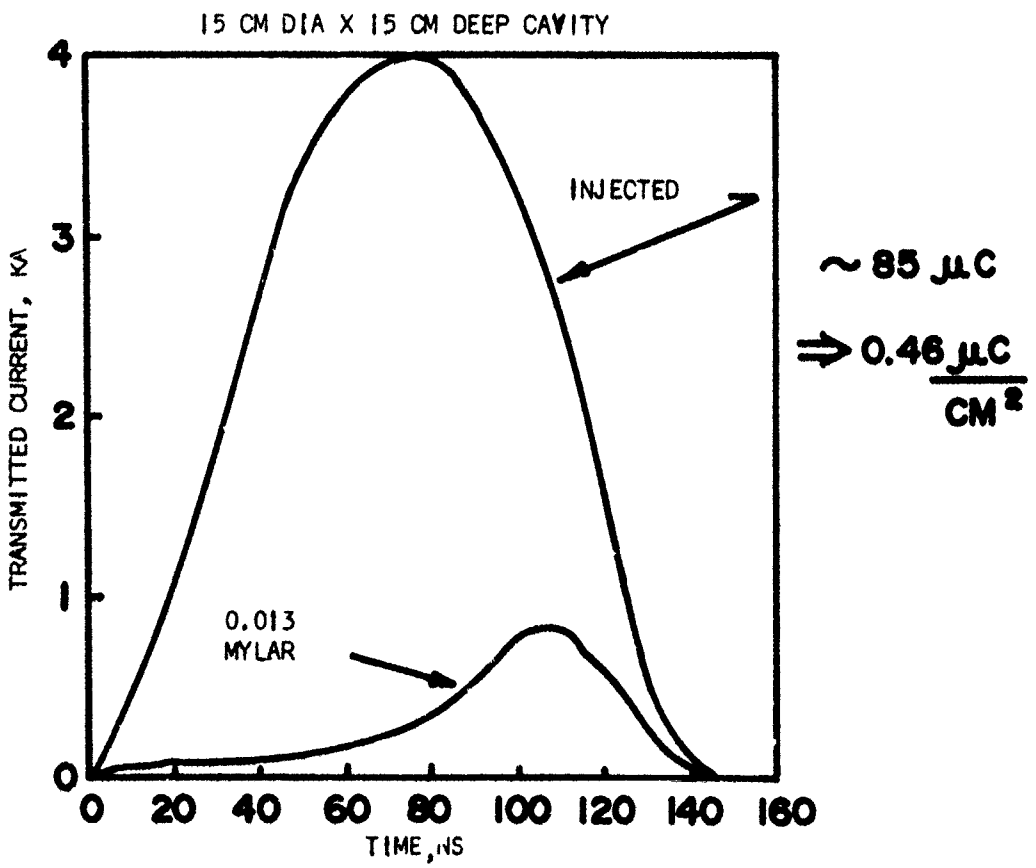
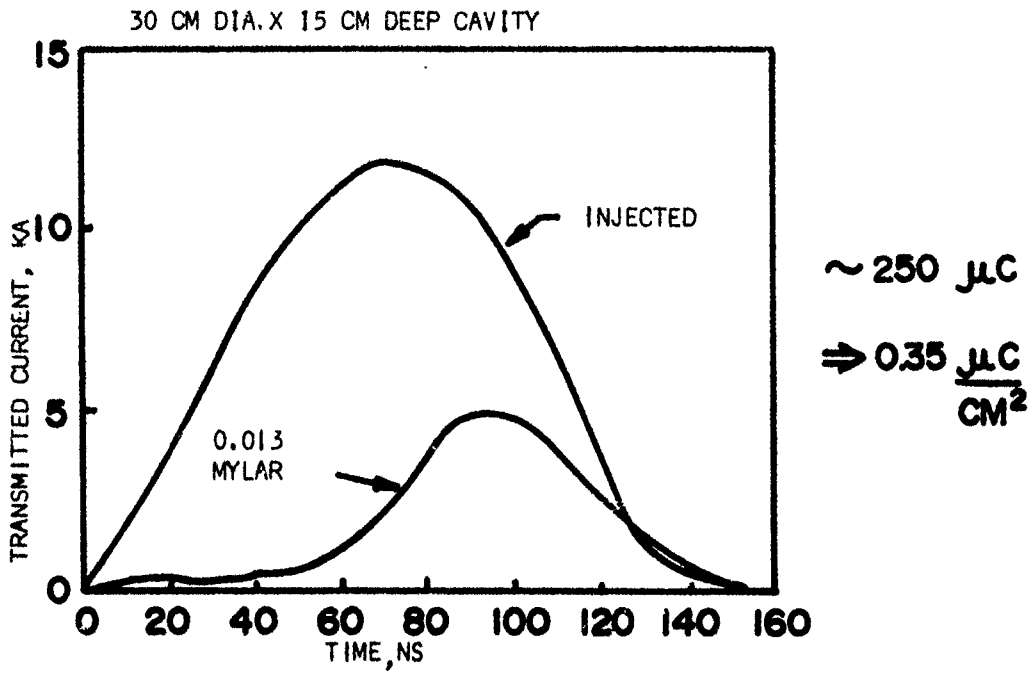


Figure 4.8 Representative Results for Constant Current Density Experiments

Q DEPENDENCE

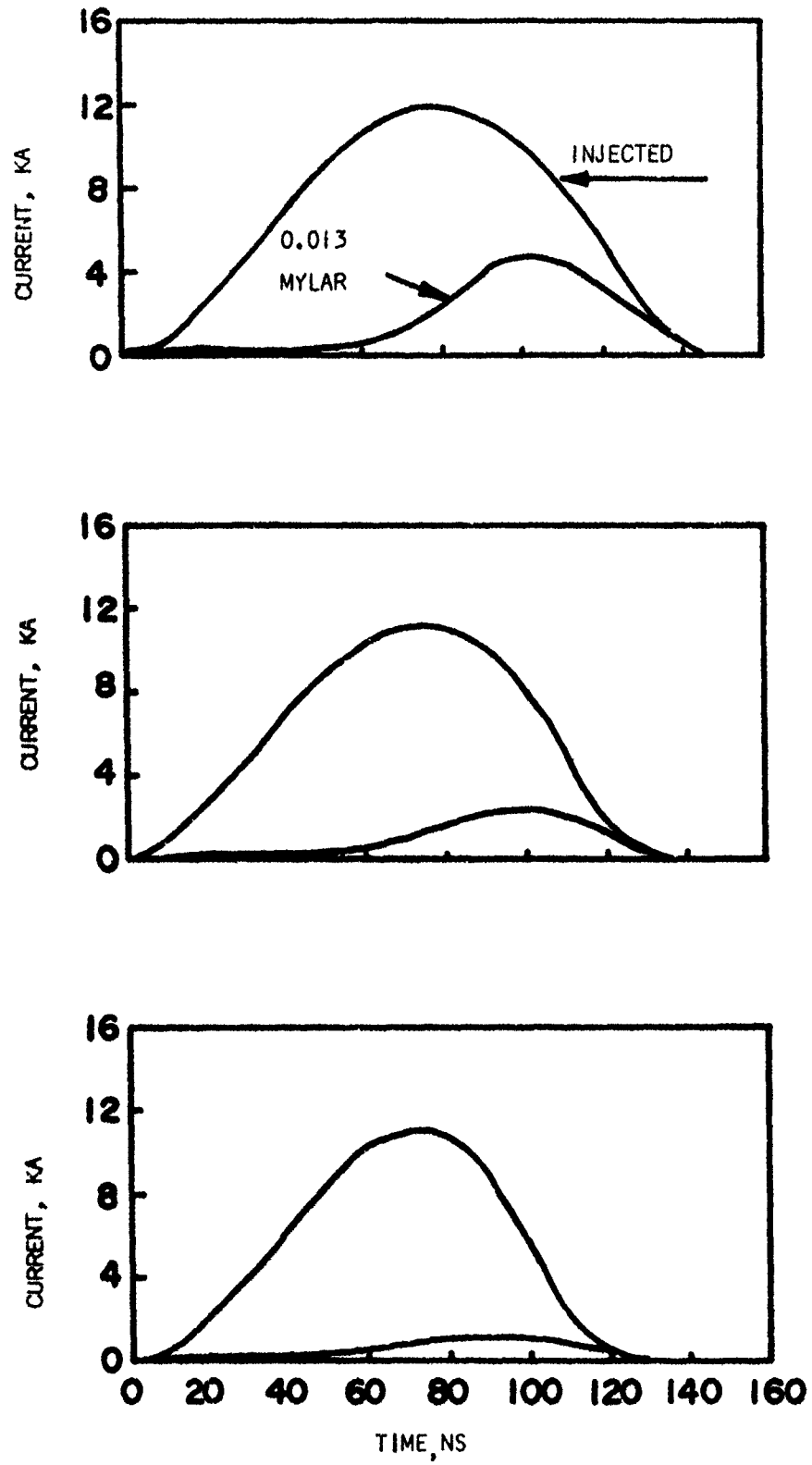


Figure 4.9 Effect of Injected Current Pulsewidth Variation Upon Transmitted Current Pulse

4.6 ION DETECTION EXPERIMENTS

Because the injected beam is heavily space charge limited, the most obvious explanation of the observed enhanced transport is that barrier dissipation, that is, space charge neutralization, occurs. This is accomplished by positive ions. As noted earlier, the long tail observed on the transmitted current pulse is reminiscent of induced plasma currents. Experiments were carried out to detect the presence of ions.

The side wall of a 10 cm diameter by 15 cm deep cavity was lined with a thick (~5 mm) tube of Lucite. An apertured plate terminated the cavity, the aperture being 3 cm in diameter. A permanent magnet was positioned behind the aperture to sweep out both primary and secondary electrons. The magnetic field (~300 gauss) was low enough to produce minimal deflection of any ion greater than 10 Kev energy. Detection of positive charge flow was done with a 2 cm diameter charge collector which was connected to a 50 ohm cable.

Late time (> 300 ns) positive charge flow was detected; by moving the charge collector further away from the magnet a time of flight determination of the velocity of the positive ions could be made. The result was $\sim 10^8$ cm/sec. The amplitude of the detected current scaled as the inverse square of the detector distance from the aperture. The extrapolated positive ion current density at the back of the cavity is about 0.5 A/cm^2 ; the pulse duration is $\sim 1 \text{ } \mu\text{sec}$ (fwhm). Since the presence of the magnetic field prevented lower energy ions from being detected it is certainly possible that the actual current density was higher.

From the above measurements an estimate can be made of the ion density in the cavity. Since

$$n = \frac{I}{ev}$$

then the ion density was at least $3 \times 10^{10}/\text{cm}^3$. This is low compared to the primary electron beam density of $\sim 10^{12}/\text{cm}^3$. Assuming that the magnitude ($\sim 500 \text{ A}$)

of the late time tail on the transmitted current pulse is more representative of the real current density (including lower energy components), then in fact the ion density works out to be $\sim 10^{12}/\text{cm}^3$.

At the ambient chamber pressure used (10^{-4} torr), ionization of the background gas by primary beam electrons could only produce about $10^9/\text{cm}^3$ of ion density. Thus the ions detected are most probably associated with the presence of dielectric on the cavity wall.

In some instances it was observed that puncture of the dielectric had occurred, presumably by electrical breakdown in volume. However it was not observed in all cases. Surface flashover is another electrical failure mode of dielectrics. To determine whether this was occurring, open shutter photographs were made with the camera focused on the portion of the dielectric near the injection end. Figure 4.10 shows a photograph obtained using neutral density filtering to reduce the light intensity. It is clear that a great deal of flashover is occurring, fairly symmetrically, near the injection end of the cavity. Since the light emitted by flashover is due to radiation from a hot, ionized gas - equivalent to the light emission from an electrical spark - it is evident that this is a likely candidate for explaining the origin of the observed ions.

4.7 INTERPRETATION

From the experimental data it is possible to construct a model of what is happening within the cavity. The beam is initially heavily space charge limited, and most of the current strikes the side wall of the cavity. The charge is trapped in a surface layer of the dielectric; the induced transient conductivity⁽⁹⁾ is too low to allow the charge build-up to leak off. The accumulated charge therefore generates a strong electric field; near the injection plane this field will have a large component along the surface of the dielectric. This is due to both the presence of the injection plane ground and non-uniformity in surface charge density. Martin⁽¹⁰⁾ has empirically developed a formula for predicting the time required to initiate flashover; a stress of 200 kV/cm is sufficient to cause breakdown in 10 ns. It thus seems likely that early in the injected pulse

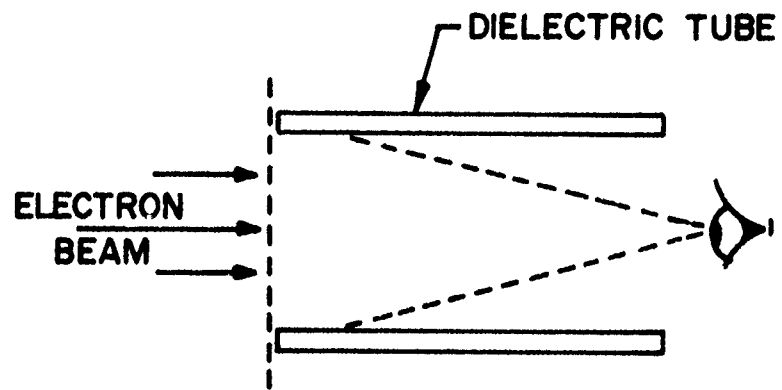


Figure 4.10 Open Shutter Photograph of Surface Flashover on Dielectric Tube

flashover occurs and either a thin surface layer of the dielectric is sublimated, or adsorbed gas is released and ionized⁽¹¹⁾. These ions are then accelerated into the body of the beam by space charge electric fields.

Figure 4.4 indicates that, even if the cavity is very short, approximately 10 ns is required to see enhanced transport. Assuming that the ions are generated essentially instantaneously, this would correspond to the time it takes for ions to neutralize a significant portion of the beam. Near the cavity side wall the radial electric fields are of order

$$E \sim \frac{V_B}{R}$$

where

V_B = beam voltage (kinetic energy in volts)
 R = cavity radius

Then:

$$\Delta R \approx \frac{1}{2} \frac{V_B}{\frac{mc^2}{q}} \frac{c^2 t^2}{R}$$

is the extent of the ions radial motion during the time period, t . Here

$$\begin{aligned} \frac{mc^2}{q} &= \text{ion rest mass per charge state} \\ &= 10^9 \text{ volts} \end{aligned}$$

Using $t = 10$ nsec, one obtains for $V_B = 10^5$ volts

$$\Delta R \approx 1 \text{ cm}$$

Thus, in the first 10 ns of the pulse the outer portion of the beam can become charge neutral; since there is local barrier dissipation that portion of the

beam can propagate further down the cavity, strike the dielectric, and cause further flashover. Ions from the first region will continue to charge neutralize more of the injected beam and allow more current to flow further into the cavity. The net current flowing to the wall would not necessarily increase; only the distance into the cavity it propagates changes.

Again from Figure 4.4 it can be inferred that the rate at which the current front propagates down the cavity is about 3×10^8 cm/sec. Once the end of the cavity is reached, further enhancement ensues as the ions neutralize more of the beam. If the pulse duration is long enough, almost all of the injected current is ultimately transported. Based on the constant current density experiments it can be concluded that $0.4 \mu\text{C}/\text{cm}^2$ of injected charge is an upper limit on the amount of charge required to initiate enhanced transport for the beam parameters and cavities studied.

4.8 CONCLUSIONS

It is apparent that even very thin layers of dielectric can have a significant influence on current transport through evacuated cavities. For short (~ 20 ns) pulse situations, current densities less than $40 \text{ A}/\text{cm}^2$ are sufficient to cause enhanced current flow. Although the effect will not propagate an appreciable distance beyond the injection plane, it will nevertheless significantly modify both the amplitude and the spatial extent of the electric and magnetic fields near the injection plane. As an example, rates of rise of current of 5×10^{11} A/sec have been observed; within a 30 cm diameter cavity the corresponding rate of rise of magnetic field is 3×10^{10} gauss/sec. Inductive electric fields can be significant and can drive large skin currents in neighboring structures.

SECTION V
SPI-PULSE 6000 MODIFICATION

5.1 INTRODUCTION

A redesign of the SPI-PULSE 6000 was carried out to achieve faster current risetime and low jitter switching for synchronously firing several machines in parallel. Specifically, multichannel triggering with a lower inductance front end design was attempted. This section describes these modifications and the results.

5.2 RISE TIME CONSIDERATIONS

5.2.1 Machine Design Modifications

In order to improve the current risetime of the machine it was necessary to reduce the front end inductance. This inductance is made up of two components: a fixed inductance associated with the geometry and switch inductance. A complete redesign of the SPI-PULSE 6000 output section was therefore performed. A reduction in all stray inductance components, not just that associated with the output switch, was necessary. We review here the modifications made.

Figure 5.1 shows schematically the new front end configuration. Major changes consist of:

- shortening of the solid dielectric energy store flashover length to 7 inches. It was demonstrated experimentally that charging voltage in excess of 400 kV can be achieved with this shorter length.
- use of parallel plate switching domes with a 0.75 inch spacing. With 30 psig Freon as insulator, this gap can support 400 kV d.c. charging voltage.
- an increase in the diameter of the switch housing and output tube, as well as shortening of the housing and tube length.
- increase in the cathode shank diameter and shortening of its length.

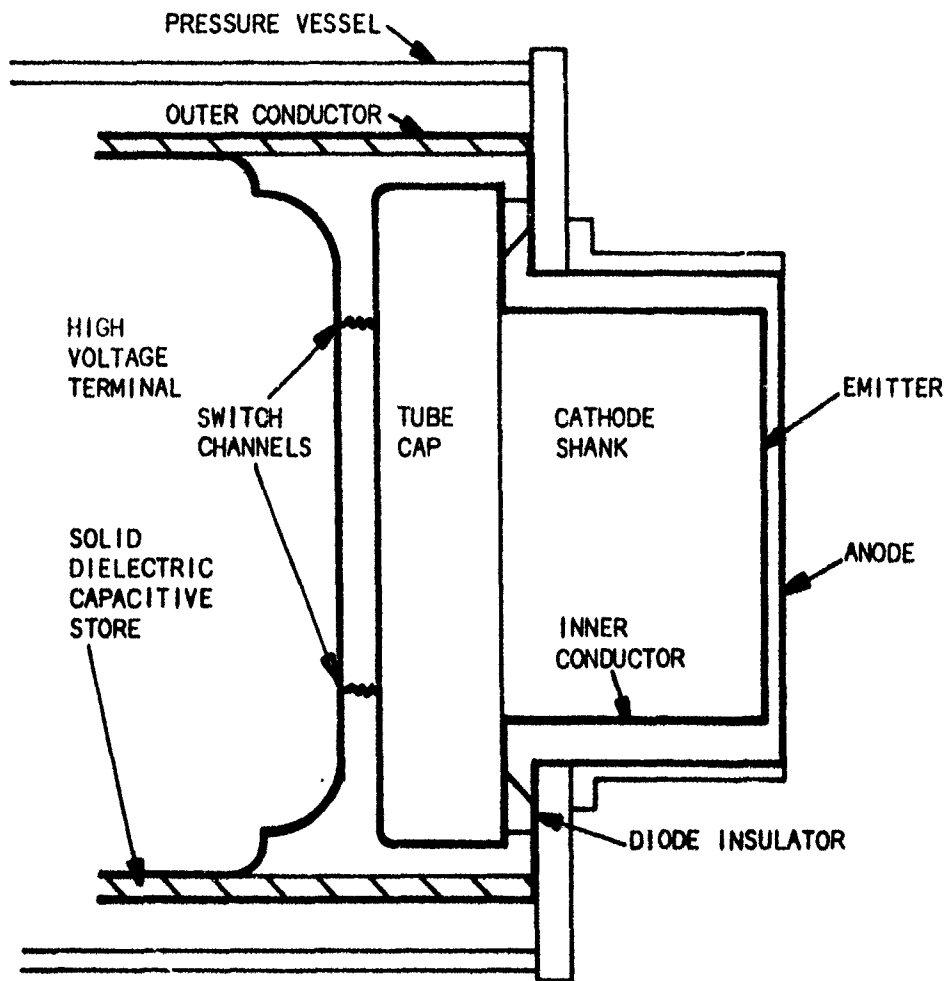


Figure 5.1 SPI-PULSE 6000 Redesigned Low Inductance Front-end Showing Inner and Outer Conducting Paths

5.2.2 Risetime Analysis

For design purposes, the output risetime can be computed as the algebraic sum of the resistive phase time constant and the inductive phase risetime.

Martin⁽¹³⁾ has shown that the resistive phase can be calculated from the formula

$$T_R = \frac{88}{Z^{1/3} E^{4/3}} \left(\frac{\rho}{\rho_0} \right)^{1/2} \quad (\text{ns})$$

where

E = average gap stress in units of MV/meter

Z = impedance of source supplying energy to the trigger channel, in ohms.

ρ = density of gas used as switching media.

ρ_0 = density of air at NTP

For a single channel switch, the source impedance Z is equal to the energy store impedance Z_0 (equal to 2 ohms for the SPI-PULSE 6000). For multi-channel switching with n channels, only one- n^{th} of the store can feed an individual channel. Thus, Z must be equal to nZ_0 . With the new front end design, we have the following parameters:

$$E \leq 20 \text{ MV/m}$$

$$Z_0 = 2 \text{ ohms}$$

$$\frac{\rho}{\rho_0} = 13$$

which gives

$$T_R \geq \frac{4.64}{n^{1/3}} \text{ nsec}$$

The inductive phase risetime is given by:

$$T_L = 2.2 \frac{L}{Z_0 + R_L}$$

where

L = total stray inductance

Z_o = energy store impedance

R_L = load resistance

Assume a matched-load case, $R_L = Z_o$. The inductance is composed of two components; the fixed inductance associated with the switch housing, output tube, and cathode shank plus the inductance of an n -channel output switch. For the new design, the fixed inductance is calculated to be 13.85 nH. The multi-channel switch inductance is given by the formula

$$L = \left\{ 2 \ln \frac{r_o}{r_i} + \frac{1}{n} \ln \frac{r_i}{n \Delta r} + \frac{1}{4n} \right\} l$$

where

l = switch gap length = 2 cm

r_o = ground return radius = 26.675 cm

r_i = radius of switching circle = 12.7 cm

Δr = spark channel radius \approx 0.05 cm

Combining all of these factors, the output risetime is given by the relation

$$T_{\text{rise}} = T_R + T_L \geq 9.25 + \frac{4.64}{n^{1/3}} + \frac{1.1}{n} \left(0.25 + \ln \frac{254}{n} \right)$$

The computed values are shown graphically in Figure 5.2. It is evident that at least 4 channels are required to achieve the desired risetime performance. We, in fact, decided to employ six channels to insure that at least four will have good current sharing and produce a fast rise.

5.2.3 Effect of Non-Linear Diode

In practice, the diode risetime will be slightly different than that computed above because the diode is a non-linear load. Assuming an ideal Child-Langmuir behavior, the diode voltage is related to the current flowing

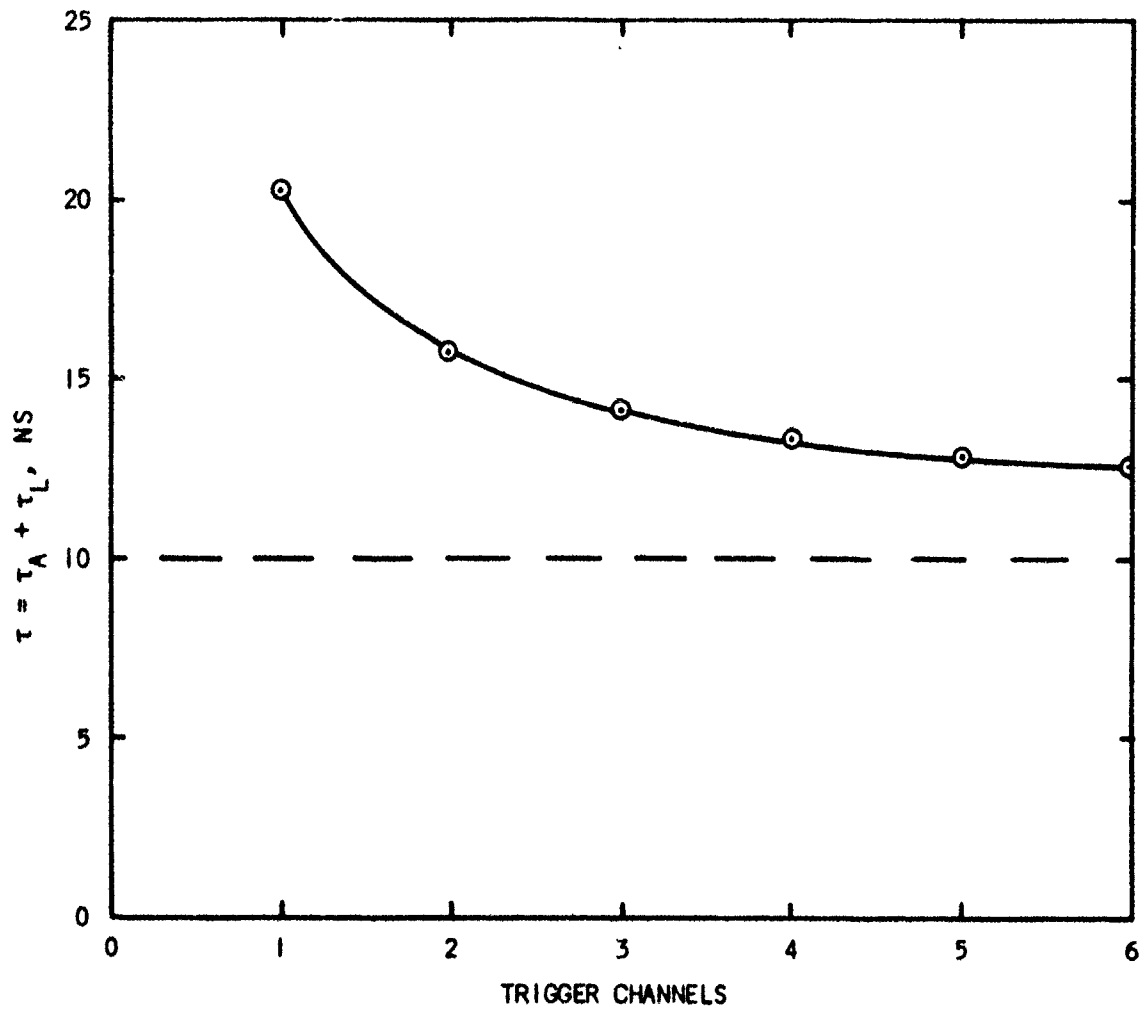


Figure 5.2 Calculated SPI-PULSE 6000 Risetime vs. Number of Trigger Channels

in it by the relation

$$V_D = K I_D^{2/3}$$

where K is a constant depending only on the diode geometry. For an ideal resistive load, the relation is

$$V_D = R_L I_D$$

The simplest model one can assume to study this non-linearity is that of an ideal transmission line driving the load through an inductor. Defining

$$\begin{aligned} L &= \text{inductance} \\ Z_o &= \text{line impedance} \\ V_o &= \text{charging voltage} \\ T_o &= L/Z_o \\ I_{\max} &= V_o/Z_o \\ \sigma &= t/T_o \\ f &= I_D/I_{\max} \end{aligned}$$

then the equation describing either the linear (resistive) or non-linear (Child-Langmuir) case during the first double transit time of the line is

$$\frac{df}{d\sigma} = 1 - f - \alpha f^Y$$

where

$$\alpha = \begin{cases} R_L/Z_o, & \text{resistive case} \\ \frac{K}{Z_o I_{\max}^{1/3}}, & \text{non linear-case} \end{cases}$$

and

$$\gamma = \begin{cases} 1, & \text{linear case} \\ 2/3, & \text{non-linear case} \end{cases}$$

The linear case is easily solved to give

$$\sigma = \frac{1}{1 + \alpha} \ln \frac{1}{1 - (1 + \alpha) f}$$

For the non-linear case the formal solution is

$$\sigma = \int_0^f \frac{df'}{1 - (f' + \alpha f')^{1/3}}$$

which cannot be solved analytically. However, for early times ($f \ll 1/2$) the denominator can be expanded in a power series and integrated term by term. The result is

$$\begin{aligned} \sigma = \ln \frac{1}{1 - f} + 3 \alpha f^{5/3} \sum_{n=0}^{\infty} \frac{n+1}{3n+5} f^n \\ + 3 \alpha^2 f^{7/3} \sum_{n=0}^{\infty} a_n f^n + \alpha^3 f^3 \sum_{n=0}^{\infty} b_n f^n + \dots \end{aligned}$$

A numerical comparison was made between a matched-load resistive diode and a non-linear load which gives the same peak current ($\alpha = 1/2^{1/3}$). In this case, the late time behavior can be approximated by

$$f = 1/2 (1 - \epsilon)$$

and

$$\begin{aligned}\frac{df}{d\sigma} &= \frac{-1}{2} \frac{d\epsilon}{d\sigma} = 1 - 1/2(1 - \epsilon) - 1/2 (1 - \epsilon)^{2/3} \\ &= 1/2 + \frac{\epsilon}{2} - 1/2 (1 - \epsilon)^{2/3}\end{aligned}$$

Using a power series expansion, this gives

$$\begin{aligned}\frac{d\epsilon}{d\sigma} &= \frac{-5}{3} \epsilon - \frac{2}{9} \epsilon^2 - \dots \\ &= \frac{-5}{3} \epsilon \left(1 + \frac{2}{15} \epsilon + \dots \right)\end{aligned}$$

For $\epsilon \leq 0.1$ the term in parenthesis is only a 2% correction or less and can be ignored. Then

$$\epsilon = e^{-5/3\sigma}$$

and

$$f = 1/2 (1 - e^{-5/3\sigma})$$

Figure 5.3 shows both the linear solution and the two limiting solutions for the non-linear case. Note that peak current occurs at $f = 1/2$. It is apparent that the current risetime in the non-linear case is longer than for an ideal load, the increase being about 23%. This effect is not normally accounted for, and clearly has an influence on risetime calculations. More subtle effects, an example being the finite cathode turn-on time, are harder to assess.

5.3 TRIGATRON SWITCHING

5.3.1 Trigatron Approach

Trigatron switching was chosen as the basic approach because of the success that it has had in similar gas insulated high voltage systems. With trigatrons it was felt that ± 1.5 nanosecond jitter could be achieved which

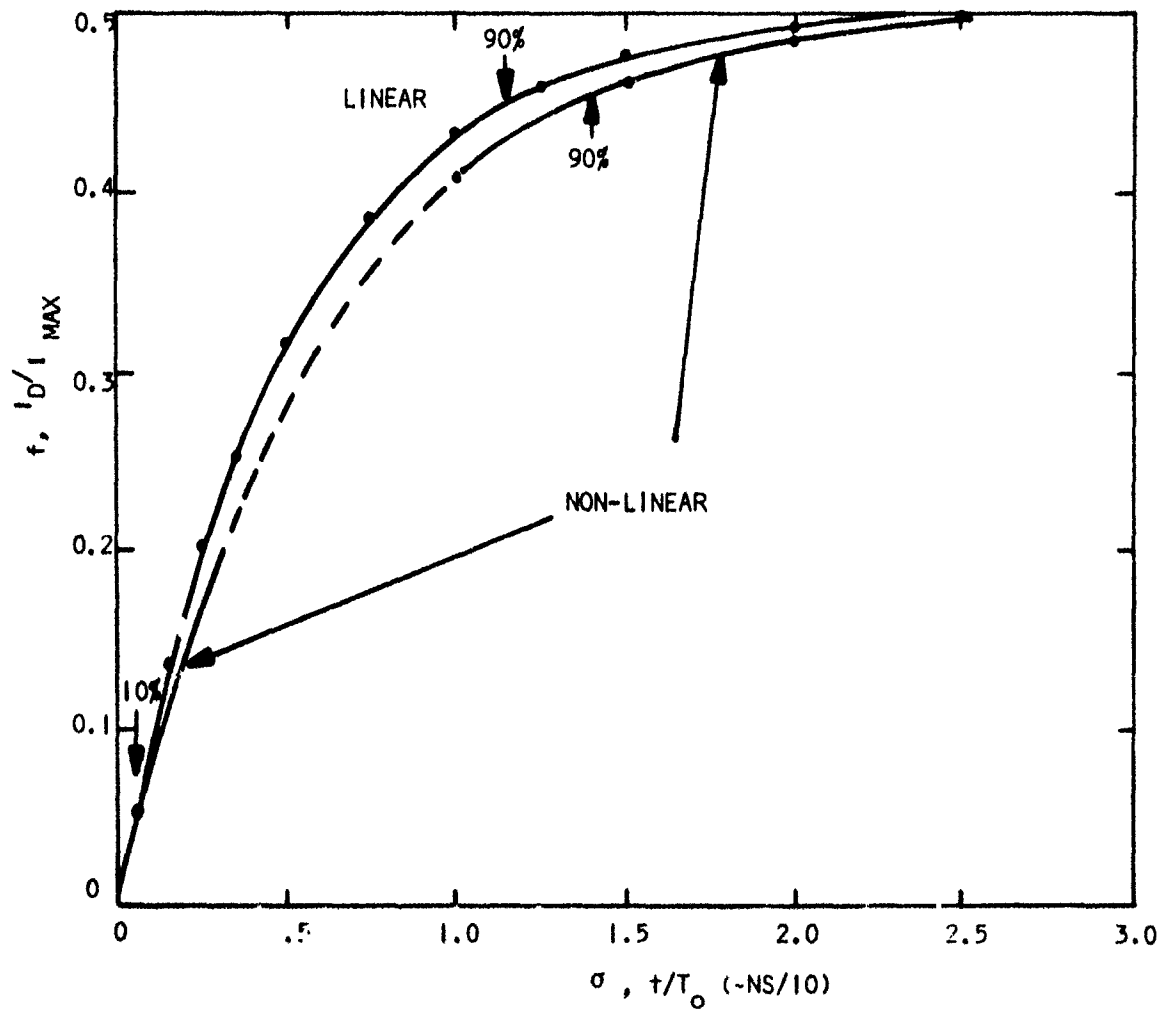


Figure 5.3 Calculated SPI-PULSE 6000 Current Risetime Waveforms for Linear and Non-linear Loads

is quite adequate for synchronously firing two or more machines. In addition, it had been shown⁽¹²⁾ that even less jitter between switches could be expected when driven simultaneously by the same power source. Multiple channel switching of a single machine could therefore be accomplished which would reduce machine front end inductance and thereby decrease risetime.

5.3.2 Trigatron Design Analysis

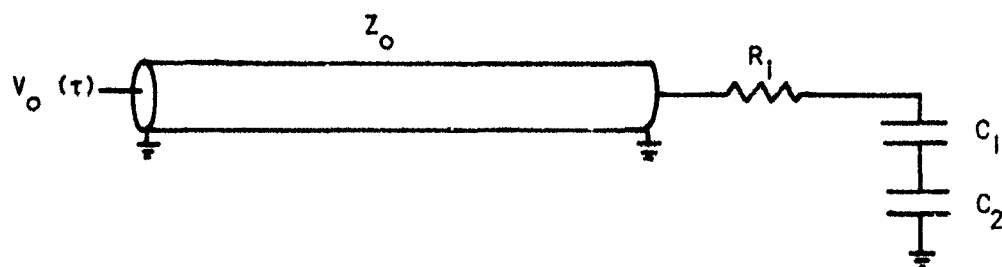
Since multiple parallel switch channels would be required to attain the desired risetime, it was necessary to determine the best design for feeding in the trigger signal. The simplest approach would have been to use a single input cable and then tap-off from it to each trigatron. Alternately, a separate cable could feed each trigatron. In either case, an isolation resistor is required for each cable to prevent the main output voltage pulse from traveling back to the trigger generator.

A schematic of the electrical circuit for each cable is shown in Figure 5.4; time isolation is provided by the trigger cable length with the source input - $V_o(t)$ - being at one end. The return path to cable ground is provided by the capacitance between trigger pin and trigger housing in series with the capacitance between trigger housing and machine ground. Using Laplace transform techniques, the trigger voltage can be shown to be

$$V_{\text{TRIGGER}} = \frac{V_o}{sZ_o C_1} e^{-\frac{s\tau}{2}} \frac{\frac{2}{\alpha + 1}}{1 + \frac{(\alpha - 1)}{(\alpha + 1)} e^{-s\tau}}$$

where

- $\frac{\tau}{2}$ = one-way transit time of cable
- C_1 = trigger pin to trigger housing
- C_2 = trigger housing to ground capacitance
- R_1 = isolation resistance
- Z_o = cable wave impedance



C_1 = TRIGGER PIN TO TRIGGER HOUSING CAPACITANCE

C_2 = TRIGGER HOUSING TO GROUND CAPACITANCE

Figure 5.4 Electrical Circuit for Trigatron Trigger

$$\alpha = \frac{1 + s R_1 C_{\text{eff}}}{s Z_0 C_{\text{eff}}}$$

$$C_{\text{eff}} = \frac{C_1 C_2}{C_1 + C_2}$$

The multiplicative exponential can be ignored since it simply gives a time shift. If the input voltage pulse risetime is less than the double-transit time of the cable, then

$$\begin{aligned} \tilde{V}_{\text{TRIGGER}} &= \frac{2}{\alpha + 1} \frac{\tilde{V}_0}{s Z_0 C_1} \\ &= \frac{2}{1 + C_1/C_2} \frac{W_1 \tilde{V}_0}{s + W_1} \end{aligned}$$

where

$$W_1 = 1/(R_1 + Z_0) C_{\text{eff}}$$

Using the convolution theorem,

$$V_{\text{TRIGGER}}(t) = \frac{2}{1 + C_1/C_2} \int_0^t V_0(u) g(t-u) du$$

where

$$\begin{aligned} g(t) &= L^{-1} \left[\frac{W_1}{s + W_1} \right] \\ &= W_1 e^{-W_1 t} \end{aligned}$$

If

$$V_o(t) = V_o = \text{Constant}$$

then

$$V_{\text{TRIGGER}}(t) = \frac{2 V_o}{1 + C_1/C_2} (1 - e^{-W_1 t})$$

This indicates that:

- to get voltage doubling it is necessary that $C_1 \ll C_2$
- to get good risetime $(R_1 + Z_o) C_{\text{eff}} < 1 \text{ ns}$

$$\text{or } \frac{(R_1 + Z_o) C_1}{1 + C_1/C_2} < 1 \text{ nsec}$$

It is clear that the best performance can be obtained when each trigatron has its own cable. If a single cable were to drive n channels, then

$$C_1 \rightarrow n C_1$$

and the inequalities above are harder to satisfy.

Capacitance estimates for the design chosen - each trigatron driven by its own cable - indicate that the above inequalities are indeed satisfied and it can be expected that the trigger pulse risetime is determined by the trigger generator itself.

A further objection to the single cable feeding n channels approach is that if one gap closes early then it will short out the other channels and inhibit multi-channel operation.

It is expected that the jitter inherent in the trigatron gaps themselves will be very small (less than one nanosecond). The criteria for multi-channel operation is that the jitter in closing the high voltage gap for each

channel be less than the resistive phase time constant. Typically the jitter is a few percent of the streamer crossing time - that is the time to cross the high voltage gap. For a positive point-plane gap, the streamer transit time can be estimated from the formula⁽¹³⁾

$$F t^{1/6} d^{1/10} = K p^n$$

where, for Freon,

$$K = 40$$

$$n = 0.4$$

and

$$F = \text{gap field in KV/cm} \approx 200$$

$$t = \text{breakdown time (transit time) in } \mu\text{sec}$$

$$d = \text{gap spacing (=2 cm) in cm}$$

$$p = \text{pressure in atmospheres}$$

Then

$$t_{\text{streamer}} \approx 0.7 \text{ ns}$$

so that any jitter in this quantity will be negligible. Therefore, since the combined trigatron gap jitter plus streamer transit jitter is less than the resistive phase time constant (2-3 ns), it is anticipated that satisfactory multi-channel formation can be realized.

5.3.3 Trigatron Design

The trigatron design, shown in Figure 5.5 was arrived at after evaluating a number of previous designs⁽¹⁴⁾. It consists of a high voltage cable (Belden 8870) which attaches to a copper electrode through a high voltage feed. The copper electrode is housed in a ceramic insulator and attached to the trigger dome. A high voltage pulse from the cable initiates a spark from the copper electrode, across the ceramic, to the grounded switch dome. This spark then initiates the formation of a breakdown channel from the low voltage dome to the high voltage surface which is parallel to the dome. The critical dimensions of the trigatron are the electrode to dome gap and the electrode recess.

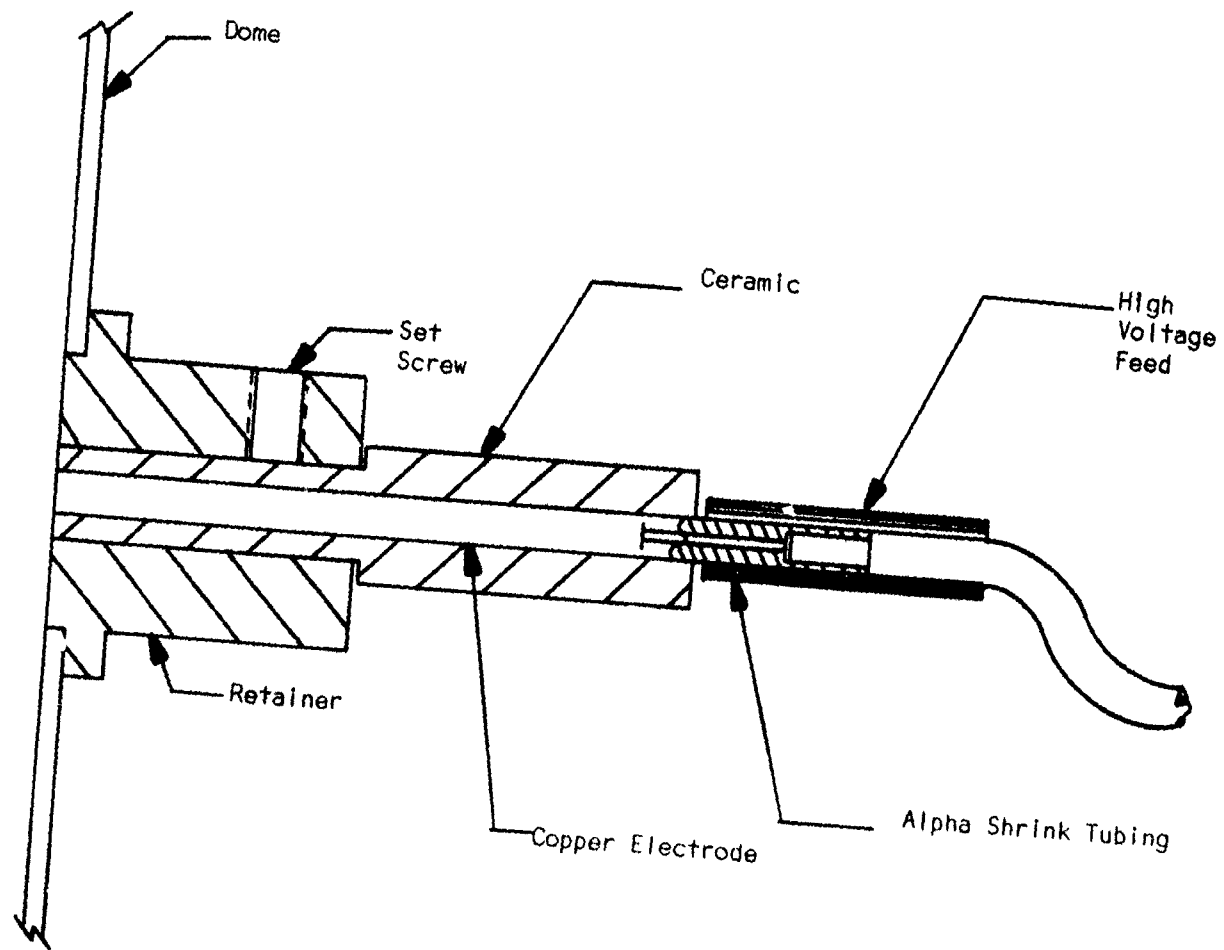


Figure 5.5 Trigatron Assembly

Associated with the trigatron itself is an isolation resistor gap. This gap, shown in Figure 5.6 prevents the high energy store of the SPI-PULSE 6000 from discharging through the trigger cable.

5.3.4 Trigger Voltage Source

The SPI-PULSE 2500 was chosen as the voltage source for driving the trigatron switches. The SPI-PULSE 2500 is a D.C. charged, solid dielectric energy store capable of storing 150 joules and discharging this energy in a pulse of typically 150 nanoseconds duration and 50 nanoseconds risetime. Peak diode voltage is in excess of 80 kV.

The front-end assembly is shown in Figure 5.7. Standard hardware consists of the pumping chamber, diagnostic chamber and shank. Special hardware designed for switch purposes included the cathode shank head, extension chamber, variable load resistor and end plate.

Normal operation of the SPI-PULSE machines utilizes a cathode mounted on the shank head and a transmitting anode separated by a few millimeters. In this program the diode consists of the load resistor and cables connected directly to the shank. The cables are stripped of their ground shield inside the chamber for seven inches to prevent flashover.

Since SPI-PULSE machines operate normally with two to ten ohms diode impedance and the number of switch cables was variable, the CuSO_4 load resistor was used to match the load to the generator.

5.3.5 Trigatron Switching Checkout

Trigatron checkout was performed using the apparatus shown in Figure 5.8. The trigatrons were mounted in a circular array in a high pressure test chamber. The configuration was similar to that used in the SPI-PULSE 6000 front end. Moebius loops were placed near each trigatron spark gap in order to detect when it closed.

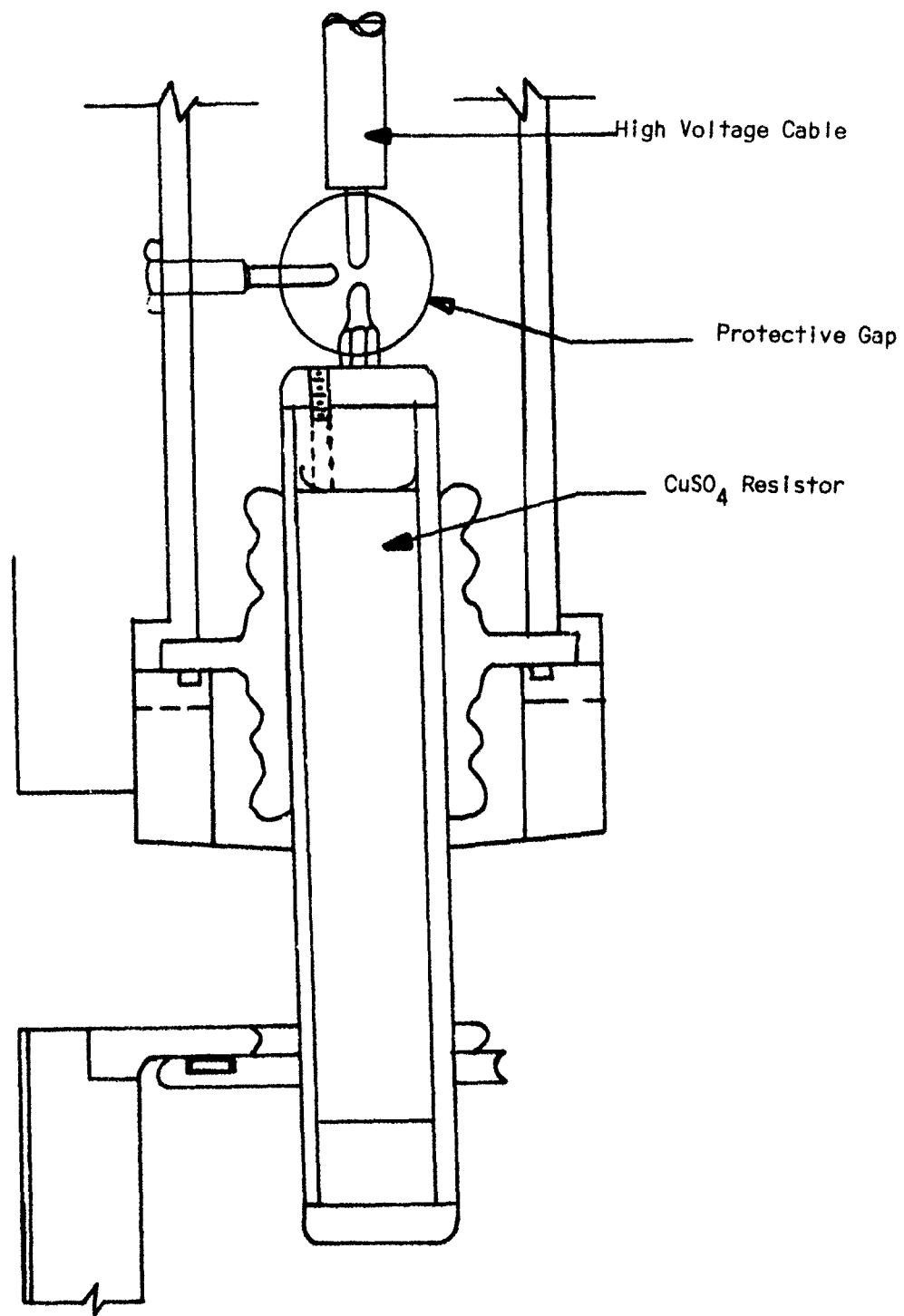


Figure 5.6 Isolation Resistor-Gap

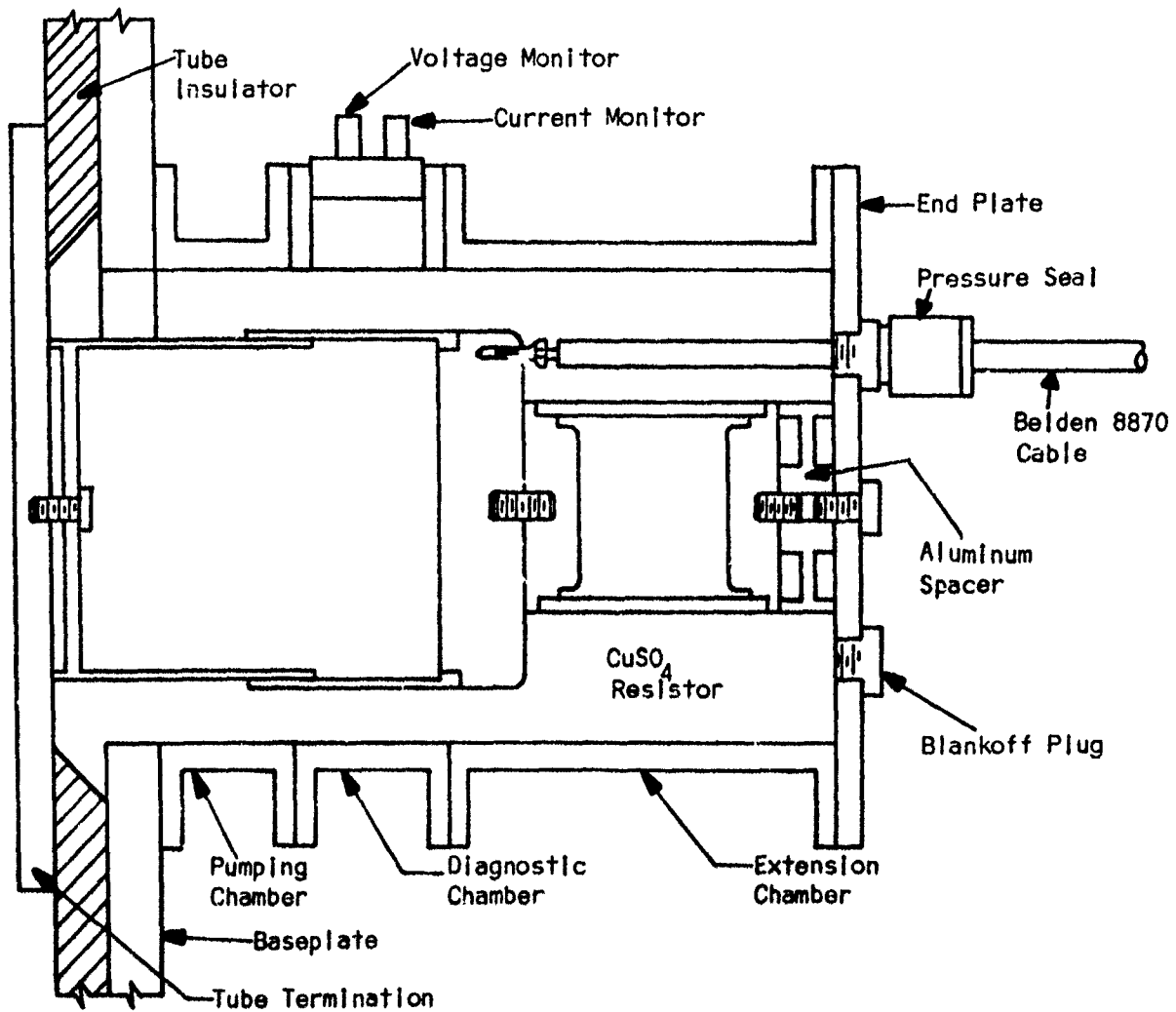


Figure 5.7 Front-end Assembly for SPI-PULSE 2500
When Used as a Power Supply Trigger Source

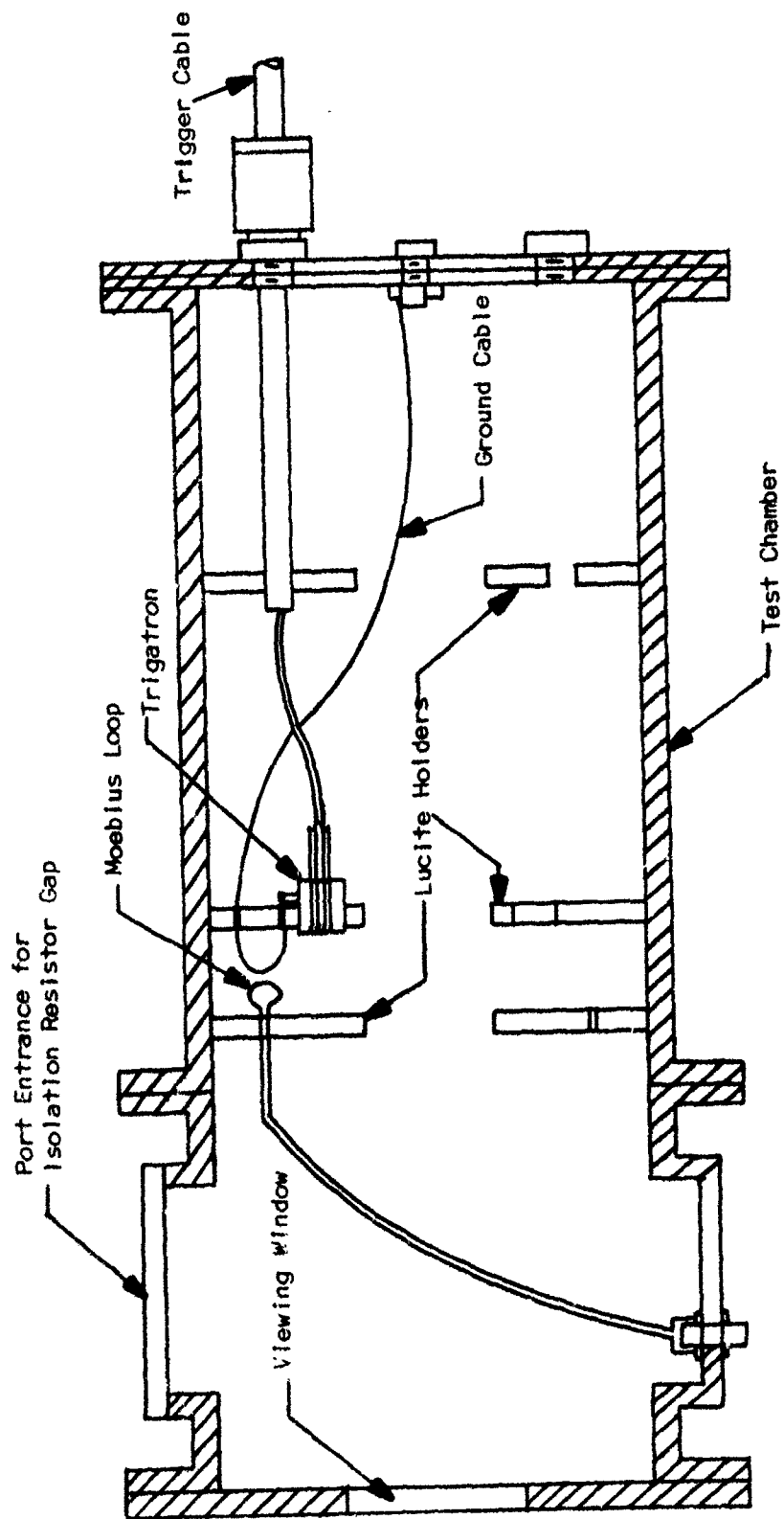


Figure 5.8 Test Chamber for Trigatrons Under Pressure

These bench tests established that the jitter associated with one switch firing was < 1 ns and between simultaneously pulsed switches was < 0.5 ns. This configuration was then incorporated into the SPI-PULSE 6000 front end.

5.4 MODIFIED SPI-PULSE 6000 TESTING

5.4.1 Machine Final Switching Configuration

After a number of design iterations the final machine front end and switching configuration is as shown in Figure 5.9. The circular array of six trigatrons are housed in an enlarged diode cap at machine ground. The high voltage trigger cables from the SPI-PULSE 2500 come through feed-throughs in the vacuum coax chamber and then through CuSO_4 resistors and isolation gaps into the cathode shank. The cables then connect to the center electrode of the trigatrons as in the configuration used for bench testing. Since the trigatrons are in 30 psi Freon, they are attached to the tube cap with a high pressure/vacuum seal.

It was determined, early in the test program, that a positive SPI-PULSE 2500 trigger pulse was more effective in switching than was a negative pulse. All final testing was therefore done with a positive pulse.

5.4.2 SPI-PULSE 6000 Delay and Jitter Measurements

Delay is defined as the time between the SPI-PULSE 2500 diode (i.e. high voltage bushing) voltage signal and that of the SPI-PULSE 6000 diode voltage. Initially, delay was determined as a function of SPI-PULSE 6000 charging voltage. Figure 5-10 shows this data as delay vs. percentage of self breakdown voltage. Delays ranged from 100 to 150 nanoseconds.

In order to get acceptable jitter, it was necessary to operate the machine at greater than 85% of the self breakdown voltage. Representative jitter data can be seen in Figure 5.11. Ten successive diode voltage traces are overlaid on this traced oscillogram. Table 5.1 contains the time for the start of each trace from a standard reference. It shows the mean firing time from this reference to be 6.9 ns with a standard deviation of ± 1.7 ns.

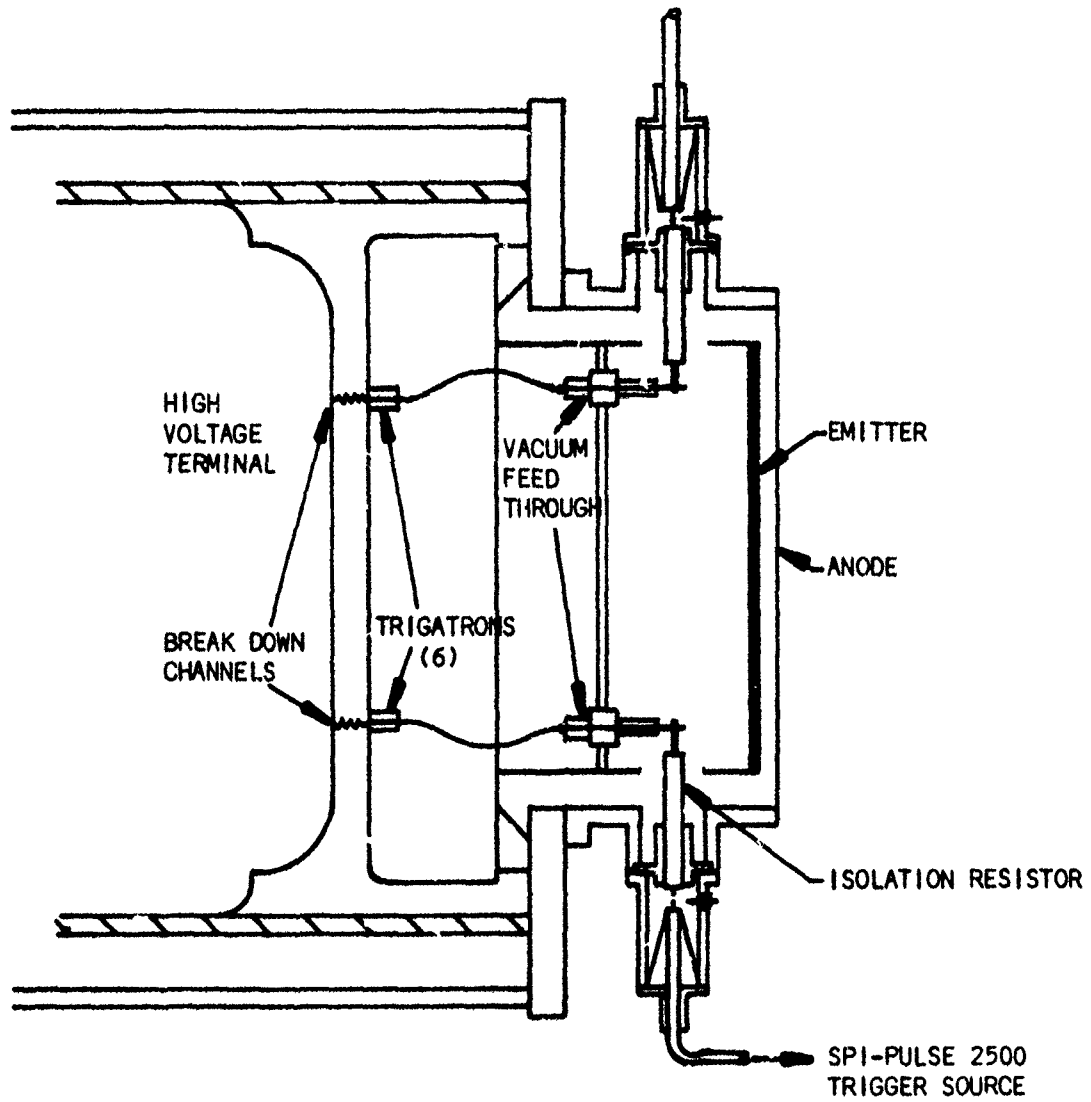


Figure 5.9 Trigatron Trigger Adaptation to SPI-PULSE 6000
Low Inductance Front End

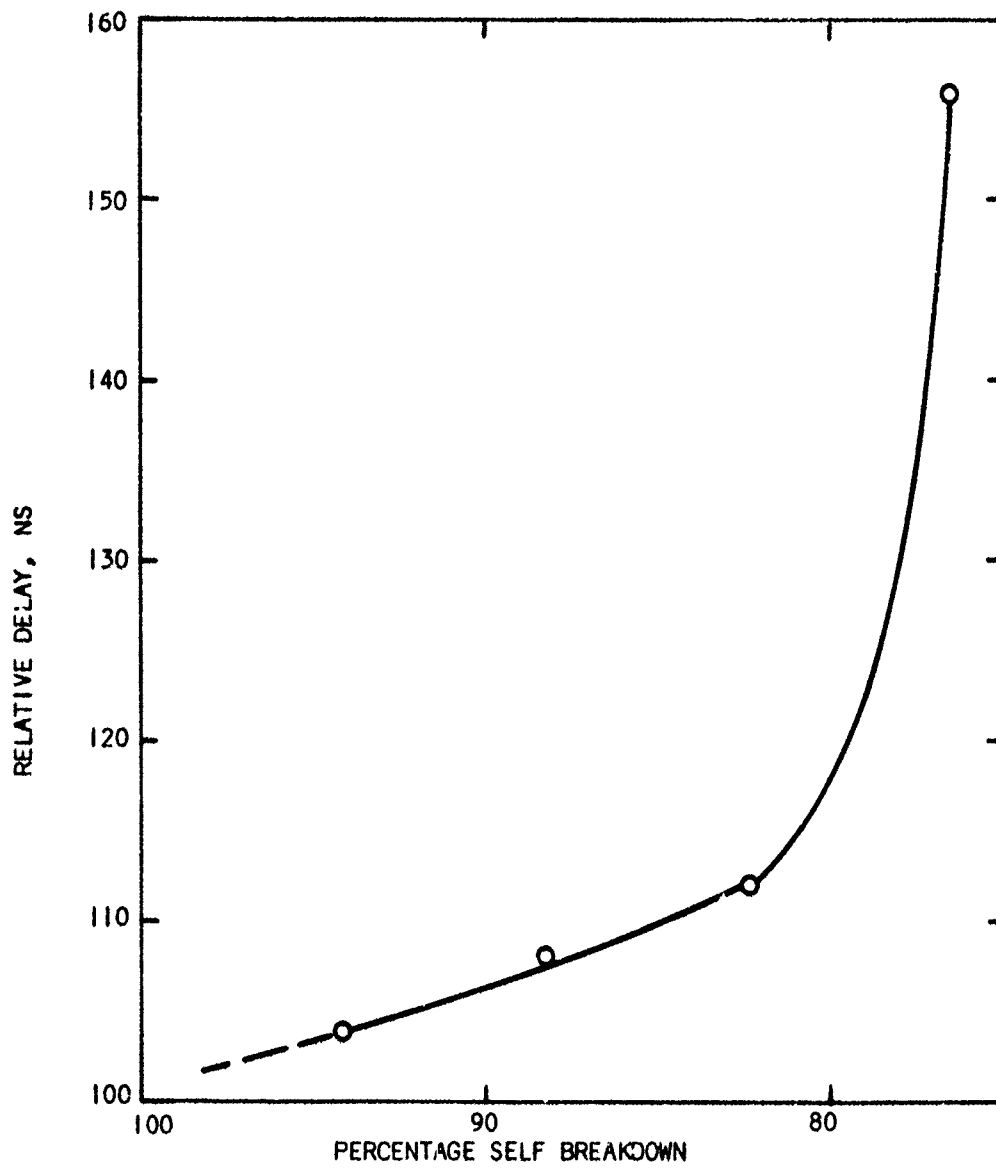


Figure 5.10 Relative Switching Delay as a Function of Percentage of Self Breakdown Voltage

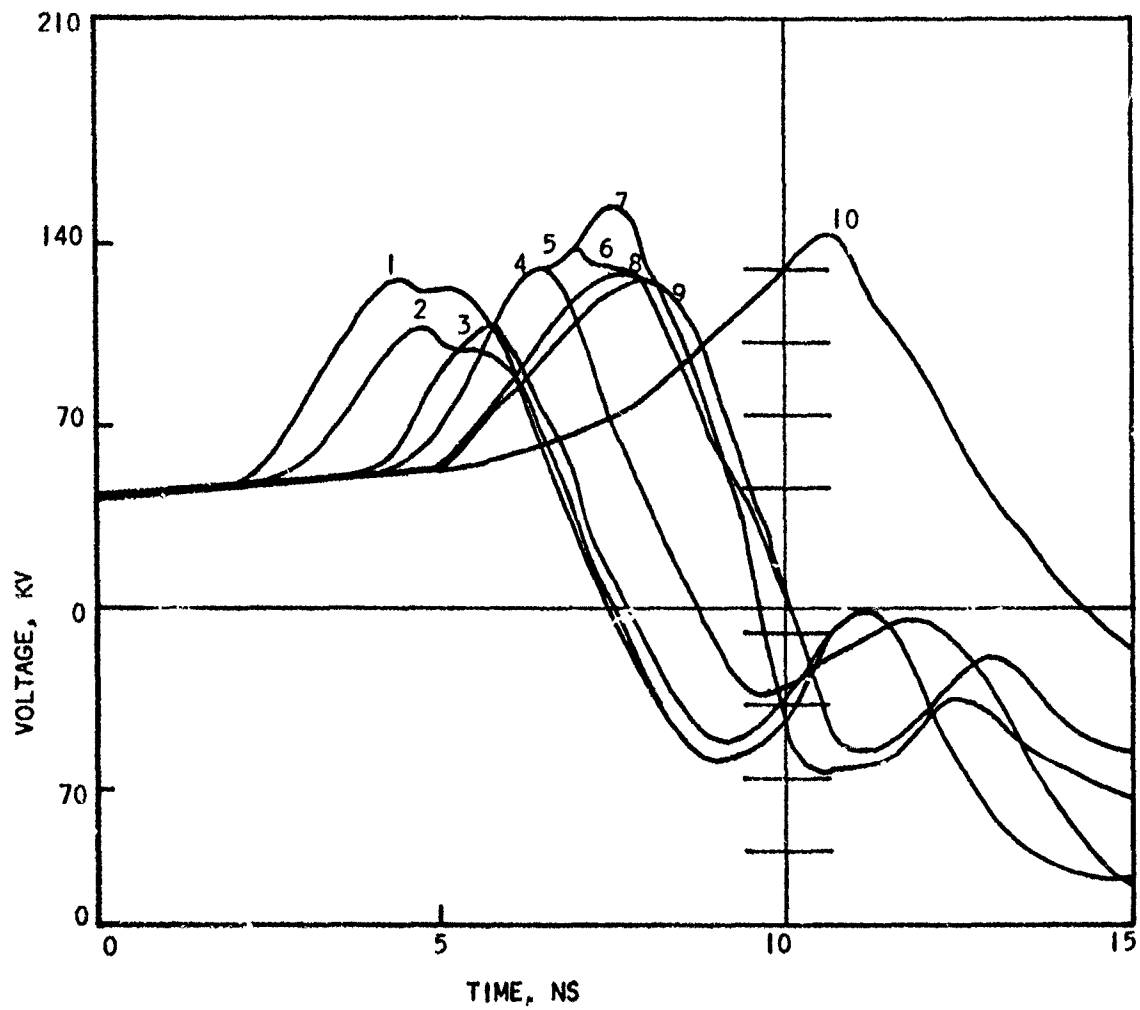


Figure 5.11 Diode Voltage Traces Showing Relative Jitter of SPI-PULSE 6000 Discharge at $V_0 = 165$ kV (Shot No. 2091-2100)

This result is well within the requirement for synchronously firing two or more SPI-PULSE machines.

TABLE 5.1 SUMMARY OF JITTER MEASUREMENT

TRACE (Relative)	TIME OF PEAK (ns from reference)
1	4.7
2	4.8
3	5.7
4	6.5
5	6.5
6	6.9
7	7.5
8	7.7
9	7.8
10	10.6

Mean Firing Time (ns); 6.9
Deviation - jitter (ns): ± 1.7

5.4.3 SPI-PULSE 6000 Risetime Measurements

Because of mechanical difficulties, only three trigatron units were operable during the testing phase in which jitter and risetime measurements were made. The problem was caused by cracking of the thin ceramic insulator sleeve on three of the trigatron trigger pins; the time required to fabricate new sleeves did not allow replacement. Therefore, the results of this and the previous section apply to a three channel switch only.

Initial risetime measurements were made using a 3.5 ohm copper sulfate resistive load. This removed any ambiguities associated with the finite turn-on time and non-linear nature of a cold cathode diode. Tests were made using one, two, and three trigatrons. The results are summarized in Figure 5.12. The SPI-PULSE 6000 charging voltage was 160 KV, and the trigger source (SPI-PULSE 2500) charging voltage was 90 KV. It is apparent that there is little

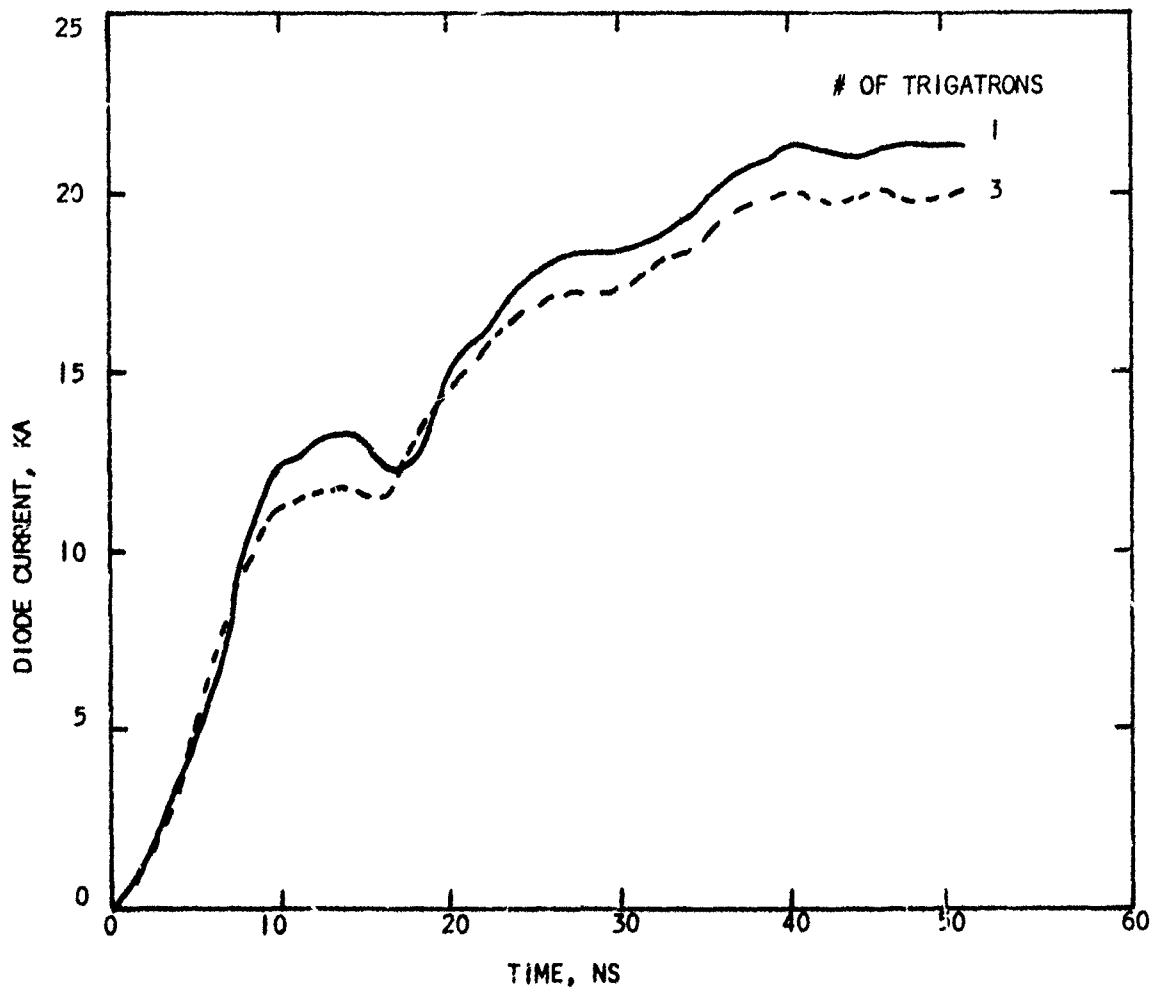


Figure 5.12 SP1-PULSE 6000 Diode Current Waveform Into a 3.5 ohm Dummy Load Showing 2 ns Improvement From One to Three Trigatrons

change in risetime between the cases of one or three trigatrons. The indications are that multi-channel operation is being achieved; this will be considered later.

The next set of measurements was made using the cold cathode diode. The cathode was 30 cm in diameter, and a 1.5 cm gap was used. Again the charging voltage was 160 KV, and the trigger source voltage 90 KV. Figure 5.13 shows the resulting diode current waveform. The initial current rise to one-half of peak value is very fast (4 ns); thereafter the pulse front slows down. The 10% - 90% risetime is 23 ns, and the pulse width is 78 ns (fwhm). The peak diode voltage in this case was approximately 85 KV.

The observed risetime is comparable to that expected for single channel switching (cf. Section 5.2). Since the resistive load results indicated that in fact three channels were probably operating, the discrepancy must arise from some effect not previously considered.

In order to interpret the experimental results, use was made of the transmission line code⁽¹⁾. The modeling of the modified SPI-PULSE 6000 consisted of the following elements:

- 1) the prime energy store
- 2) the high voltage spinning
- 3) the multi-channel switch
- 4) the switch housing
- 5) a short inductance representing that portion of the cathode shank inside the output tube
- 6) a capacitor-shunting the above inductance - representing the output tube capacitance to ground
- 7) a coaxial line representing the shank feeding the load
- 8) either a resistive or diode load

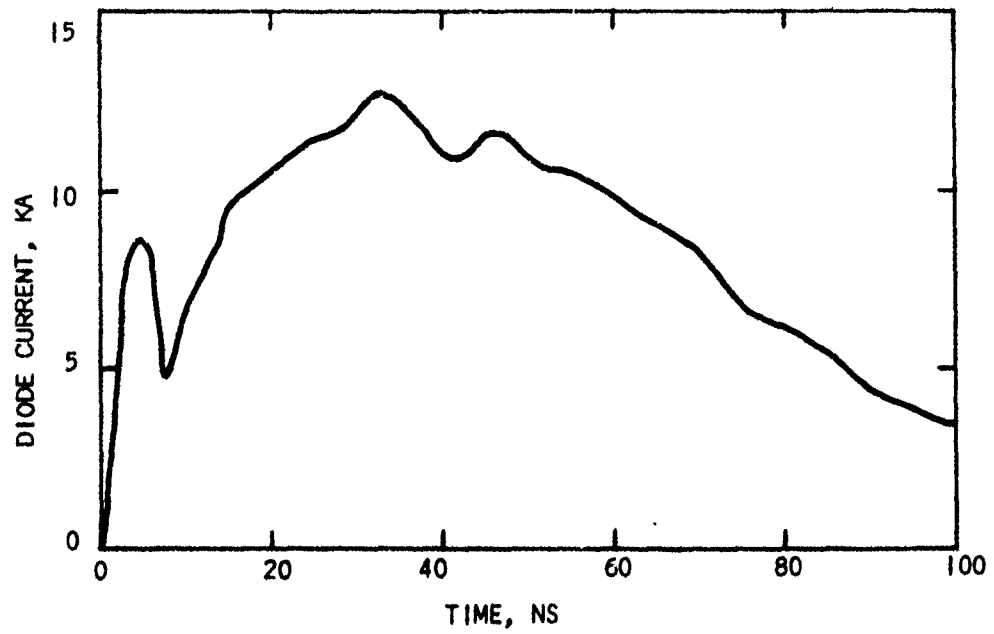


Figure 5.13 SPI=PULSE 6000 Diode Current Waveform With 30 cm Diameter Cathode and Three Trigatron Switching

In the resistive load case, the resistor also has a rather large inductance (35 nH) associated with it. The effect of the inductance associated with the resistive load is to increase the risetime. The faster the risetime becomes with more switch channels, the greater the effect. As a result, the difference between one and three channels, being six ns theoretically, is reduced to about 3 ns, which agrees with the experimental results shown in Figure 5.12. This was also included in the model. Figure 5.14 shows a comparison of the computer generated diode current compared to the experimentally measured value. Because the experimental peak current was only 70% of the computer value, the curves have been normalized to provide better comparison. The values correspond to single channel switching only; generally there is good agreement between the two waveshapes. The computer risetime is about 4 ns faster than the measured one; given the uncertainties involved in choosing the elements for the computer model, the results indicate that the machine is operating about as can be expected. It should be pointed out that if the resistor inductance were not present, the risetime would have been more nearly 20 ns.

Figure 5.15 compares diode current waveforms both computed and measured when a 30 cm diameter cold cathode diode was used. The computer-modelled diode current exponentially rises to peak value with a 4 ns e-folding time. In both the computed and experimental curves three trigatron channels were assumed to be operating. Again, the agreement is quite good. It is expected that improvements in the turn-on time of the diode (cathode plasma formation time) would lower the risetime to 13 ns.

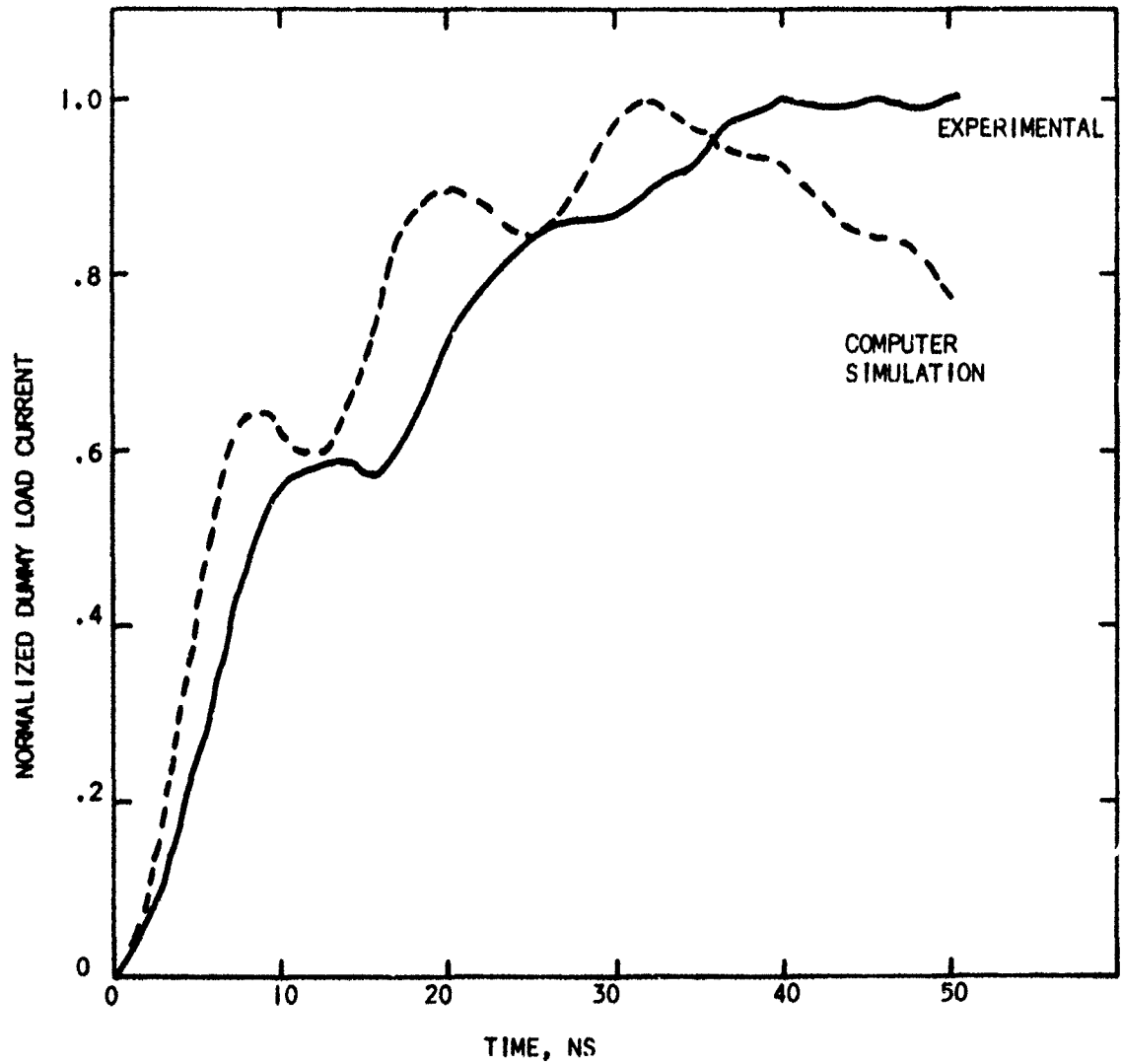


Figure 5.14 Comparison of Measured and Calculated SPI-PULSE 6000 Dummy Load Current Waveforms

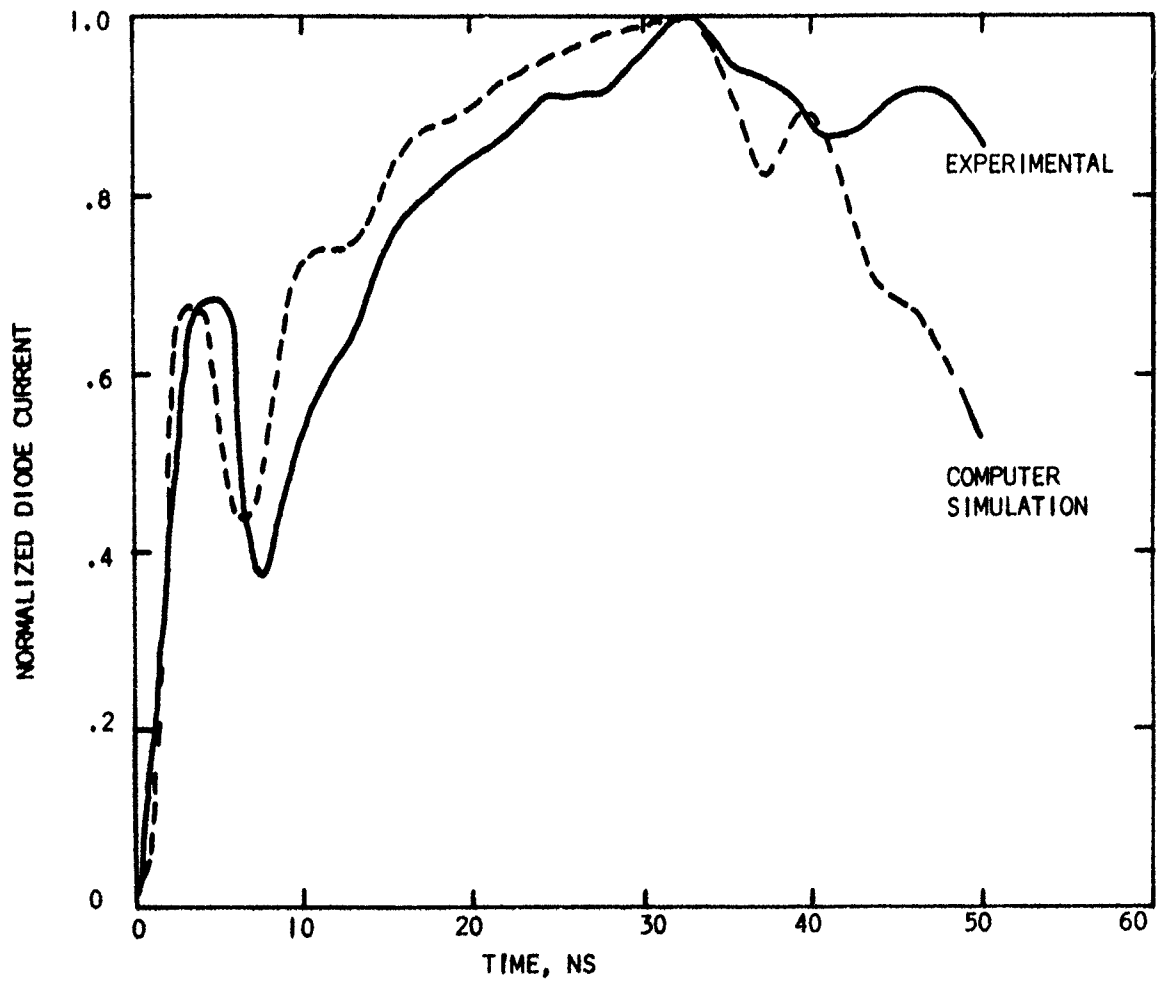


Figure 5.15 Comparison of Measured and Calculated SPI-PULSE 6000 Diode Load Current Waveforms

SECTION VI

SUMMARY

This final report has reviewed the work performed in the development of an electron beam IEMP Simulation capability. The techniques used for calibrating these electron beam environments have been discussed and representative IEMP cavity data presented.

The data of IEMP cavity currents for various pressures and simple cavity geometries shows the value of the electron beam technique for phenomenology studies. An extension of this capability into more complex "system-like" cavities containing cables and electronic boxes is now a straightforward matter.

The effect of dielectrically lined cavity walls were evaluated. Unlike gas neutralization for instance, the existence of this phenomena was not evident through analytical studies. That this effect could be demonstrated and characterized in some detail is further evidence of the utility of this simulation approach.

Modifications made to the SPI-PULSE 6000 were described in detail. The front-end changes along with the incorporation of multichannel low jitter switching has significantly increased the risetime of the current pulse allowing a broad range of electron beams to be produced, extending the simulation capability. For instance, a 5 ns wide (baseline) pulse of 18 keV average electron energy at 10 amps/cm² over 620 cm² has been developed.

In addition, the low jitter switching (± 1.7 ns) now makes it possible to produce very large emission patterns by synchronously firing multiple machines in stacked configurations.

In addition to complex cavity IEMP studies, an experiment which addresses aspects of SGEMP phenomena is planned. This experiment, illustrated in Figure 6-1, consists of injecting an electron beam into the center of a large vacuum chamber and monitoring the flow of electrons about this disc-shaped "emission" source. With the previously described 5 ns baseline pulse, current can be characterized in a time frame short compared to chamber wall reflected wave interference times.

Depending upon requirements, even further advances in pulsed electron beam simulation of IEMP/SGEMP phenomena can be envisioned. For instance, in addition to flat disc emission, other irregular shapes and surface structures can be made to emit with existing technology. Also, multi-energetic electron spectra can be produced simultaneously with advanced "chromacolor" window techniques and electron angular distributions can be tailored to particular requirements.

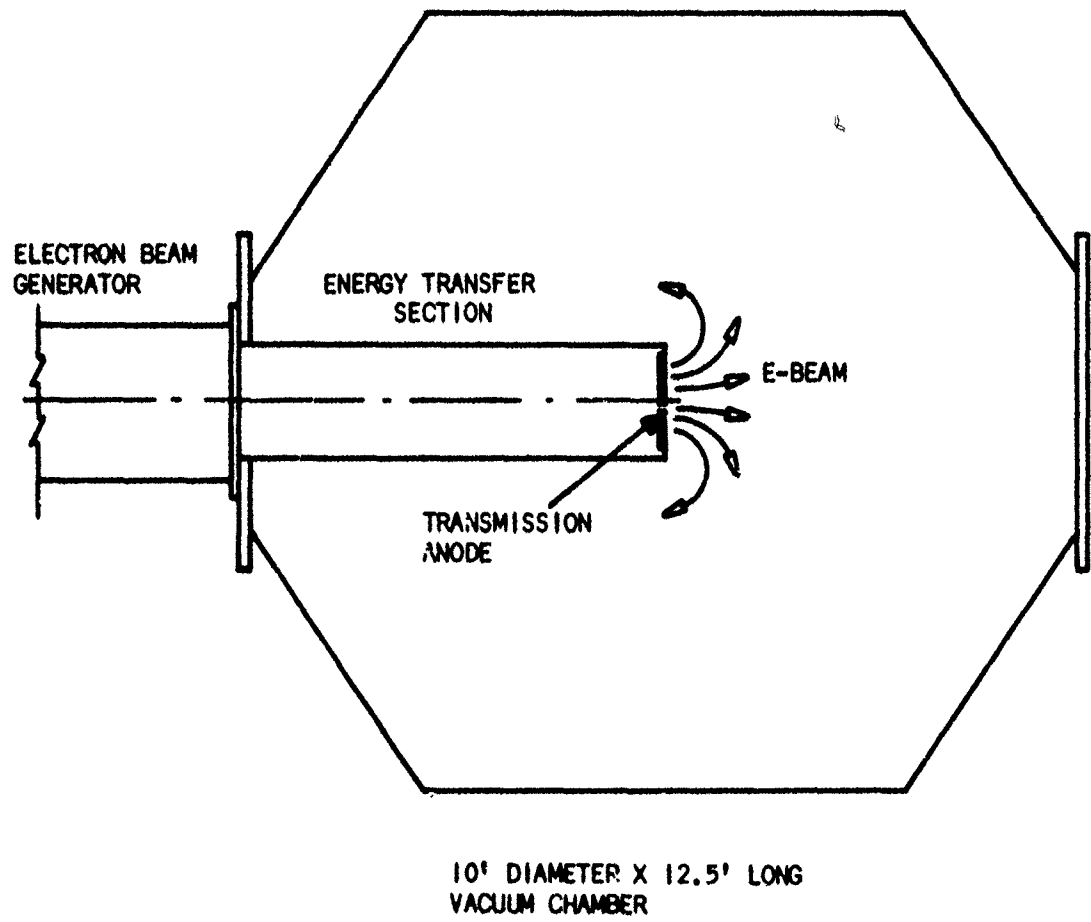


Figure 6-1. SPI-PULSE 6000 in SGEMP Configuration

REFERENCES

- (1) Shipman, J., "Program Trans", NRL, Private Communication, January 1975.
- (2) "ELTRAN, One Dimensional Monte Carlo Transport Code", RSIC Computer Code Collection, CCC-155, SC-TM-68-713.
- (3) Little, R., and M. Kima, "Thin Film Mapping of Electron Accelerators", IEEE Transactions on Nuclear Science, Vol. NS-20, No. 3, June 1973.
- (4) Lowell, R., "Development of a 12 Inch IEMP Simulation Capability", SPI FR-74-20013, IRT Contract No. 8101.99, May 1974.
- (5) Osborn, D.C., et.al., "Large Area Electron Beam Experiments", INTEL-RT 8101-011, Topical Report HDL Contract No. DAAG39-74-C-0006, July 1975.
- (6) Little, R. G., et.al., IEEE Trans. Nuc. Sci., NS-21, #6 (Dec. 1974) pp. 249.
- (7) Stahl, R.H., Et. al., IEEE Trans. Nuc. Sci., NS-20, #6 (Dec. 1973) pp. 26.
- (8) Genuario, R., and A. Bromborsky, IEEE Trans. Nuc. Sci., NS-21, #6 (Dec. 1974) pp. 243.
- (9) Weingart, R.C., et. al., IEEE Trans. Nuc. Sci., NS-19, #6, (Dec. 1972) pp. 15.
- (10) Martin, J.C., AFWL High Voltage Note #2, (March 1971).
- (11) Anderson, R.A., App. Phys. Lett., 24, (15 Jan. 1974) pp. 54.
- (12) Milde, H. and J. Moriarty, "Switching of Fast, High Voltage Pulse Generators", High Voltage Technology Seminar Vol. 11, Sept. 1969.
- (13) Martin, J.C., "Duration of the Resistive Phase and Inductance of Spark Channels", SSWA/JCM/1065/25.
- (14) "Flash X-ray Machine Triggering Circuits", Ion Physics Report EI, August 1968.

DISTRIBUTION LIST

DEPARTMENT OF DEFENSE

Director
Defense Advanced Research Projects Agency
ATTN: NMR

Director
Defense Civil Preparedness Agency
ATTN: TS AED

Defense Communication Engineer Center
ATTN: Code 1035, Nicholas A. Sica
ATTN: Code R-103P
ATTN: Robert Rostron

Director
Defense Communications Agency
ATTN: Code B-205, George B. Adkins
ATTN: Code 430
ATTN: Code 800, Fred Bond
ATTN: Code 830, Monte I. Burgett, Jr.
ATTN: NMR

Defense Documentation Center
12 cy ATTN: TC

Director
Defense Intelligence Agency
ATTN: DI-7B, Edward O'Farrell

Director
Defense Nuclear Agency
ATTN: RATN
ATTN: STSI, Archives
ATTN: DDST
2 cy ATTN: RAEV
3 cy ATTN: STTL, Tech. Lib.

Commander
Field Command
Defense Nuclear Agency
ATTN: FCPR
ATTN: FCLMC

Director
Interservice Nuclear Weapons School
ATTN: Doc. Con.

Director
Joint Strategic Target Planning Staff, JCS
ATTN: JLTW-2

Chief
Livermore Division, Field Command, DNA
ATTN: Doc. Con. for L-395
ATTN: FCPRL

National Communications System
Office of the Manager
ATTN: NCS-TS, Charles D. Bodson

Director
National Security Agency
ATTN: Oriand O. Van Gunten, R-425

OJCS/J-3
ATTN: J-3, RDTA Br., WWMCCS, Plans Div.

DEPARTMENT OF DEFENSE (Continued)

OJCS/J-5
ATTN: J-5, Plans & Policy, R & D Div.

Commander-in-Chief
U.S. European Command, JCS
ATTN: ECJ6-P

DEPARTMENT OF THE ARMY

Director
Ballistic Missile Defense Advanced Technical Center
ATTN: RDMH-O, F. M. Hoke

Commander
Ballistic Missile Defense System Command
ATTN: SSC-TEN, L. L. Dickerson
ATTN: BDMSC-TEN, Noah J. Hurst

Deputy Chief of Staff for Research Development & Acq.
ATTN: DAMA-CSM-N, LTC E. V. DeBoesser, Jr.

Commander
Harry Diamond Laboratories
ATTN: DRXDO-RB, Robert E. McCoskey
ATTN: DRXDO-RCC, Raine Gilbert
ATTN: DRXDO-EM, R. Gostak
ATTN: DRXDO-RBH, Stewart S. Graybill
ATTN: DRXDO-RC, Robert B. Oswald, Jr.
ATTN: DRXDO-TI, Tech. Lib.
ATTN: DRXDO-EM, George Merkel
ATTN: DRXDO-RCC, John A. Rosado
ATTN: DRXDO-TR, Edward E. Conrad
ATTN: DRXDO-NP, Francois N. Wimenits
ATTN: DRXDO-RB, Joseph R. Miletta
ATTN: DRXDO-RCC, John E. Thompkins
ATTN: DRXDO-EM, John Bombardt

Commander
Picatinny Arsenal
ATTN: SARPA-ND-C-E, Amina Nordio
ATTN: SARPA-FR-E, Louis Avrami
ATTN: SMUPA-ND-W
ATTN: SMUPA-TN, Burton V. Franks
ATTN: SARPA-ND-N-D
ATTN: SARPA-TS-I-E, Abraham Grinooch

Commander
Redstone Scientific Information Center
3 cy ATTN: Chief, Documents

Commander
TRASANA
ATTN: ATAA-EAC, Francois N. Winans

Director
U.S. Army Ballistic Research Laboratories
ATTN: DRXBR-AM, Donald Eccleshall

Chief
U.S. Army Communications Sys. Agency
ATTN: SCCM-AD-SV, Library

DEPARTMENT OF THE ARMY (Continued)

Commander
U. S. Army Electronics Command
ATTN: DRSEL-NL-O-4
ATTN: DRSEL-GG-TD, W. R. Werk
ATTN: DRSEL-TL-IR, Edwin T. Hunter
ATTN: DRSEL-TL-ME, M. W. Pomerantz
ATTN: DRSEL-PL-ENV, Hans A. Bomke

Division Engineer
U. S. Army Engr. Div., Missouri River
ATTN: MRDED-MC, Floyd L. Hazlett

Commander-in-Chief
U. S. Army Europe & Seventh Army
ATTN: ODCSE-E, AEAGE-PI

Commandant
U. S. Army Field Artillery School
ATTN: ATSFA-CTD-ME, Harley Moberg

Commander
U. S. Army Foreign Science & Tech. Ctr.
ATTN: DRXST-ISI, Daniel W. McCallum, Jr.

Commander
U. S. Army Mat. & Mechanics Research Center
ATTN: DRXMR-HH, John F. Diguam

Commander
U. S. Army Materiel Dev. & Readiness Command
ATTN: DRCDE-D, Lawrence Flynn

Commander
U. S. Army Missile Command
ATTN: DRCPM-PE-EG, William B. Johnson

Commander
U. S. Army Safeguard Command
ATTN: Chief, Activation Division

Commander
U. S. Army Test & Evaluation Command
ATTN: DRSTE-EL, Richard I. Kolchin
ATTN: DRSTE-NB, Russell R. Galasso

DEPARTMENT OF THE NAVY

Chief of Naval Operations
ATTN: Robert A. Blaise
ATTN: Code 604CS, Robert Placost

Chief of Naval Research
ATTN: Code 464, Thomas P. Quinn
ATTN: Code 427, Henry Mullaney

Commander
Naval Air Systems Command
ATTN: AIR-5202, Muriel L. Scarborough

Commander
Naval Electronic Systems Command
ATTN: Code 5032, Charles W. Neill
ATTN: PME 117-T
ATTN: PME 117-21

Commander
Naval Electronics Laboratory Center
ATTN: Code 3100, E. E. McCown

DEPARTMENT OF THE NAVY (Continued)

Commanding Officer
Naval Intelligence Support Center
ATTN: NISC-611

Director
Naval Research Laboratory
ATTN: Code 2627, Doris R. Folen
ATTN: Code 4004, Emanuel L. Brancato
ATTN: Code 6631, James C. Ritter
ATTN: Code 7770, Gerald Cooperstein
ATTN: Code 7706, Jay P. Boris
ATTN: Code 7761, Jack D. Brown

Commander
Naval Sea Systems Command
ATTN: SEA-9931, Riley B. Lane
ATTN: SEA-9931, Samuel A. Barham

Commander
Naval Ship Engineering Center
ATTN: Code 6174D2, Edward F. Duffy

Commander
Naval Surface Weapons Center
ATTN: Code 431, Edwin R. Rathburn
ATTN: Code WA-501, Navy Nuc. Prgms. Off.
ATTN: Code WA-50, John H. Malloy
ATTN: Code 431, Edwin B. Dean
ATTN: Code WX-21, Tech. Lib.

Commander
Naval Telecommunications Command
ATTN: N-7, LCDR Hall

Commander
Naval Weapons Center
ATTN: Code 533, Tech. Lib.

Commanding Officer
Naval Weapons Evaluation Facility
ATTN: Lawrence R. Oliver

Commanding Officer
Naval Weapons Support Center
ATTN: Code 70242, Joseph A. Munarin
ATTN: Code 7024, James Ramsey

Director
Strategic Systems Project Office
ATTN: NSP-230, David Gold
ATTN: NSP-2431, Gerald W. Hoskins
ATTN: NSP-2701, John W. Pitscoberger

DEPARTMENT OF THE AIR FORCE

Commander
ADC/DE
ATTN: DEEDS, Joseph C. Brannan

AF Geophysics Laboratory, AFSC
ATTN: Charles Pike
ATTN: LQR, Edward A. Burke

AF Institute of Technology, AU
ATTN: Library, AFIT, Bldg. 640, Area B

AF Materials Laboratory, AFSC
ATTN: Library

DEPARTMENT OF THE AIR FORCE (Continued)

AF Weapons Laboratory, AFSC

ATTN: EL, John Darrah
ATTN: SUL
ATTN: ELA
ATTN: ELC
ATTN: JAB
ATTN: SAS
ATTN: EL

**Commander
ASD**

ATTN: 4960 Test W/TZMH, Peter T. Marth
ATTN: ASD-YH-EX, Lt Col Robert Leverette

**Headquarters
Electronic Systems Division, AFSC**

ATTN: DCD/SATIN IV
ATTN: XRRT

Commander

Foreign Technology Division, AFSC
ATTN: ETET, Capt Richard C. Husemann

HQ USAF/RD

ATTN: RDQPN

Commander

Rome Air Development Center, AFSC
ATTN: P. Gianino

SAMSO/DY

ATTN: LYS, Capt Wayne Schober
ATTN: DYS, Maj Larry A. Darda

SAMSO/IN

ATTN: IND, Maj Darryl S. Muskin

SAMSO/MN

ATTN: MNNH, Capt William M. Carra
ATTN: MNNG, Capt David J. Strobel
ATTN: MNNH, Capt Michael V. Bell
ATTN: MNNG

SAMSO/SK

ATTN: SKF, Peter H. Stadler

SAMSO/XR

ATTN: XRS

SAMSO/YD

ATTN: YDD, Maj Marion F. Schneider

Commander in Chief

Strategic Air Command
ATTN: XPPS, Capt DeRaad
ATTN: NRI-STINFO, Library

ENERGY RESEARCH & DEVELOPMENT ADMINISTRATION

University of California

Lawrence Livermore Laboratory
ATTN: William J. Hogan, L-531
ATTN: Walter W. Hofer, L-24
ATTN: Louis F. Wouters, L-48
ATTN: Donald W. Vollmer, L-154
ATTN: Donald J. Meeker, L-545
ATTN: Frederick R. Kovar, L-31
ATTN: Hans Kruger, L-96
ATTN: Tech. Info., Dept. L-3

ENERGY RESEARCH & DEVELOPMENT ADMINISTRATION
(Continued)

Los Alamos Scientific Laboratory

ATTN: Doc. Con. for John S. Malik
ATTN: Doc. Con. for Marvia M. Hoffman
ATTN: Doc. Con. for J. Arthur Freed
ATTN: Doc. Con. for Donald R. Westervelt
ATTN: Doc. Con. for Reports Library
ATTN: Doc. Con. for Bruce W. Noel
ATTN: Doc. Con. for Richard L. Wakefield
ATTN: Doc. Con. for P. W. Keaton

Sandia Laboratories

Livermore Laboratory
ATTN: Doc. Con. for Theodore A. Dellin

Sandia Laboratories

ATTN: Doc. Con. for Org. 2110, J. A. Hood
ATTN: Doc. Con. for 3141, Sandia Rpt. Coll.
ATTN: Div. 5231, James H. Renken
ATTN: Doc. Con. for Org. 2315, James E. Gover
ATTN: Doc. Con. for Org. 2353, R. L. Parker
ATTN: Doc. Con. for 5240, Gerald Youas
ATTN: Doc. Con. for Elmer F. Hartman

OTHER GOVERNMENT AGENCIES

Administrator

Defense Electric Power Admin.
ATTN: Doc. Con.

Department of Commerce

National Bureau of Standards
ATTN: Judson C. French

Department of Transportation

Federal Aviation Administration
ATTN: Fredrick S. Sakate, ARD-350

NASA

ATTN: Code Res. Guid. Con. & Info. Sys.

NASA

ATTN: Library
ATTN: Robert R. Lovell, M.S. 54-3

DEPARTMENT OF DEFENSE CONTRACTORS

Aerojet Electro-Systems Co. Div.
ATTN: Thomas D. Hanscombe

Aeronutronic Ford Corporation

Western Development Laboratories Division
ATTN: Donald R. McMorro, M.S. G-30
ATTN: Library
ATTN: J. T. Mattingley, M.S. X-22

Aerospace Corporation

ATTN: Irving M. Garfunkel
ATTN: Frank Hai
ATTN: J. Benveniste
ATTN: William W. Willis
ATTN: C. B. Pearlston
ATTN: Library
ATTN: Julian Reinheimer
ATTN: V. Josephson
ATTN: Norman D. Stockwell

DEPARTMENT OF DEFENSE CONTRACTORS (Continued)

Avco Research & Systems Group
ATTN: Research Library, A-830, Rm. 7201

Battelle Memorial Institute
ATTN: Robert H. Blazek

The BDM Corporation
ATTN: T. H. Neighbors

The Bendix Corporation
Navigation & Control Division
ATTN: George Gartner

The Boeing Company
ATTN: Robert S. Caldwell, M.S. 2R-00
ATTN: Kenneth D. Friddell, M.S. 2R-00
ATTN: Aerospace Library
ATTN: Howard W. Wicklein, M.S. 17-11
ATTN: David L. Dye, M.S. 87-75
ATTN: Donald W. Egekrout, M.S. 2R-00

Booz-Allen & Hamilton, Inc.
ATTN: Raymond J. Chrisner

Brown Engineering Company, Inc.
ATTN: John M. McSwain, M.S. 18

University of California at San Diego
ATTN: Sherman De Forest

Charles Stark Draper Laboratory, Inc.
ATTN: Richard G. Haltmaier
ATTN: Kenneth Fertig
ATTN: Paul R. Kelly

Computer Sciences Corporation
ATTN: Barbara F. Adams

Computer Sciences Corporation
ATTN: Richard H. Dickhaut
ATTN: Alvin T. Echiff

Cutler-Hammer, Inc.
AIL Division
ATTN: Anne Anthony, Central Tech. Files

Dr. Eugene P. dePlomb

The Dikewood Corporation
ATTN: K. Lee
ATTN: Tech. Lib.

E-Systems, Inc.
Greenville Division
ATTN: Library 8-50100

EG&G, Inc.
Albuquerque Division
ATTN: Hilda H. Hoffman
ATTN: Tech. Lib.

Electronics Technology Laboratory
ATTN: R. Curry

Exp. & Math. Physics Consultants
ATTN: Thomas M. Jordan

DEPARTMENT OF DEFENSE CONTRACTORS (Continued)

Fairchild Camera & Instrument Corporation
ATTN: Sec. Dept. for 2-233, David K. Myers

The Franklin Institute
ATTN: Ramie H. Thompson

General Electric Company
Space Division
ATTN: Joseph C. Peden, VFSC, Rm. 4230M
ATTN: Daniel Edelman
ATTN: Larry I. Chasen
ATTN: John L. Andrews
ATTN: James P. Spratt

General Electric Company
Re-Entry & Environmental Systems Division
ATTN: Robert V. Benedict

General Electric Company
TEMPO-Center for Advanced Studies
ATTN: William McNamara
ATTN: Royden R. Rutherford
ATTN: John D. Ilgen
ATTN: DASLAC

General Electric Company
Aircraft Engine Group
ATTN: John A. Ellerhorst, E-2

General Electric Company
Aerospace Electronics Systems
ATTN: Charles M. Hewison, Drop 624
ATTN: W. J. Patterson, Drop 233

General Research Corporation
ATTN: John Ise, Jr.

General Research Corporation
Washington Operations
ATTN: David K. Ostas

Goodyear Aerospace Corporation
Arizona Division
ATTN: B. Manning

Grumman Aerospace Corporation
ATTN: Jerry Rogers, Dept. 533

GTE Sylvania, Inc.
Electronics Systems Group-Eastern Division
ATTN: Charles A. Thornhill, Librarian
ATTN: Leonard L. Blaisdell

GTE Sylvania, Inc.
ATTN: Herbert A. Ullman
ATTN: Emil P. Motchok, Comm. Sys. Div.
ATTN: S. E. Periman, A. S. M. Dept.
ATTN: David P. Flood
ATTN: Mario A. Nurefora, H & V Group

Hazeltine Corporation
ATTN: M. Waite, Tech. Info. Ctr.

Hercules, Incorporated
ATTN: W. R. Woodruff, 100K-26

Honeywell, Incorporated
Government & Aeronautical Products Division
ATTN: Ronald R. Johnson, A-1622

DEPARTMENT OF DEFENSE CONTRACTORS (Continued)

Honeywell, Incorporated
Aerospace Division
ATTN: Harrison H. Noble, M.S. 725-6A
ATTN: Richard B. Reinecke, M.S. 725-6

Honeywell, Incorporated
Radiation Center
ATTN: Tech. Lib.

Hughes Aircraft Company
ATTN: Kenneth R. Walker, M.S. D-157
ATTN: Billy W. Campbell, M.S. 6-E-110
ATTN: Tech. Lib.
ATTN: John B. Singletary, M.S. 6-D-133

Hughes Aircraft Company
Space Systems Division
ATTN: William W. Scott, M.S. A-1080
ATTN: Edward C. Smith, M.S. A-620

IBM Corporation
ATTN: Frank Frankovsky

ITT Research Institute
ATTN: Irving N. Mindel
ATTN: Jack E. Bridges

Institute for Defense Analyses
ATTN: IDA, Librarian, Ruth S. Smith

International Telephone & Telegraph Corporation
ATTN: Alexander T. Richardson

Ion Physics Corporation
ATTN: Robert D. Evans

IRT Corporation
ATTN: Terry Flanagan
ATTN: James A. Naber
ATTN: R. L. Mertz
ATTN: Dennis Swift

Jaycor, Incorporated
ATTN: Eric Wenas
ATTN: Andrew Woods

Johns Hopkins University
Applied Physics Laboratory
ATTN: Peter E. Partridge

Kaman Sciences Corporation
ATTN: Library
ATTN: Donald H. Bryce
ATTN: W. Foster Rich
ATTN: Walter E. Ware
ATTN: Albert P. Bridges
ATTN: John R. Hoffman

Litton Systems, Inc.
Guidance & Control Systems Division
ATTN: R. W. Maughmer
ATTN: John P. Retzler
ATTN: Val J. Ashby, M.S. 67

Lockheed Missiles & Space Company
ATTN: Clarence F. Kooi, Dept. 52-11

DEPARTMENT OF DEFENSE CONTRACTORS (Continued)

Lockheed Missiles & Space Co., Inc.
ATTN: Edwin A. Smith, Dept. 85-85
ATTN: Samuel I. Taimuty, Dept. 85-85
ATTN: Benjamin T. Kimura, Dept. 81-14
ATTN: Philip J. Hart, Dept. 81-14
ATTN: George F. Heath, Dept. 81-14

LTV Aerospace Corporation
Vought Systems Division
ATTN: Charles H. Coleman

LTV Aerospace Corporation
Michigan Division
ATTN: James F. Sanson, B-2
ATTN: Tech. Lib.

M.I.T. Lincoln Laboratory
ATTN: Jean L. Ryan
ATTN: Leona Loughlin, Librarian, A-082

Martin Marietta Aerospace
Orlando Division
ATTN: William W. Mrs. MP-413
ATTN: Jack M. Ashford, MP-537
ATTN: Mona C. Griffith, Library, MP-30

Martin Marietta Corporation
Denver Division
ATTN: Ben T. Graham, M.S. PO-454
ATTN: J. E. Goodwin, Mail 0452

Maxwell Laboratories, Inc.
ATTN: Victor Fargo

McDonnell Douglas Corporation
ATTN: Stanley Schneider
ATTN: Paul H. Duncan, Jr.

Mission Research Corporation
ATTN: Conrad L. Longmire
ATTN: Roger Stettner
ATTN: William C. Hart
ATTN: Daniel F. Higgins

Mission Research Corporation
ATTN: David E. Merewether
ATTN: Larry D. Scott

Mission Research Corporation
ATTN: V. A. J. Van Lint

The Mitre Corporation
ATTN: Theodore Jarvis

Motorola, Inc.
Government Electronics Division
ATTN: James R. Black, M.S. A-112
ATTN: A. J. Kordalewski, Tech. Info. Ctr.

Northrop Corporation
Electronic Division
ATTN: Boyce T. Ahlport
ATTN: John M. Reynolds
ATTN: Vincent R. DeMartino
ATTN: John M. Reynolds

Northrop Corporation
ATTN: Joseph D. Russo

DEPARTMENT OF DEFENSE CONTRACTORS (Continued)

Northrop Corporation
ATTN: Library
ATTN: Orle L. Curtis, Jr.
ATTN: David N. Pocock

Physics International Company
ATTN: Doc. Con. for John H. Huntington
ATTN: Doc. Con. for Ian D. Smith
ATTN: Doc. Con. for Charles H. Stallings
ATTN: Doc. Con. for Philip W. Spence

Pulsar Associates, Inc.
ATTN: Carleton H. Jones, Jr.

R & D Associates
ATTN: Richard R. Schaefer
ATTN: Leonard Schlessinger
ATTN: William R. Graham, Jr.
ATTN: William J. Karsas
ATTN: S. Clay Rogers

The Rand Corporation
ATTN: Cullen Craik

Raytheon Company
ATTN: Gajanan H. Joshi, Radar Sys. Lab.

Raytheon Company
ATTN: Harold L. Fiescher

RCA Corporation
Government & Commercial Systems
ATTN: George J. Brucker

RCA Corporation
ATTN: K. H. Zainiger

RCA Corporation
Government & Commercial Systems
ATTN: Andrew L. Warren
ATTN: Eleanor K. Daly

RCA Corporation
ATTN: E. Van Keuren, 13-5-2

Research Triangle Institute
ATTN: Sec. Officer for Eng. Div., Mayraat Simons, Jr.

Rockwell International Corporation
ATTN: N. J. Rudie, FA-53
ATTN: J. Spetz
ATTN: L. H. Pinson, FB-41
ATTN: Donald J. Stevens, FA-70
ATTN: George C. Messenger, FB-61
ATTN: James E. Bell, HA-10

Rockwell International Corporation
ATTN: John F. Roberts

Rockwell International Corporation
ATTN: T. B. Yates

Sanders Associates, Inc.
ATTN: James L. Burrows
ATTN: R. G. Despathy, Sr., P E, 1-6270
ATTN: Moe L. Aitel, NCA, 1-3236

DEPARTMENT OF DEFENSE CONTRACTORS (Continued)

Science Applications, Inc.
Huntsville Division
ATTN: Noel R. Byrn

Science Applications, Inc.
ATTN: J. Roger Hill

Science Applications, Inc.
ATTN: Charles Stevens

Science Applications, Inc.
ATTN: William L. Chadsey

Sidney Frankel & Associates
ATTN: Sidney Frankel

Simulation Physics, Inc.
ATTN: Roger G. Little
ATTN: John R. Uglum
ATTN: Steven H. Face

The Singer Company
ATTN: Irwin Goldman, Eng. Management

Sperry Flight Systems Division
Sperry Rand Corporation
ATTN: D. Andrew Schow

Sperry Rand Corporation
Univac Division
ATTN: James A. Inda, M.S. 41T25

Sperry Rand Corporation
Sperry Division
ATTN: Paul Marraffino
ATTN: Charles L. Craig, EV

Stanford Research Institute
ATTN: Arthur Lee Whitson
ATTN: Mel Bernstein
ATTN: Phillip J. Dolan
ATTN: Satsuo Dairiki
ATTN: Robert A. Armistead

Stanford Research Institute
ATTN: MacPherson Morgan

Sundstrand Corporation
ATTN: Curtis B. White

Systems, Science & Software
ATTN: David A. Meskus

Systems, Science & Software, Inc.
ATTN: Andrew R. Wilson
ATTN: Ira Katz

Systrom-Donner Corporation
ATTN: Harold D. Morris

Texas Instruments, Inc.
ATTN: Donald J. Maus, M.S. 72

Texas Tech University
ATTN: Travis L. Simpson

DEPARTMENT OF DEFENSE CONTRACTORS (Continued)

TRW Systems Group

ATTN: Donald Jortner
ATTN: Paul Moimud, R1-1196
ATTN: Aaron H. Narovsky, R1-2144
ATTN: Richard H. Kingsland, R1-2154
ATTN: Jerry I. Lubell
ATTN: Philip R. Carder, R1-1028
ATTN: Lillian D. Singletary, R1-1070
ATTN: Robert M. Webb, R1-1150
ATTN: Tech. Info. Ctr., S-1930
ATTN: William H. Robinette, Jr.

TRW Systems Group

San Bernardino Operations
ATTN: Earl W. Allen
ATTN: J. M. Gorman
ATTN: John E. Dahnke

DEPARTMENT OF DEFENSE CONTRACTORS (Continued)

TRW Systems Group

ATTN: Donald W. Pugsley

United Technologies Corporation
Norden Division

ATTN: Conrad Corda

Westinghouse Electric Corporation

ATTN: Henry P. Kalapaca, M. S. 3525